January 2014

Development And Applications Of Gold-Silica Nanohybrids For Bioanalysis

Jiao Chen

DEVELOPMENT AND APPLICATIONS OF GOLD-SILICA NANOHYBRIDS FOR BIOANALYSIS

by

Jiao Chen
Bachelor of Engineering, Zhejiang Chinese Medical University, 2008

A Dissertation

Submitted to the Graduate Faculty

of the

University of North Dakota

In partial fulfillment of the requirements

for the degree of

Doctor of Philosophy

Grand Forks, North Dakota
August
2014

This dissertation, submitted by Jiao Chen in partial fulfillment of the requirements for the Degree of Doctor of Philosophy from the University of North Dakota, has been read by the Faculty Advisory Committee under whom the work has been done, and is hereby approved.

_____
Dr. Julia Xiaojun Zhao

_____
Dr. David T. Pierce

_____
Dr. Alena Kubátová

_____
Dr. Kathryn A. Thomasson

_____
Dr. Min Wu

This dissertation is being submitted by the appointed advisory committee as having met all of the requirements of the Graduate School at the University of North Dakota and is hereby approved.

_____
Wayne Swisher
Dean of the School of Graduate Studies

_____
Date

PERMISSION

Title Development and Applications of Gold-Silica Nanohybrids for Bioanalysis

Department Chemistry

Degree Doctor of Philosophy

In presenting this dissertation in partial fulfillment of the requirements for a graduate degree from the University of North Dakota, I agree that the library of this University shall make it freely available for inspection. I further agree that permission for extensive copying for scholarly purposes may be granted by the professor who supervised my dissertation work or, in her absence, by the Chairperson of the department or the dean of the School of Graduate Studies. It is understood that any copying or publication or other use of this dissertation or part thereof for financial gain shall not be allowed without my written permission. It is also understood that due recognition shall be given to me and to the University of North Dakota in any scholarly use which may be made of any material in my dissertation.

Jiao Chen
August 2014

TABLE OF CONTENTS

LIST OF FIGURES

Figure Page

LIST OF TABLES

Table Page

LIST OF SCHEMES

Scheme Page

ACKNOWLEDGEMENTS

I would never have been able to finish my Ph.D study and dissertation without the guidance of my committee members, help from friends, and support from my family.

I would like to express my deepest gratitude to my advisor, Dr. Julia Xiaojun Zhao, for her guidance, caring, patience, and most importantly, her friendship during my graduate studies at the University of North Dakota. She encouraged me to not only grow as a chemist but also as an instructor and an independent thinker. For everything you've done for me, Dr. Zhao, I thank you. I would also like to thank all of my committee members: Dr. David T. Pierce, Dr. Alena Kubátová, Dr. Kathryn A. Thomasson, and Dr. Min Wu. Thank Dr. Pierce for his guidance and support during my graduate study and recommended me as a graduate representative to be part of dean search committee. This experience provided me with the unique opportunity to gain a wider breadth of experience and helped me on my own job searching. Thank Dr. Alena Kubátová for providing me opportunities to participate in all the outreach activities, through which I learned how to be a good educator and scientist. Thank Dr. Kathryn A. Thomasson for your encouragement all the time through the way you may even not notice. Every time when I got nervous in my seminars or OPRs, I always received your encouraging messages from your smiles and eyes, which supported me to finish my presentations with full of confidence. I would also like to thank Dr. Wu from the School of Medicine and Health for his assistance and guidance in my research projects. Additionally, I am very grateful for the friendship of all of the members of his research group, especially Xuefeng Li, with whom I worked closely

on one project and solved many problems.

I would like to thank all of faculty members who have been very kind enough to extend their help at various phases of my research and Ph.D study. My current and former colleagues, Yuhui Jin, Aize Li, Song Liang, Carrie John, Xu Wu, Shaina Strating, Fei Tian, Yuqian Xing, Joseph Birrenkott, Kali Shepherd, Aaron Hanson, Robert Ducioame, Yang Zhao, Nenny Fahruddin, have all extended their support in a very special way. I learned a lot from them through their personal and scholarly interactions, their suggestions at various points of my research. They are more like my family members who always support me go through all the difficulties. I would also like to extend my special thanks to the visiting professor, Dr. Xingguang Su from Jilin University.

I am truly grateful for the financial support I received from the UND Graduate School, ND EPSCoR, and UND Chemistry Department. Without their financially support, I could never make it so far. Meanwhile, I appreciate the technical support from the Basic Science Imaging Center for training me on the microscopes and allowing me to use these instruments independently.

Finally, and most importantly, I would like to thank my parents for their support, encouragement, patience and unwavering love in the past five years. Thank them for their faith in me and allowing me to be as ambitious as I wanted.

ABSTRACT

In the first project, both non-spherical and spherical silica nanomateirals with hollow interiors were synthesized by a one-step soft-templating method. By simply changing the applied solvent from ethanol to 1-propanol, or 1-pentanol, three different shapes of nanomaterials, including nanosphere, nanowire, and nanotadpole, could be obtained, respectively. The effects of other factors on morphology were also systematically studied to propose a growth mechanism. It was found that the PVP-water droplet was the crucial factor on the formation of hollow interiors. Without the addition of PVP, only solid silica nanomaterials, such as solid nanoparticles, nanorods, and nanowires, were synthesized. This developed method showed excellent reproducibility and great potential for a large-scale synthesis.

In the second project, a novel nanocomposite contained a spherical gold nanoparticle core, a silica spacer and a fluorescent dye layer in the silica matrix was designed to study the metal-enhanced fluorescence phenomenon. It was found that the size of gold nanoparticles cores and the distances between cores and fluorescent dyes had significant effects on the emitted fluorescence intensity. An enhancement factor of 9.2 was obtained when the nanocomposite contained a 13.7 ± 1.3 nm gold nanoparticle core and a 36.6 ± 4.4 nm silica spacer.

In the third project, an ultrasensitive protein assay was developed by using silica nanorods decorated with gold nanoparticles (AuNPs-SiNPs) as labels in a lateral flow platform. A large number of AuNPs on one single SiNR provided visualized dark purple color that was much darker than the pure AuNPs solution. Therefore, the detection limit was lowered 50 times compared to the traditional AuNP-based lateral

flow assay. Under optimal conditions, a linear range of 0.05 - 2 ng/mL with a detection limit of 0.01 ng/mL was obtained. The lateral flow bioassay based on these composite nanomaterials thus offered an ultrasensitive method for rapid detection of trace amount of proteins and has a potential application for point-of-care screening in clinical diagnostics and biomedical research.

In the fourth project, a new hyperthermia agent, Au-silica nanowire nanohybrid (Au-SiNW nanohybrid) was synthesized and applied in the photothermal therapy. Due to its strong NIR absorption ability, the Au-SiNW nanohybrid can generate significant amount of heat upon NIR irradiation and induced thermal cell death. By incubating the nanohybrids with cancer cells and irradiating with NIR laser, cancer cells were successfully killed, indicating their potential as promising hyperthermia agents.

CHAPTERI

SHAPE-TUNABLE HOLLOW SILICA NANOMATERIALS BASED ON SOFT-TEMPLATING METHOD AND THEIR APPLICATIONS AS DRUG CARRIERS

1. Introduction

Hollow silica nanomaterials have attracted considerable attention due to their excellent biocompatibility, easy surface functionalization accessibility, good chemical inertness and thermal stability.[1-8] They have been used in diverse fields including drug delivery, sensing, catalysis, and large biomolecular release system.[9-11] Two approaches for synthesizing hollow silica nanomaterials can be broadly divided into two categories: hard-templating[12-16] and soft-templating[17-22]. The hard-templating method normally needs a layer of the desired materials coated on the surface of the template core, followed by a selective removal of the template. This approach has been widely used and proven to be effective for the synthesis of hollow nanomaterials with controllable shell thickness. However, tedious and complicated procedures are usually required, which are sometimes expensive and unsuitable for a large scale synthesis. Many efforts have been devoted to developing soft-templating methods. In the soft-templating method, no additional templates are needed and therefore it may have the advantage of better scalability.

On the other hand, the hollow silica nanomaterials obtained by the template methods are mostly spherical in morphology. The preparation of well-defined hollow non-spherical nanomaterials with tunable sizes and morphologies generally introduces additional challenges due to the difficulties in forming uniform coating around high-curvature surfaces and the deficiency of appropriate non-spherical templates.

Therefore, the ability to tune the structure, size, and morphology of the synthesized nanomaterials is an important goal in current material synthesis and device fabrication. Recently, Chen *et al.* developed a method to synthesize silica nanotubes based on the thermolysis of silicon tetraacetate with the assistance of both hard and soft templates.[23] Wu *et al.* found that rodlike hollow silica particles could be obtained by using a surfactant mixture composed of zwitterionic and anionic surfactants as the templates with the assistance of a constructure-directing agent.[24] These non-spherical new members expand the versatility of hollow nanomaterials family and bring some novel properties, functions and potential applications. However, the preparation of non-spherical nanomaterials generally requires strict reaction conditions in addition to high cost and tedious synthetic procedures. Moreover, the morphology of the synthesized nanomaterial is not tunable.

Herein, we developed a synthetic approach for making hollow silica nanomaterials with tunable morphologies by using PVP-water droplets as the soft templates. Three morphologies with hollow interiors, including tadpole-like, wire-like, and spheres, were obtained easily by changing the applied solvent from 1-propanol to 1-pentanol, or ethanol, respectively. In addition, we demonstrated that molar ratio of NH_4OH to TEOS and reaction time could also be used as factors to tune the morphology of produced nanomaterials. The effect of various factors on the morphology was systematically studied to propose a growth mechanism. The potential application of the developed hollow nanomaterials was investigated by taking the hollow spherical silica nanomaterials as an example to study its drug-carrying ability. Using inexpensive and commercially available reagents, the newly developed one-step synthetic strategy shows significantly high reproducibility that brings great potential for a large-scale synthesis.

2. Experimental Section

2.1. Chemicals and Instruments.

Tetraethylorthosilicate (TEOS, 98%) was purchased from Aldrich. Ammonium hydroxide (28.0% – 30.0%), absolute ethanol (99%) and ethanol (95%) were obtained from Fisher Scientific Co. Sodium citrate (Na_3Ct), 1-propanol, 1-pentanol and polyvinylpyrrolidone (PVP, average molecular weight Mn = 40,000) were purchased from Alfa Aesar. Tris(bipyridine)ruthenium (II) dichloride (Rubpy) was purchased from ICN Biomedicals Inc.*E. Coli* HB101 strain (genotype: F-, thi-1, hsdS20 (rB-, mB-), supE44, recA13, ara-14, leuB6, proA2, lacY1, galK2, rpsL20 (strr), xyl-5, mtl-1) was obtained from American Tissue Culture Collection (ATCC) and polymyxin B was purchased from MPBio. Deionized water (Millipore Milli-Q grade) with resistivity of 18.2 MΩ·cm was used in all experiments.

2.2. Characterization.

A Hitachi 7500 transmission electron microscope (TEM) and a Hitachi SU8010 field emission scanning electron microscope (SEM) were used to take images of the developed silica nanomaterials. The fluorescence intensities of the synthesized fluorescent silica nanomaterials were measured using a Jobin Yvon Horiba Fluorolog spectrofluorometer. The Carl Zeiss LSM 510 Meta laser scanning confocal microscope was used to observe Rubpy-doped hollow silica nanoparticles. The elemental analysis was achieved by performing energy dispersive X-ray spectroscopy (EDS) measurements using an Oxford X-Max EDS that is attached to the Hitachi SU8010 field emission SEM. Powder X-ray diffraction patterns (XRD) of the synthesized nanomaterials were recorded on a Rigaku Ultima IV diffractometer with PDXL software. The diffraction patterns were collected at room temperature using Ni filtered Cu Kα radiation of wavelength 1.5408 Å with accelerating voltage of 40 kV,

and emission current of 44 mA. The angle regions were scanned from 10 to 80º (2θ) with a step size of 0.02º at a scan rate of 1º/min. The Beckman DU® 640 spectrophotometer was used to measure the optical density (OD) of the LB bacterial suspensions in the kinetic study for the determination of the bacterial growth curve.

2.3. Synthesis of Hollow Non-Spherical Silica Nanomaterials (HNSNs).

2.3.1. Synthesis of Hollow Silica Tadpole-like Nanomaterials.

Monodispersed hollow silica tadpole-like nanomaterials were prepared by using 1-propanol as the solvent. A mixture of 3.00 g PVP and 30.00 mL of 1-propanol was sonicated for 30 min until all PVP was dissolved. An aliquot of 3.00 mL of 95% ethanol, 0.84mL H_2O, and 0.20 mL of 0.17 M Na_3Ct was added into the PVP/1-propanol mixture and gently shaken by hand, followed by the addition of 0.30 mL TEOS and 0.60 mLNH_4OH. The mixture was left to rest and the reaction was allowed to proceed overnight at room temperature. The tadpole-like nanomaterials were collected by centrifuging at 3,000 rpm for 30 min. The supernatant was removed and the precipitates were washed 3 times with ethanol for 20 min at a centrifuge speed of 3,000 rpm.

2.3.2. Synthesis of Hollow Silica Nanowires (HSiNWs).

The synthetic procedures were the same as the synthesis of hollow tadpole-like nanomaterials except for changing the solvent from 1-propanol to 1-pentanol and adding 0.10 mL instead of 0.60 mL of NH_4OH. By changing the molar ratio of NH_4OH to TEOS from 0.53, 1.60, 2.67, 3.73, 4.80, to 5.87, different shapes of silica nanomaterials can be obtained.

2.4. Synthesis of Hollow Spherical Silica Nanomaterials (HSSNs).

Monodispersed HSSNs were prepared using EtOH as the solvent. A total of 0.50 g PVP was added to 10.00 mL of absolute ethanol and the mixture was sonicated

until all the PVP was dissolved. A 0.40 mL aliquot of $H_2O$and 0.10 mL of 0.17 M Na_3Ct were added into the PVP-ethanol mixture followed by the addition of 0.40 mL of NH_4OH and 0.15 mL of TEOS. The mixture was shaken by hand gently and then left to rest for overnight reaction at room temperature. HSSNs were collected by centrifuging at 3,000 rpm for 30 min. The supernatant was removed and the precipitates were washed 3 times with ethanol for 20 min. The calcination process at 500 - 600 °C for 4 h can remove the PVP to obtain HSSNs. For the synthesis of dye-doped HSSNs, 0.40 mL of 10.00mM Rubpy solution was added instead of 0.40 mL H_2O and the reaction was carried out in the dark. Rubpy-doped HSSNs were collected by centrifuging at 3,000 rpm for 30 min and the precipitates were washed 3 times by ethanol. After carefully removing the supernatant, the Rubpy-doped HSSNs were re-dispersed in 10 mL water for fluorescence intensity measurement. The fluorescence intensity of pure Rubpy aqueous solution (0.03 mM) and pure HSSNs (0.05 mg/mL) were measured as controls. For the synthesis of polymyxin B-doped HSSNs, 0.40 mL of 5.00 mg/mL polymyxin B solution was added instead of 0.40 mL H_2O.

2.5. Monitoring of the Formation Process of Hollow Silica Nanomaterials at Different Reaction Times.

The intermediates of the hollow nanomaterials were collected at different reaction times to study their formation process. The synthetic procedures were the same as described in Section 2.4. When using 1-propanol as the solvent, a 5.00 mL aliquot of synthetic solution was collected each time when the reaction had proceeded for 5 min, 10 min, 1 h, and 16 h; the same amount was also taken at 1 h, 2 h, 3 h, 5 h, and 16 h with 1-pentanol as the solvent. The collected solutions were centrifuged at 3,000 rpm for 30 min and the supernatant was subsequently removed. The precipitates were washed 3 times by ethanol and re-dispersed in distilled water.

2.6. Antibacterial Experiments in LB Plates.

A 0.05mL aliquot of *E. coli* suspension was mixed with 0.05mL of 2.00 mg/mL HSSNs, pure water, or polymyxin B-doped HSSNs with a concentration of 1.00, 0.50, 0.25, and 0.10 mg/mL, respectively. Each as-prepared 0.10 mL bacteria-sample mixture was evenly spread on the surface of LB-agar dishes. The dishes were then placed in an incubator for 24 h at 37 °C.

2.7. Bacterial Kinetic Study.

A 0.05mL aliquot of *E. coli* suspension was added to 5.00 mL LB followed by the addition of different samples. The final concentrations of the samples was 0.040 mg/mL pure HSSNs, 0.005, 0.020, and 0.100 mg/mL polymyxin B-doped HSSNs. Water and pure HSSNs were used as controls. The initial time of adding each sample to LB bacterial suspension was recorded as zero. The suspension was incubated at 37 °C at a shaking speed of 200 rpm. At each set time interval, a 0.20 mL aliquot of the suspension was withdrawn from the incubator and placed in a cuvette containing 1.80 mL of LB broth. Then, an OD measurement at a wavelength of 600 nm was performed to estimate the amount of bacteria present in the samples.

3. Results and Discussion

3.1. Synthesis of Hollow Non-Spherical Silica Nanomaterials (HNSNs).

Two distinct morphological non-spherical silica nanomaterials, hollow tadpole-like and hollow silica nanowires (HSiNWs), were obtained by using 1-propanol and 1-pentanol as the solvent, respectively. In a typical synthetic process, PVP was first dissolved in the solvent and followed by the addition of Na_3Ct, H_2O, and NH_4OH. The formation of a silica shell was initiated by the addition of TEOS that acted as the silica precursor.

When 1-propanol was used as the solvent, the resulting hollow nanomaterials

showed a tadpole-like shape (Figure 1A - B). They possessed a relatively round shape at one end, resembling the head of a tadpole, and the hollow structure gradually became thinner towards the other end, resembling the tail of a tadpole. The average diameter of the head parts was 235 ± 35 nm with a silica shell thickness of 58 ± 9 nm. The diameter and the silica shell thickness of the tail parts were 64 ± 5 nm and 23 ± 5 nm, respectively. The shape of the product was uniform. Over 99% of the produced nanomaterials had the tadpole-like morphology. The hollow structure can be clearly observed from both the TEM image (Figure1A) and the broken nanomaterials in the SEM image (Figure1B, red arrows).

Ultra-long silica nanowires (HSiNWs) were obtained when changing the solvent to 1-pentanol as shown in Figure 1C and D. The nanowires have a typical length up to tens of micrometers and a diameter ranging from 60 to 100 nm. The hollow structures can be clearly observed either from the TEM (Figure 1C) or some broken HSiNWs in the SEM image (Figure 1D, red arrows). It is also noteworthy that the HSiNWs can bend dramatically without breaking into small pieces, showing their excellent flexibility.

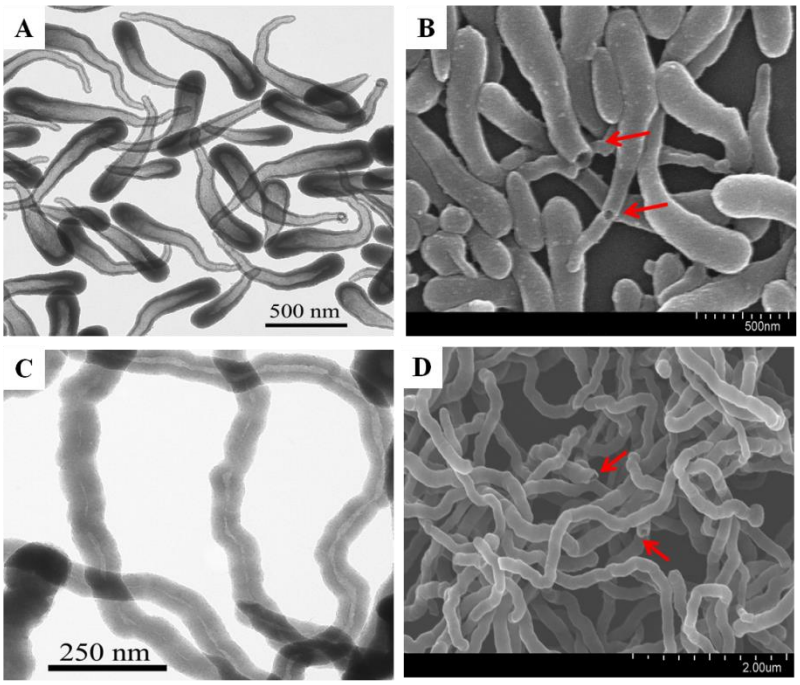

Figure 1. TEM and SEM images of obtained hollow silica tadpole-like nanomaterials (A and B) and hollow silica nanowires (C and D) by using 1-propanol or 1-pentanol as the solvent, respectively. TEM images: A and C, SEM images: B and D.

The chemical composition and crystalline property of the hollow silica nanomaterials were investigated using EDS elemental analysis and powder X-ray diffraction patterns (XRD). The hollow nanomaterials with different shapes showed similar chemical composition and crystalline property. Here the results for the HSiNWs were presented as an example. The EDS spectrum in Figure 2A was obtained from a single nanowire of the indicated yellow area on the SEM image (Figure 2A inset). The EDS analysis demonstrated that the nanowire contained Si and O with an approximate atomic ratio of Si : O = 1 : 2. The XRD pattern of the synthesized HSiNWs was shown in Figure 2B. The scattering pattern exhibited one broad peak ranging from 15 to 30º with the peak value at 2θ angle of 24º, indicating the amorphous nature of the HSiNWs.

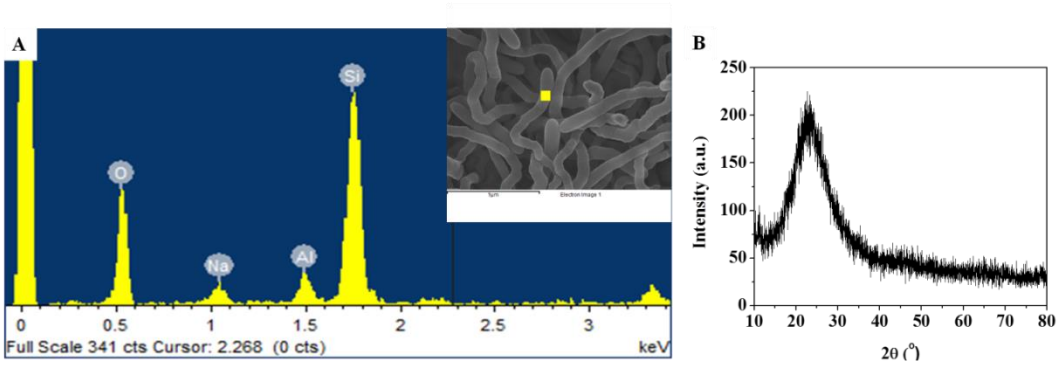

Figure 2. A EDS spectrum (A) and the XRD pattern (B) of the synthesized HSiNWs.

One-dimensional amorphous HSiNWs are good candidates for photoluminescent materials due to their unique blue light emission.[25-29] It is also reported that the photoluminescence intensity is two orders of magnitude higher than that of oxidized silicon nanowires.[30] The optical properties of silica nanowires were also investigated in our study. Figure 3a shows the photoluminescence excitation spectrum of the synthesized silica nanowires. It has a strong peak around 330 nm, therefore, it was used as the excitation wavelength for the following photoluminescence emission study. From the obtained emission spectrum (Figure 3b), two characteristic peaks are observed at the wavelength of 450 (2.76 eV) and 540 nm (2.30 eV). According to discussion provided by Nishikawa *et al.*[31] and Liao *et al.*[32], the 2.76 eV band is ascribed to the neutral oxygen vacancy (O≡Si-Si≡O) defects in amorphous silica. For the band near 2.3 eV, the self-trapped excitons and the nature of the self-trapped excitons are governed by the structure of the SiO_4 tetrahedron.[33] A relatively weak peak around 410 nm (3.0 eV, not shown here) is also observed, which can be attributed to some intrinsic diamagnetic defect centers, such as the two fold coordinated silicon lone pair centers (O-Si-O).The photoluminescence property of the silica nanowires may have great potential applications in integrated optics.

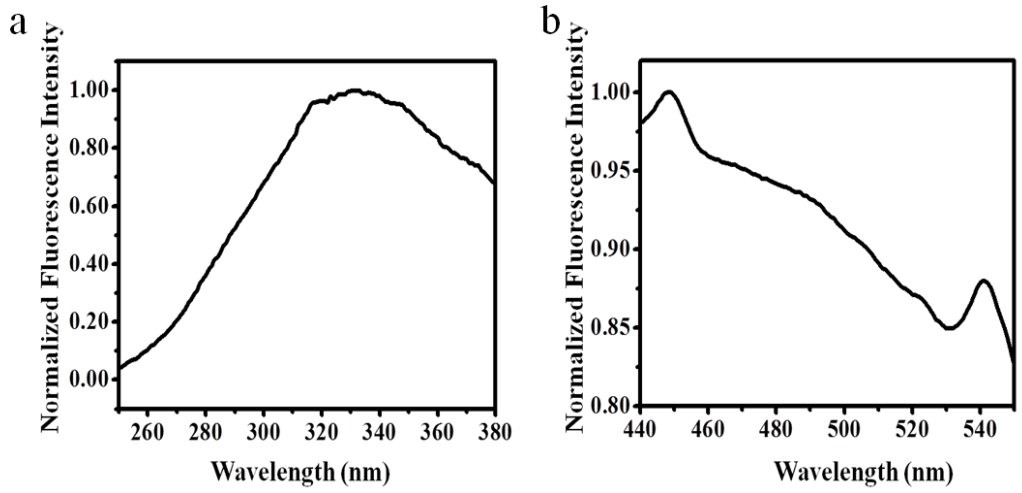

Figure 3. The excitation (a) and emission (b) spectra of the as-synthesized silica nanowires.

3.1.1. Effect of Molar Ratio of NH_4OH to TEOS.

Analogous to the classic sol-gel process, NH_4OH was used as a basic catalyst for the hydrolysis of TEOS. In addition, NH_4OH has also been reported as a morphological catalyst reagent.[34] The amount of NH_4OH in the reaction medium has a pronounced influence on integrity and surface morphology of the synthesized silica nanomaterials. A wide range of the molar ratios of NH_4OH to TEOS (0.53, 1.06, 2.12, 3.18, 4.24, and 5.30) was investigated (Figure 4) in the 1-propanol solvent system. At a low molar ratio of NH_4OH to TEOS (0.53, Figure 4A) hollow crushed-microballoon-like particles with thin shells were obtained. As the molar ratio of NH_4OH to TEOS (1.06) increased, the particles became more spherical with a thicker silica shell. Meanwhile, some of the particles started to grow tails to form tadpole-like structures (Figure 4B). When the molar ratio of NH_4OH to TEOS reached 2.12, a tadpole-like structure formed (Figure 4C). With further increasing the molar ratio of NH_4OH to TEOS (3.18, 4.24 and 5.30), the head of the particle became more solid while the tail kept the hollow structure and grew longer (Figure 4D – F).

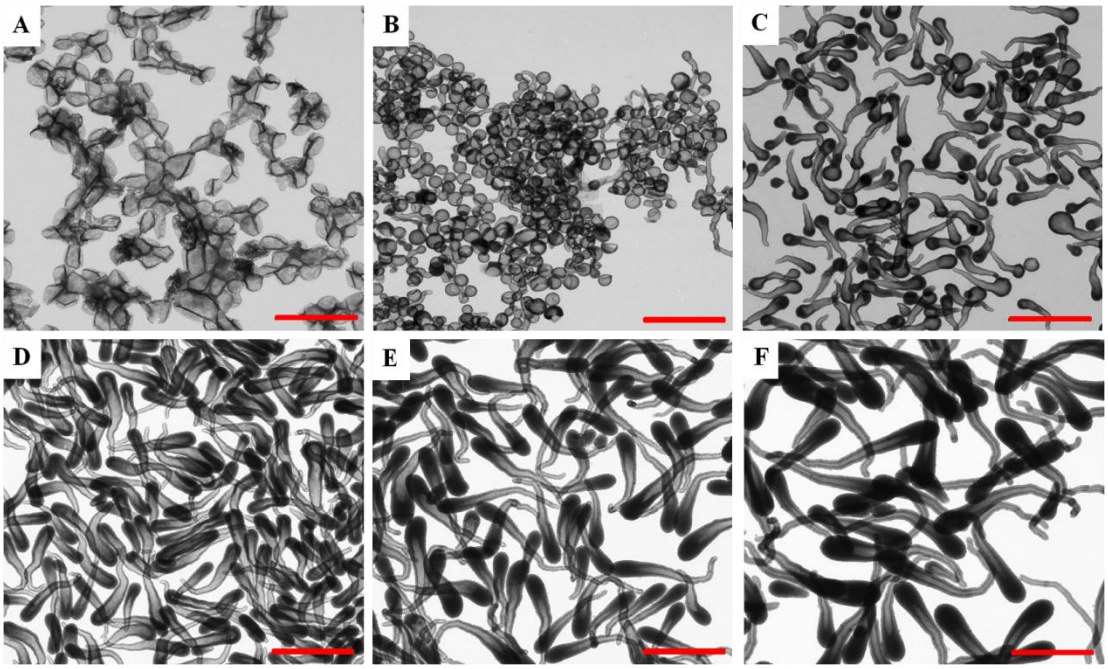

Figure 4. TEM images of the hollow silica nanomaterials prepared using 1-propanol under various molar ratios of NH_4OH to TEOS. From A to F, the molar ratio of NH_4OH to TEOS was 0.53, 1.06, 2.12, 3.18, 4.24, and 5.30, respectively(scale bar: 1μm).

When 1-pentanol was used as the solvent, ultra long and amorphous HSiNWs were obtained (Figure 5A – C) at relatively low molar ratios (0.53 and 1.60). Differences were revealed under high magnification TEM images in these two molar ratios of NH_4OH to TEOS (Figure 5B – C). In a molar ratio of 0.53, silica nanowires with hollow nanostructures were obtained (Figure 5B) while only solid nanowires were synthesized in the molar ratio of 1.60 (Figure 5C). As the molar ratio of NH_4OH to TEOS increased to 2.67, 4.80, and 5.87, solid silica nanorods and nanoparticles were synthesized (Figure 5D – F). The above results might be explained by different TEOS hydrolysis and condensation rates under various NH_4OH to TEOS molar ratios. The condensation of TEOS was fast at low molar ratios of NH_4OH to TEOS, in which the by-products (ethanol and water molecules) were unable to diffuse into the relatively nonpolar solvent (pentanol) timely and were trapped inside of the newly formed nanowires. With several washings, the spaces occupied by these encapsulated

small by-products became hollow parts of the nanowires. The rough surfaces of the HSiNWs also indicated they were not formed by slow thermodynamic controlled processes. In contrast, the condensation rate probably decreased at a high molar ratio of NH_4OH aqueous solution to TEOS due to the large excess of NH_4OH and the water introduced at the same time. Therefore, no by-product or PVP-water mixture was trapped inside of the nanomaterials (Figure 5C – F). The observation of solid nanowires, nanorods and nanoparticles at high molar ratio of NH_4OH to TEOS was consistent with Kuijk's report.[35] The formation of such long HSiNWs was quite challenging and the one-pot process reported herein is not only novel but also facile and reliable.

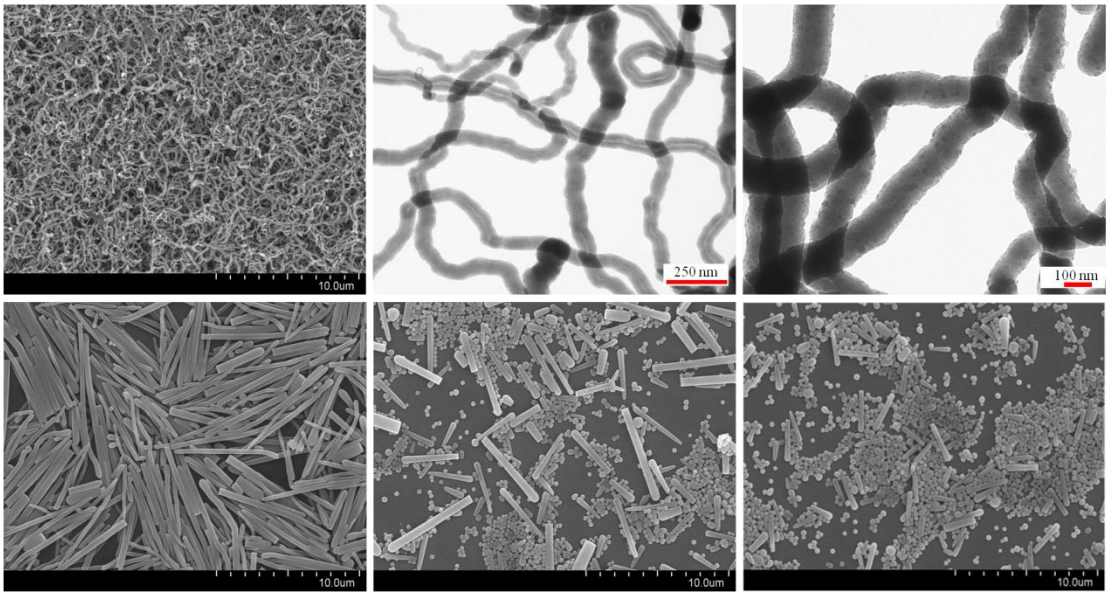

Figure 5. SEM (A, D – F) and TEM (B and C) images of the synthesized silica nanomaterials by changing the molar ratio of NH_4OH to TEOS from 0.53 (A,B), 1.60 (C), 2.67 (D), 4.80 (E), to 5.87 (F), respectively. 1-pentanol was used as the solvent.

3.2. Formation Process of Hollow Non-Spherical Silica Nanomaterials.

To study the formation process of silica nanomaterials in different solvents and propose a possible growth mechanism, the intermediates were collected at different reaction intervals and then were characterized using TEM. These TEM

images clearly revealed the evolution process of the products.

3.2.1. Hollow Tadpole-like Silica Nanomaterials.

At the initial stage (5 min after the addition of TEOS) the products showed hollow hemispheres with one side open (Figure 6A). After 10 min of the reaction, the silica shell grew thicker at one side, forming a head of the tadpole (Figure 6B). By increasing the reaction time to 20 min, the length of the nanomaterials increased dramatically (Figure 6C) and a hole formed at the tail. The length of the tadpole kept growing within 1 h (Figure 6D) until the hole at the end of the tail was closed. With a further increase in the reaction time to 16 h, the size of the tadpole only showed slight changes.

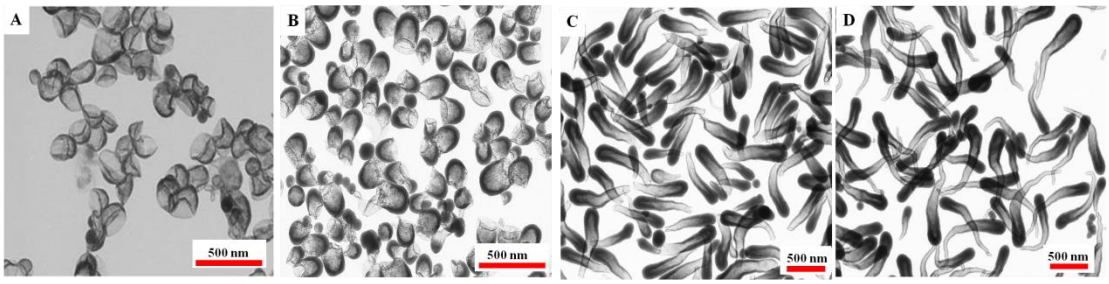

Figure 6. TEM images of the silica tadpole-like nanomaterials in the formation process, preceding the reaction for (A) 5 min, (B) 10 min, (C) 20 min, and (D) 1 h, respectively.

3.2.2. Hollow Silica Nanowires.

At the early stage of hollow nanowire growth (1 h), the produced hollow nanomaterials were more likely to have spherical shapes as shown in Figure 7A. It is noteworthy that the thickness of the silica shell in this stage was not uniform. After 2 h of reaction, a silica tail appeared at the thinner shell area and began to grow along the direction (Figure 7B – C). Long HSiNWs were formed by further reaction until TEOS was completely consumed (Figure 7D – E). The steep increase in the length of the HSiNWs was observed during the first 4 h (Figure 7F). It was difficult to measure the length of HSiNWs after an overnight reaction (16 h) because they were densely

tangled. In both 1-propanol and 1-pentanol systems, spherical-like hollow silica nanomaterials were formed at the initial stage, which proved the existence of PVP-water droplets and the hydrolysis and condensation on the surface of the droplets.

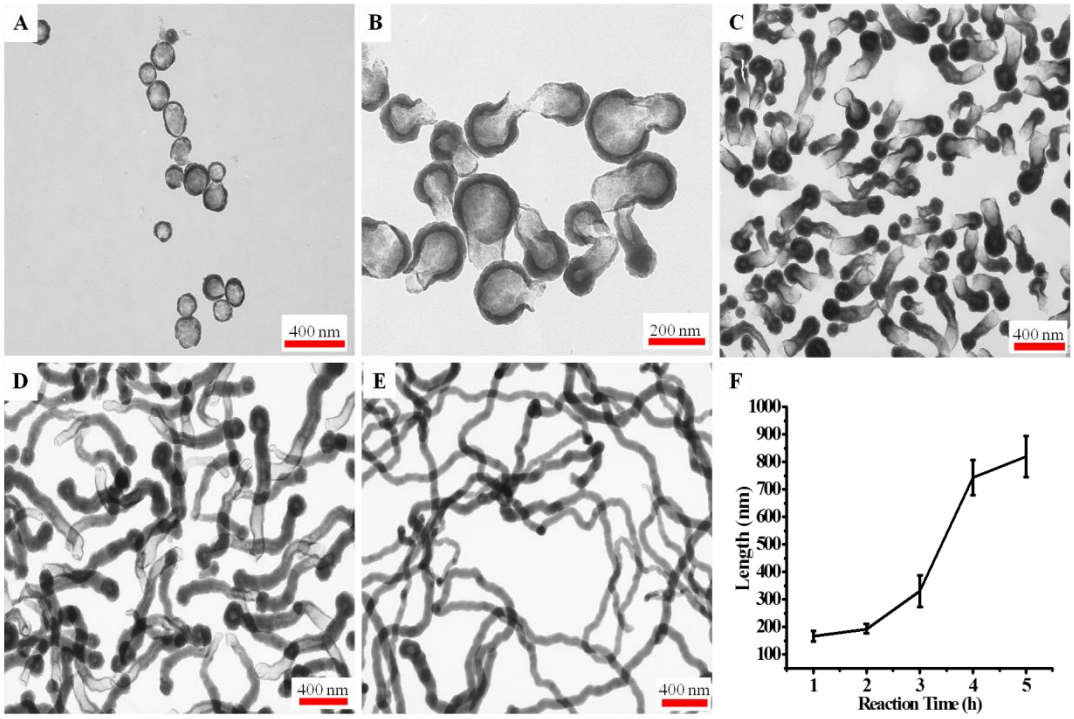

Figure 7. The growth of HSiNWs observed at different reaction times. (A) 1 h, (B) 2 h, (C) 3 h, (D) 5 h, (E) 16 h, (F) the length changes of products vs the reaction time.

3.3. Synthesis of Hollow Spherical Silica Nanomaterials (HSSNs).

The HSSNs could be synthesized by changing the applied solvent to EtOH. As shown in Figure 8, monodispersed HSSNs with a relatively uniform size and smooth surface were obtained. The average diameter of the particles in Figure 8 was 365 ± 49 nm. The hollow structure of these spherical particles can be revealed by the contrast between the dark outlier and the pale inner in the spheres (Figure 8A). The hollow structure was also observed in broken particles in the SEM image (red arrows in Figure 8B).

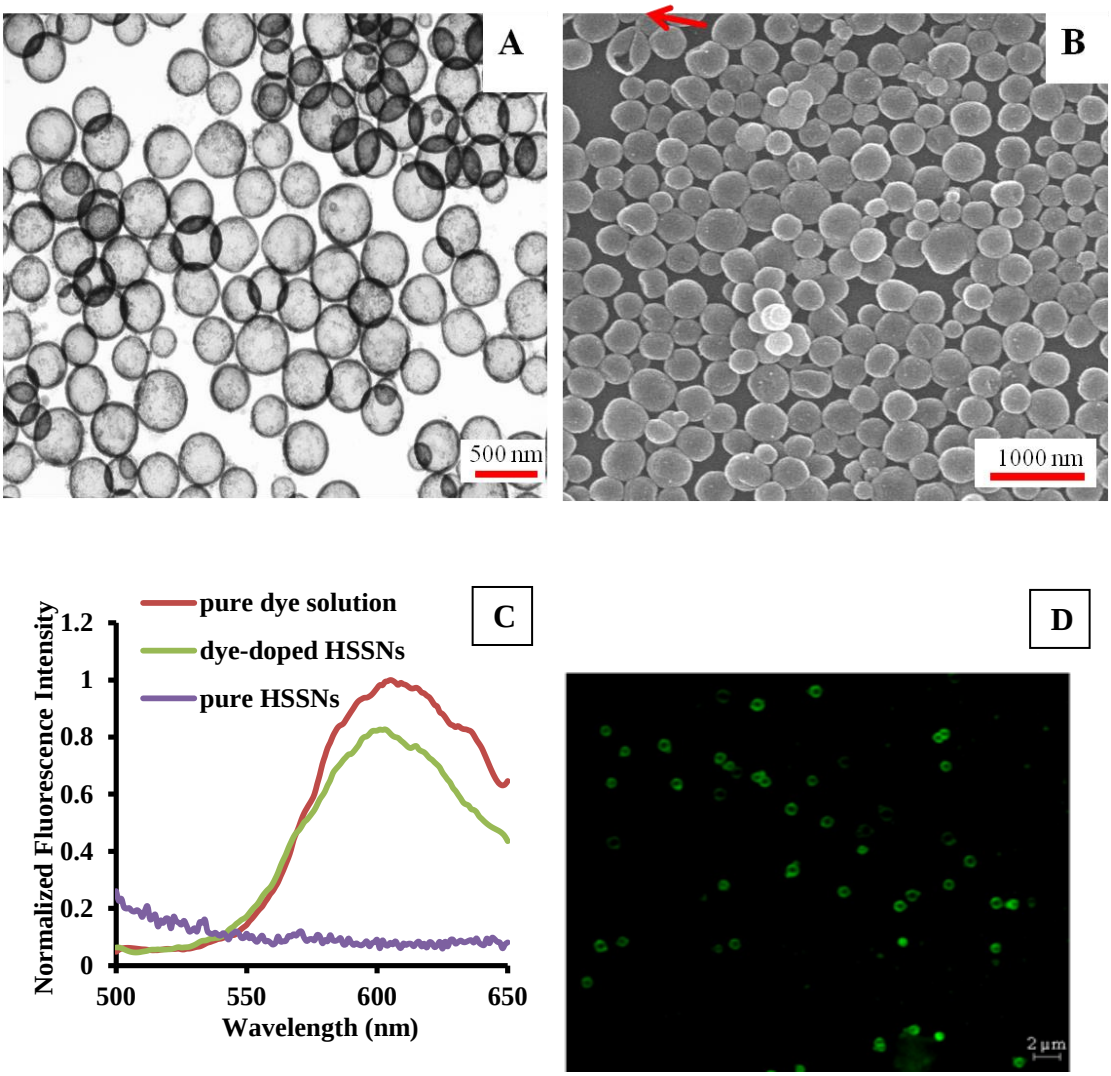

Figure 8. (A) TEM and (B) SEM images of synthesized HSSNs by using ethanol as the solvent, (C) Fluorescence spectra of pure Rubpy, Rubpy-doped HSSNs, and pure HSSNs in aqueous solutions as described in Section 2.3. Excited at 488 nm with emission range from 500 to 650nm. Slit: 2 nm. (D) Confocal fluorescence image of Rubpy–doped HSSNs. The fluorescence image was taken using a 100× objective lens with an excitation wavelength of 488 nm and a 585 nm long pass emission filter.

To further confirm the hollowness of the particles, we visually observed the hollow nanostructure through fluorescence imaging. A positively charged fluorescent dye, Rubpy, was doped into the silica shell during the synthesis of HSSNs. Due to the strong electrostatic interaction between the negatively charged silica and the positively charged dye molecules, Rubpy would be trapped in the silica shell and guaranteed the high encapsulation efficiency. The encapsulating of Rubpy in the silica

shell was studied by fluorescence measurements (Figure 8C) and confocal fluorescence imaging (Figure 8D). The characteristic fluorescence emission peak of Rubpy at 605 nm in the fluorescent spectra and a ring-like structure in the confocal fluorescence imaging demonstrated the hollow structure of the particles since only the fluorescent labeled silica shell was visible.

3.3.1. Effect of Molar Ratio of NH_4OH to TEOS.

The molar ratio of NH_4OH to TEOS (the amount of TEOS was fixed) was varied from 1.06, 2.12, 3.18, 4.24, 5.30, to 6.36 to study the effect of molar ratio on the formation of the HSSNs (Figure 9). Without NH_4OH in the reaction system, no nanoparticles were obtained due to the slow hydrolysis of TEOS. At low molar ratios of NH_4OH to TEOS (1.06 and 2.12), the products were deformed and aggregated as shown in Figure 9A – B. The deformed silica structures seemed to be the broken thin shell HSSNs because they were too fragile to survive during the sequential workup. When the molar ratio was increased to 3.18, a large number of HSSNs was observed (Figure 9C). However, some of them had open ends rather than intact HSSNs. With further increasing the ratio of NH_4OH to TEOS to 4.24 and 5.30, perfectly intact HSSNs were synthesized (Figure 9D – E). If the molar ratio further increased to 6.36, the majority of the products became solid silica nanoparticles as shown in Figure 9F and the silica shell of HSSNs became much thicker. By changing the molar ratio of NH_4OH to TEOS, the silica shell thickness increased from 23.02 nm ± 3.1 nm (Figure 9D), 32.8 nm ± 2.2 nm (Figure 9E), to 50.6 ± 2.9 nm (Figure 9F), respectively.

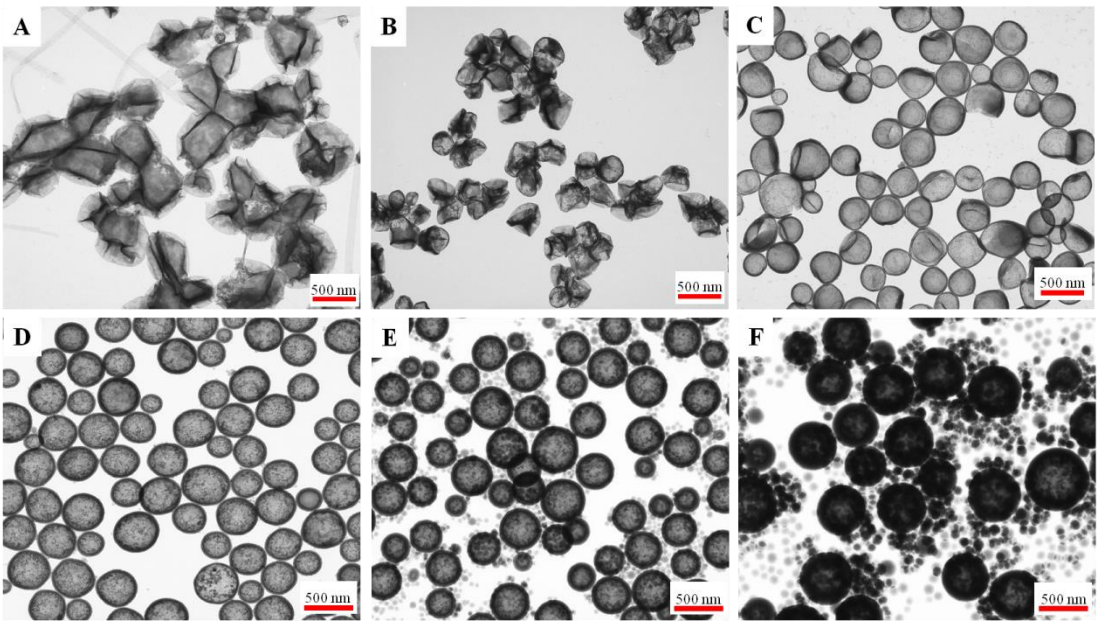

Figure 9. TEM images of the HSSNs prepared under various molar ratios of NH_4OH to TEOS by applying ethanol as the solvent. From A to F, the molar ratio of NH_4OH to TEOS is 1.06, 2.12, 3.18, 4.24, 5.30, and 6.36, respectively. The experiment was performed by changing the amount of NH_4OH while other conditions were fixed.

3.4. The Role of PVP on the Formation of the Hollow Structure.

The effect of PVP concentration on the formation of hollow nanomaterials was investigated. The HSSNs was taken as an example. In the absence of PVP, solid silica nanoparticles without hollow interior were obtained as shown in Figure 10A. In the presence of different concentrations of PVP varying from 31.3 wt%, 62.5 wt%, to 125 wt%, the HSSNs were successfully synthesized. When the concentration of PVP was 31.3 wt% (Figure 10B), which was lower than the minimum PVP-water binding concentration (57 wt%),[36] a limited number of water molecules bound to PVP. Therefore, the majority of the synthesized nanomaterials were solid silica nanoparticles (inset TEM image in Figure 10B) with a few HSSNs. As the concentration of PVP increased to 62.5 wt%, well-dispersed HSSNs were obtained as shown in Figure 10C. All hollow nanoparticles appeared as a spherical morphology with uniform size. When the concentration of PVP further increased to 125 wt% (Figure 10D), no significant morphological change was observed except for a slight

decrease in size from 365 ± 49 nm to 359 ± 55 nm.

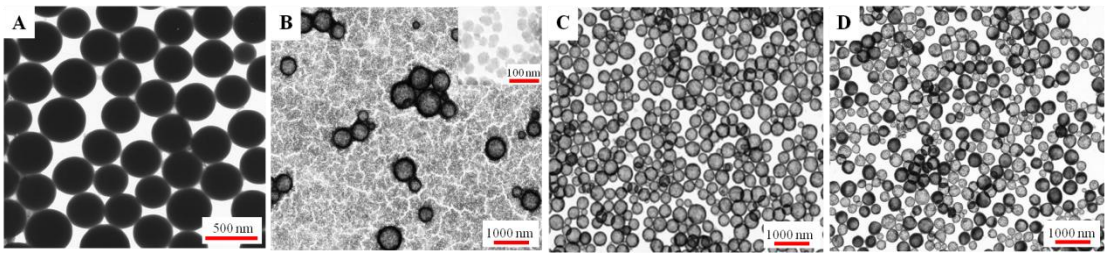

Figure 10. TEM images of silica nanoparticles obtained at different concentrations of PVP: (A) 0 wt%, (B) 31.3 wt%, (C) 62.5 wt%, and (D) 125 wt%. Inset image in B: solid silica nanoparticles.

3.5. Possible Mechanism.

A possible mechanism of the formation of hollow nanomaterials with tunable morphologies was proposed based on the above results (Scheme 1). The formation of PVP-water droplets and intrinsic properties of applied solvents play critical roles in the synthesis process. PVP is an amphiphilic, non-ionic polymer, which is soluble in water and many non-aqueous solvents due to the presence of a highly polar amide group within the pyrrolidone ring. Therefore, the PVP was commonly viewed as a surfactant and a stabilizer in material synthesis. One important property of PVP is that at a high concentration of PVP (≥ 57 wt%) in aqueous solution, water molecules preferred binding with PVP instead of acting as a solvent, which was referred to as bound water. When TEOS was added, its hydrolysis and condensation took place at the interface of the hydrophobic phase and the PVP-water droplets. The hydrolyzed $Si(OH)_x(OCH_2CH_3)_{4-x}$ molecules were polar and tended to accumulate at the oil-water interface of the emulsion. As the hydrolysis and condensation continuously proceeded, the resulting silica assembled on the surface of PVP-water droplets, eventually resulting in a hollow interior after the removing of PVP-water droplets.

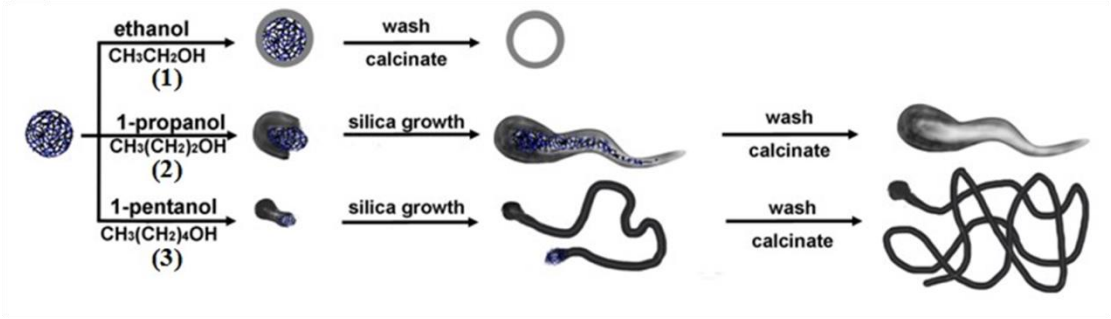

Scheme 1. The formation of hollow nanomaterials in different solvents: ethanol (1), 1-propanol (2), and 1-pentanol (3).

The morphology of synthesized nanomaterials changed dramatically with different applied solvents. Ethanol is the most commonly used solvent to obtain spherical silica nanoparticles based on the TEOS hydrolysis and condensation as follows:[37]

$$Si(OCH_2CH_3)_4 + 4H_2O \leftrightarrow Si(OH)_4 + 4EtOH \qquad [1]$$

$$nSi(OH)_4 \leftrightarrow nSiO_2 + 2nH_2O \qquad [2]$$

The produced EtOH and H_2O are homogeneously miscible with the solvent EtOH. Thus the surface tension of PVP-water droplets barely changed. Therefore, perfectly spherical-shape hollow nanomaterials were obtained in the ethanol-solvent system (Scheme 1, (1)). On the contrary, if the produced EtOH and H_2O are not homogeneously miscible with the solvent, the surface tension of PVP-water droplets would change in the formation of the silica shell thus the shape of the PVP-water droplets would change, resulting in different morphologies of the silica shell (Scheme 1, (2) and (3)).

When 1-propanol was used as a solvent, although it is also miscible with H_2O, the combined solution was far from homogeneous.[38] In this case, some produced water molecules would prefer binding with PVP rather than dispersing into the surrounding solvent. Thus the surface tension of PVP-water droplets would be changed. As the anisotropic supply continued to hydrolyse and condense, the

PVP-water droplets were deformed where the silica grew along, resulting in a tadpole-like shape (Scheme 1, (2)).

Unlike ethanol and 1-propanol which are miscible with water, 1-pentanol is immiscible with water and its solubility in water is only 2.19 wt%.[39] Therefore, the produced ethanol and water molecules were unable to timely diffuse into the relatively nonpolar solvent pentanol and trapped inside of the newly formed nanowires. The spaces occupied by these encapsulated small by-products became hollow parts of the nanowire after workup. Meanwhile, the PVP-water droplets kept in the end of the nanowire and the silica continued to grow along the direction, resulting in an ultra-long wire-shape nanostructure (Scheme 1, (3)).

3.6. Potential Applications of the Hollow Silica Nanomaterials.

Hollow nanomaterials are of great interests for applications in drug delivery and catalysis. To investigate potential applications of the developed hollow nanomaterials, the HSSNs were selected as an example to study its drug-carrying ability. In this work, we studied if drugs could maintain their activity after being encapsulated in the HSNs.

Polymyxin B, a well-known drug for its biocidal activity on a number of bacteria, was chosen as a model drug. The antimicrobial efficacy of the polymyxin B-doped HSNs was examined against gram-negative *E. coli* bacteria, which has been used as a model bacterial system for various antimicrobial tests. Without addition of polymyxin B-doped HSNs, a full bacterial layer on the surface was observed (Figure 11, 1 and 6). However, in the dish with the highest concentration of polymyxin B-doped HSNs (Figure 11, 2), the dish surface was completely free from bacteria. As the concentration of the polymyxin B-doped HSSNs decreased, bacterial colonies gradually increased (Figure 11, 3 – 5).

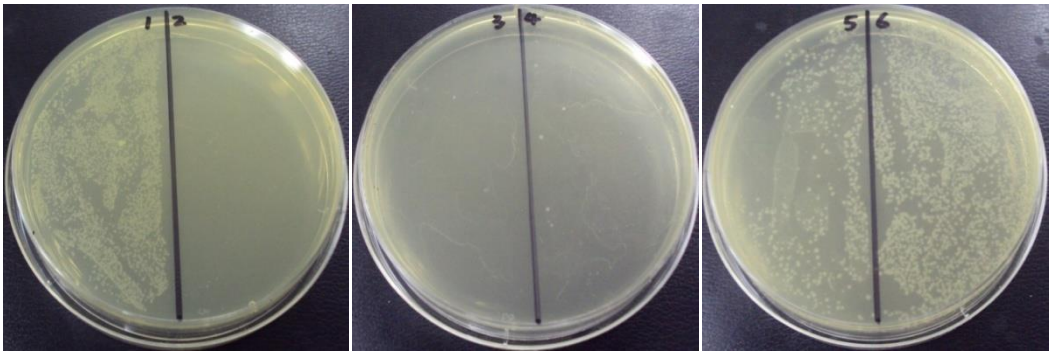

Figure 11. Antibacterial function of the polymyxin B-doped HSSNs toward gram-negative *E. coli* bacteria. Photographs were taken after incubation for 24 h at 37 °C. The samples (each sample is ½ of the agar dish) from left to right were: 1) pure water; 2 - 5) polymyxin B-doped HSSNs with a concentration of 0.500, 0.250, 0.125, and 0.050 mg/mL, respectively; 6) 2.000 mg/mL pure HSSNs.

We further quantitatively evaluated the antibacterial activity of the polymyxin B-doped HSSNs by studying the growth kinetics of bacteria in a LB liquid medium. The bacterial proliferation was measured using OD600 based on the turbidity of the cell suspension within 24 h. The growth curve showed a typical concentration-dependent antibacterial effect of the polymyxin B-doped HSSNs (Figure 12). The bacteria growth curves in the presence of polymyxin B-doped HSSNs were significantly different from the ones in the two controls media (water and pure HSSNs) in the first 8 h, suggesting strong inhibition of proliferation of *E. coli*. Complete inhibition of *E. coli* growth during the whole 24 h was observed when 0.100 mg/mL of polymyxin B-doped HSSNs was used. These data strongly suggest a long-term antibacterial activity of the polymyxin B after being doped in the HSSNs.

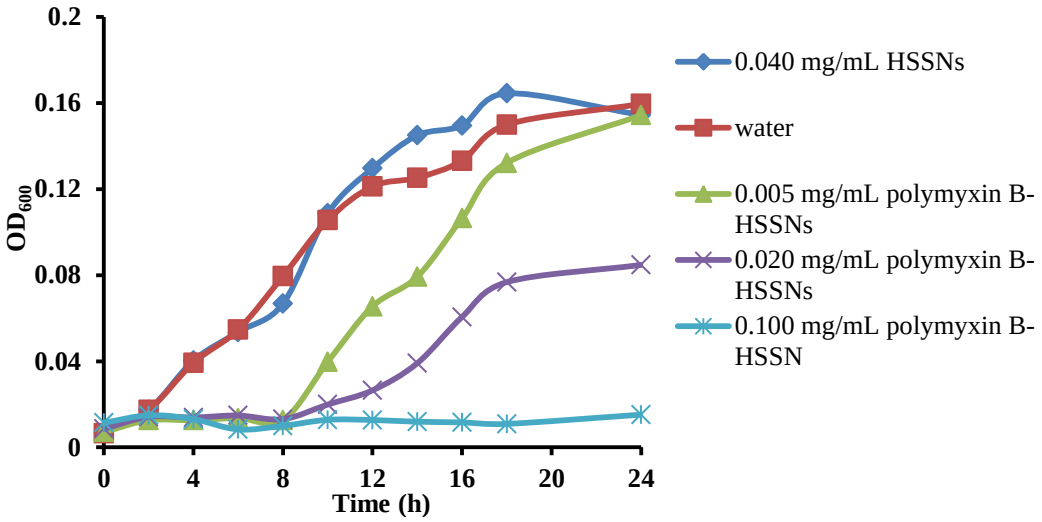

Figure 12. Bacteria growth curves in LB media with pure HSSNs, water and different concentrations of polymyxin B-doped HSSNs. Wavelength: 600 nm.

4. Conclusions

In summary, hollow silica nanomaterials with different morphologies have been successfully synthesized by simply changing the solvent. By using three different solvents, hollow spherical nanoparticles, tadpole-like nanomaterials, and nanowires were obtained, which further generate a broad family of interesting structures. The morphology of synthesized nanomaterials can also be tuned by the molar ratio of NH_4OH to TEOS and reaction time. A mechanism based on the intrinsic properties of solvents, diffusion rates of side-products and the condensation reaction rate of TEOS was proposed. Overall, the newly developed synthetic process is an efficient one-step procedure using inexpensive and commercially available reagents, showing high reproducibility and great potential for a large-scale synthesis. Their application as a drug-carrier was demonstrated using the hollow spherical silica nanoparticles.

CHAPTER II

DEVELOPMENT OF GOLD NANOPARTICLE-ENHANCED FLUORESCENT NANOCOMPOSITES

1. Introduction

Fluorescence-based detection technology, in combination with nanotechnology, has been widely used in biological fields.[40-44] A number of fluorescent nanomaterials, including quantum dots (QDs),[45] upconversion nanoparticles,[46] polymer-based fluorescent nanoparticles,[47-48] and dye-doped silica nanoparticles (DDSN),[42] are of considerable interest as sensors and indicators for biological detections due to their high fluorescence intensity, stability, and easy modification. To further increase fluorescence intensities of nanomaterial-based probes, metal nanostructures have been applied to fabricate metal-dye nanocomposites. It has been proven that the fluorescence can be enhanced by several fold at a certain distance, but quenched in close proximity to a metal nanoparticle.[49-51] Such a fluorescence enhancement phenomenon is well-known as the metal-enhanced fluorescence (MEF) effect. MEF from different metals including silver,[51-54] gold,[49, 55] copper,[56] zinc,[57] chromium,[58] iron,[59] and rhodium[60] has been observed. These metals can be made into different shapes of nanostructures, such as nanoparticles,[51] nanotubes,[61] nanoburgers,[62] and nanorods.[63-64]

However, most MEF applications have been performed on a planar glass substrate,[54, 65-66] which limits their use in biological fields. In 2004, Geddes's group used a SiO_2 matrix to adjust the distance between dye molecules and silver nanoparticles. For the first time the MEF sensing platform was based on solutions

instead of solid substrates.[53] Afterward, a new class of SiO_2-coated silver nanoparticles for MEF study continued to be developed.[50, 67-68] Because of their low toxicity and enhanced-fluorescence intensity, they have become one of the most promising candidates for *in vivo* fluorescence imaging and ultrasensitive analysis. Thus, various types of non-solid substrates based metal-dye nanocomposites are needed.

The mechanisms of MEF have been extensively studied. Several pathways of metal enhancement have been proposed.[43, 69-75] First of all, the occurrence of surface plasmon resonance leads to a strongly enhanced absorption of the incident light. When the surface plasmon resonance band of a metal nanostructure overlaps the excitation of the fluorophores, the energy is transferred from the metal to the fluorophores so that the possibility of excitation of the dye molecules is increased. Secondly, the metal nanostructure can change the radiative deactivation rate of the fluorophores. Thus, the fluorescence lifetime and the quantum yield are changed.[76] Thirdly, the scattering of the metallic nanostructures affects the coupling efficiency of the fluorescence emission to the far field.[77-78] By matching the plasmon resonance band to the fluorophore emission wavelength, a fluorescence enhancement can be obtained.

In spite of these well-developed mechanisms, the rapid development of nanotechnology has produced various new types of metallic nanostructures. These generate a number of new effects of metallic nanomaterials on dye molecular properties, especially the dimensional effects of metallic nanostructures on fluorescence intensity. For instance, in addition to the observation of fluorescence enhancement, a quenching effect was detected by some research groups in the presence of metal nanoparticles. Therefore, the design of new types of metal-dye

nanocomposites may provide useful models for better understanding of the geometric and dimensional effects of metallic nanostructures on fluorescent molecular properties.

In this work, we have developed a new fluorescent metallic nanocomposite for the solution-based MEF. Gold nanoparticles (AuNPs) were chosen based on their high stability and well-studied surface chemistry. This nanocomposite was comprised of an AuNP core, a PVP layer, a silica-spacer shell of variable thicknesses, and a dye molecule-doped silica shell. 5-(and-6)-carboxytetramethylrhodamine-succinimidyl ester (TAMRA-SE) was chosen as the dye molecule because it is one of the most common labeling reagents and its emission and excitation spectra overlap with the absorption of AuNPs. Moreover, the dimensional effect of the metal core on the fluorescence intensity of dye molecules was studied. It is expected that this study may shed light on how to design metal-enhanced nanostructures with desired properties.

2. Experimental Section

2.1. Chemicals and Instruments.

Tetraethylorthosilicate (TEOS, 98%) was purchased from Aldrich. Ammonium hydroxide (28.0% – 30.0%), L-ascorbic acid (99.6%), and ethanol were obtained from Fisher Scientific Co. Sodium citrate (Na_3Ct), gold(III) chloride trihydrate (auric acid, $HAuCl_4 \cdot 3H_2O$, 99.9+%), polyvinylpyrrolidone (PVP-10, average molecular weight of 10 kg/mol), and poly-l-lysine (PLL) solution (0.1% w/v, in water) were purchased from Sigma-Aldrich Inc. carboxytetramethylrhodamine-succinimidyl ester (TAMRA-SE) was purchased from Molecular Probes. Deionized water (Millipore Milli-Q grade) with resistivity of 18.2 MΩ·cm was used in all experiments.

A Hitachi 7500 transmission electron microscope (TEM) was used to take the images of the developed nanomaterials. A Shimadzu UV-250 PC UV-vis spectrophotometer was used to measure the absorption of samples. A Jobin Yvon Horiba Fluorolog spectrofluorometer was employed for fluorescence intensity measurements.

2.2. Synthesis of AuNPs.

AuNPs with various sizes were synthesized according to the standard Na_3Ct reduction method by changing the molar ratio of$Na_3Ct$to auric acid (Na_3Ct:$HAuCl_4$). In a typical synthesis of 13.7 nm AuNPs, 1.0 mL of 0.25 mM $HAuCl_4$ was added to 100.0 mL water. Then, the solution was heated to the boiling point while being stirred. A freshly prepared 4.0 mL of 1.0% Na_3Ct was immediately added into the boiling solution and kept heated until the color changed to wine red, indicating the reaction was completed. Different sizes of AuNPs were obtained by varying the concentration of Na_3Ct at a fixed $HAuCl_4$ concentration.

2.3. Synthesis of the Spacer on the AuNPs.

A silica layer was formed on the AuNP surface as a spacer. The silica coating involved two steps: the adsorption of PVP on the surface of AuNPs and the growth of the silica shell using the Stöber method.[79] The amount of PVP was adjusted based on the size of AuNPs. In the case of coating silica on 13.7 nm AuNPs, 1.0 mL of 0.05 M PVP solution was first mixed with 5.0 mL of 23 nM AuNPs under gentle stirring overnight. After removing the excess PVP by centrifugation, 50.0 mL of 99.0% ethanol, 20 μL of 98.0% TEOS, and 2.5 mL of NH_4OH (28.0% – 30.0%) were added into the PVP-adsorbed AuNP solution. The solution was continuously stirred for 50 min. The thickness of the silica shell was controlled by varying the reaction time or the amount of TEOS.

2.4. Formation of Dye-PLL Complex.

The dye molecules were first linked to PLL to form a dye-PLL complex before doping them into the nanocomposites. An aliquot of 2 μL of 10.0 mg/mL TAMRA-SE in DMSO was added into 1.0 mL of 0.1% PLL. After overnight reaction at room temperature, the dye molecules conjugated with PLL and were ready to be doped into the silica matrix. A final ratio of NH_2 to TAMRA-SE was 200:1.

2.5. Doping Dye-PLL Complex.

The second silica layer was formed outside the silica spacer using the Stöber method. During the formation of this silica layer, the dye-PLL complexes were doped into the silica shell. In this process, an aliquot of 1.0 mL of previously synthesized silica-coated AuNPs was added into 10.0 mL of EtOH, followed by adding 0.5 mL of NH_4OH (28.0% – 30.0%), 5 μL of 98.0% TEOS, and 10 μL of TAMRA-SE-PLL. The solution was stirred in the dark for 3 h.

2.6. Release Dye Molecules from the Nanocomposites.

The silica matrix can be dissolved in a high concentration of NaOH. In a typical experiment, 0.5 mL of 0.4 M NaOH was added into 2.5 mL of dye-doped AuNPs. After stirring for overnight, the nanocomposites were eroded and the bare AuNPs (no citrate ion on the surface) were removed by multiple centrifugations. Then, the dye molecules were released into the supernatant.

3. Results and Discussion

3.1. Design of the Nanocomposite.

The design of the nanocomposite is shown in Scheme 2. A AuNP was selected as the core of the nanocomposite to enhance the fluorescence intensity of dye molecules (Scheme 2a). However, fluorescence energy transfer could occur and thus quench the fluorescence signal of dye molecules if the distance between the dye

molecules and the AuNP is too close. Therefore, a spacer is needed to adjust this distance. A silica layer was selected to perform as the spacer (Scheme 2b). In addition, a silica layer on the AuNP can protect AuNPs from aggregation. However, the formation of the spacer on the AuNP was a challenge. To realize this work, a thin layer of PVP – which assisted in the coating of the silica layer – was first coated on the AuNP. The dye molecules were conjugated to PLL prior to doping the dyes into the 2nd silica layer of the nancomposite. This conjugation can prevent the leaking of dye molecules.

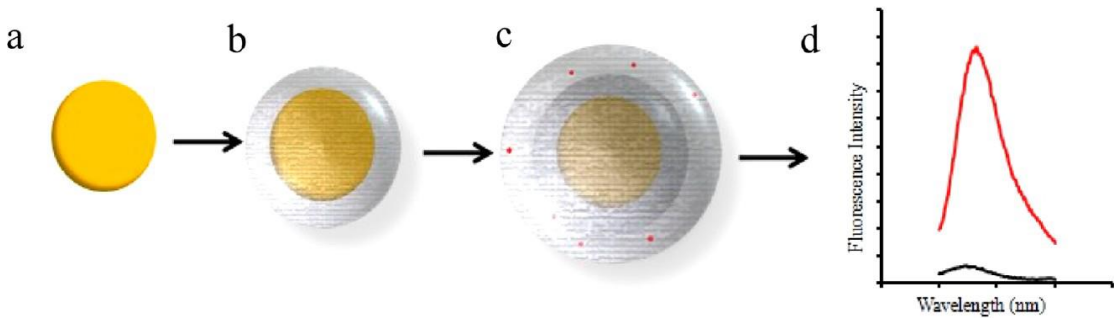

Scheme 2. Schematic illustration of the metal-enhanced fluorescent nanocomposite. (a) A AuNP as a metal core; (b) a silica shell with varied thicknesses coated on the AuNP after the adsorption of the PVP on the surface of AuNP; (c) dye molecules doped during the formation of the second silica layer; (d) the demonstration of the fluorescence enhancement by measuring the fluorescence intensity of the nanocomposites with (top curve) and without the metal core (bottom curve). (red sphere) TAMRA-SE-PLL; (yellow sphere) AuNP; (gray sphere) silica layer.

3.2. Matching Spectra of the Dye Molecules with AuNPs.

To enhance the fluorescence intensity of dye molecules by the metal, it is necessary to have overlap of the metal absorption spectrum with the dye molecule excitation spectrum. The AuNP absorption peak is varied based on the size and shape of the nanoparticles. To fit the objective of this work, it is better to employ different sized AuNPs with similar absorption spectrum. Thus, when studying the size effect of the AuNPs on the fluorescence enhancement, the effect of absorption spectra could be

eliminated. In this work, AuNPs were prepared using the citrate reduction method,[76] which is the most popular and controllable method for synthesizing AuNPs. Different sizes of AuNPs were obtained *via* adjusting the ratio of Na_3Ct to $HAuCl_4$.

In this work, three different sizes of AuNPs were prepared, 33.6 ± 4.3 nm, 19.7 ± 2.2 nm, and 13.7 ± 1.3 nm. These nanoparticles were obtained by adding different amounts of 1% Na_3Ct (1.5, 2.5, and 4.0 mL) with fixed amount of 1% $HAuCl_4$ (1.0 mL). The smallest size was obtained by adding 4.0 mL Na_3Ct, while 1.5 mL was used to obtain the biggest size. These AuNPs were very stable and well-dispersed in an aqueous solution for a long period of time without aggregation (Figure 13, a – c). Here, the monodispersity of the AuNPs benefited from the negatively charged citrate ions on the surface of AuNPs, which provided strong electrostatic repulsion among AuNPs.

The size difference among these three AuNPs was not big enough to cause significant difference in their absorption peaks (Figure 13d, curves 1, 2, 3). A TAMRA-SE dye molecule with an emission wavelength in the red end of the visible range was selected. This emission range is suitable for fluorescence measurements of biological samples. The excitation and emission spectra of TAMRA-SE are shown in Figure 13d (curve 4 and 5). The excitation peak significantly overlaps with the absorption spectra of the three sizes of AuNPs, as desired.

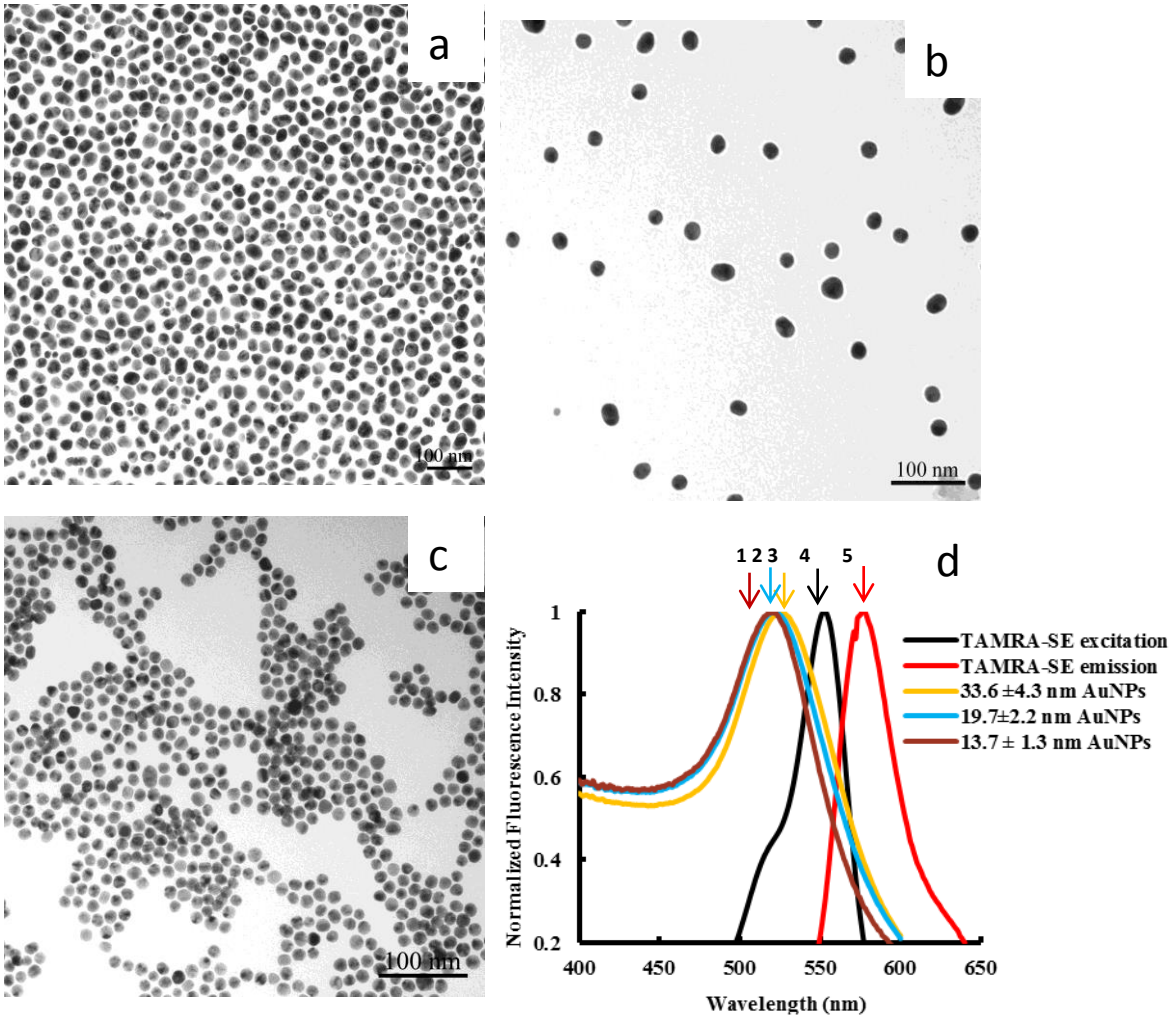

Figure 13. (a – c) TEM images of different sized AuNPs; (d) spectra of different sized AuNPs (curves 1 – 3) and TAMRA-SE. (curve 4: fluorescence excitation spectrum, curve 5: fluorescence emission spectrum). λ_{ex} = 540 nm with a slit width of 5 nm.

3.3. Formation of the Spacer in the Nanocomposite.

To achieve the fluorescence enhancement, a suitable distance between the metal nanoparticle and dye molecules is crucial. Thus, in the fabrication of the nanocomposite, the selection of an appropriate material to make a spacer is important. Zhang *et al.* found ~ 90-fold fluorescence enhancement by doping dye molecules into a ZnO nanomatrix.[80] DNA sequences were also applied as the spacer to adjust the distance between dye molecules and the metal core.[81] However, DNA spacers require strict experimental conditions, such as pH and temperature. In this work, we chose to

use a silica layer as the spacer. Several unique properties make silica an excellent spacer material, including well-established surface chemistry, low toxicity, good transparency, and thermal stability. The silica surface can be modified with suitable functional groups, such as thiol, carboxyl, and amine groups, which are very useful for further linking biomolecules (*e.g.*, antibodies, DNA).

The formation of silica layer was obtained using the Stöber method that needs an organic medium. However, under such a condition, AuNPs become unstable, making it difficult to directly coat the silica layer on the AuNP surface. The color of monodispersed citrate ion-protected AuNPs immediately turned from red to dark blue in the organic solvent, indicating the aggregation of AuNPs.

To solve this problem, an amphiphilic nonionic polymer, PVP, was employed as a coupling agent. Our previous work had shown that the PVP can be easily adsorbed on the surface of AuNPs and had no effect on the subsequent formation of the silica layer. It was also reported that the amount of PVP was critical. To achieve successful silica coating on the gold surface, one AuNP should have about 60 PVP molecules per nm^2 of surface area.[79] A deficiency in applying PVP resulted in no or partial silica coating on AuNPs. To ensure the amount of PVP is sufficient, excess PVP was used and the unreacted PVP was removed by centrifugation. Afterwards, a uniform silica layer was formed on the AuNP surface (Figure 14 a – f).

Different thicknesses of silica shell were obtained by varying the reaction time, the amount of TEOS, or a combination of these two factors. The three different sized PVP-stabilized AuNPs were added to the Stöber solution separately as described in Section 2.3. The ratio of EtOH: H_2O: NH_4OH in the Stöber solution affected the results as well. The best ratio of EtOH: H_2O: NH_4OH was found to be 10: 1: 0.5. For the 33.6 ± 4.3 nm AuNPs, the layer thickness of 16.3 ± 3.4 nm and 24.1 ± 3.3 nm

were obtained by adding 20 µL TEOS with 3 h reaction time and 35 µL TEOS with 4.5 h reaction time, respectively (Figure 14a and b). For the 19.7 ± 2.2 nm AuNPs, by adding 30 µL TEOS with 2 h reaction time or 40 µL TEOS with 4 h reaction time, a silica layer of 20.5 ± 3.2 nm or 32.6 ± 5.1 nm were obtained, respectively (Figure 14c and d); and for the 13.7 ± 1.3 nm AuNPs, the silica layer thickness of 18.9 ± 3.4 nm and 25.6 ± 3.3 nm were obtained, respectively (Figure 14e and f). The absorption spectra of silica coated AuNPs had a red shift. This red shift has been attributed to the dielectric environment changes upon the addition of a silica shell. Varying the reaction time below 4 hours would also produce different thicknesses of silica layer. However, when the time was longer than 5 hours, the layer became less homogeneous, loosened and disintegrated.

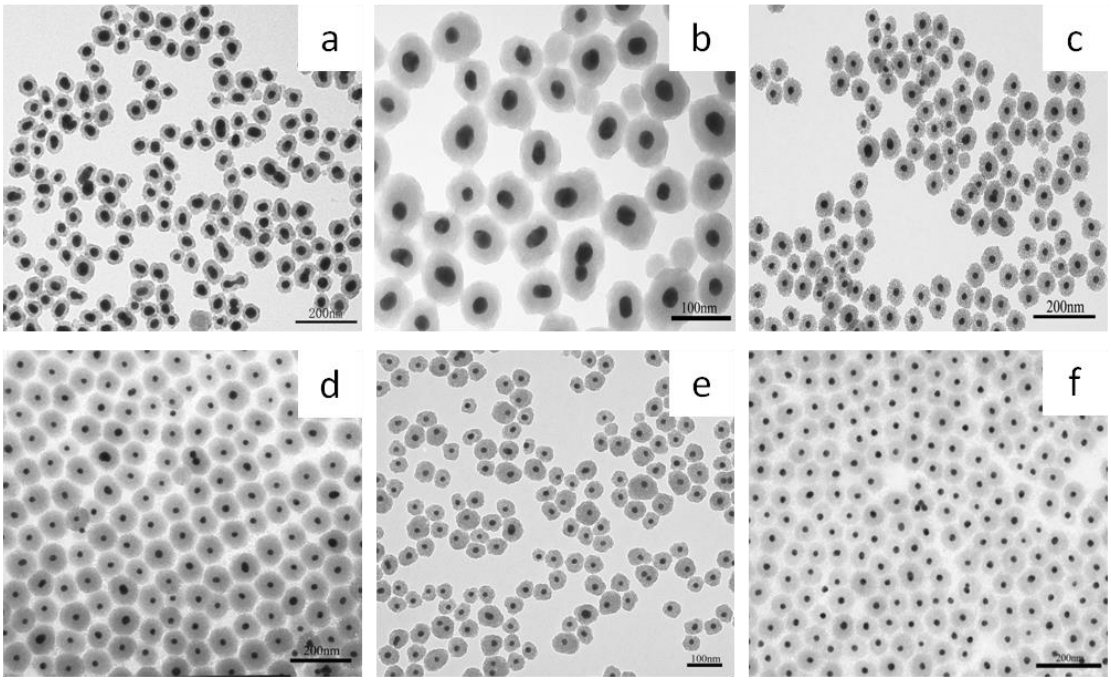

Figure 14. TEM images of silica coated AuNPs. (a – b) 33.6 ± 4.3 nm AuNPs with the silica layer of 16.3 ± 3.4 nm and 24.1 ± 3.3 nm, respectively; (c – d) 19.7 ± 2.2 nm AuNPs with the silica layer of 20.5 ± 3.2nm and 32.6 ± 5.1 nm, respectively; (e – f) 13.7 ± 1.3 nm AuNPs with the silica layer of 18.9 ± 3.4nm and 25.6 ± 3.3nm, respectively.

3.4. Conjugate of TAMRA-SE with PLL.

Covalent binding and electrostatic interaction are the most popular methods to dope dye molecules into a silica matrix. Electrostatic interaction is a relatively weak association force compared to covalent bonds. Its advantage is simplicity. The dye used was positively charged TAMRA-SE that can be directly doped into the silica matrix based on the electrostatic interaction. In order to increase the doping efficiency and reduce the leakage of dye molecules, TAMRA-SE was conjugated with PLL (Figure 15). PLL is a relatively big molecule and commonly used in biological research as a block copolymer with PEG. The amine groups on the PLL can react with the succinimidyl ester on the TAMRA-SE to form a complex of TAMRA-SE-PLL. The complex increased the size of the doped dye and thus reduced the leakage of dye molecules from the nanocomposite. Furthermore, by controlling the ratio of PLL to TAMRA-SE, the distance among dye molecules and the self-quenching of dye molecules could be controlled.

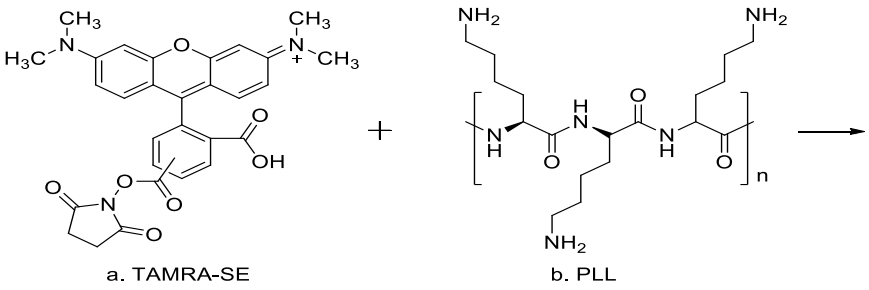

a. TAMRA-SE b. PLL

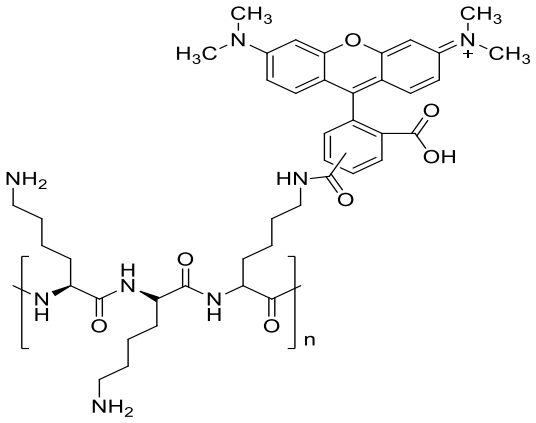

c. Conjugate of TAMRA-SE with PLL.

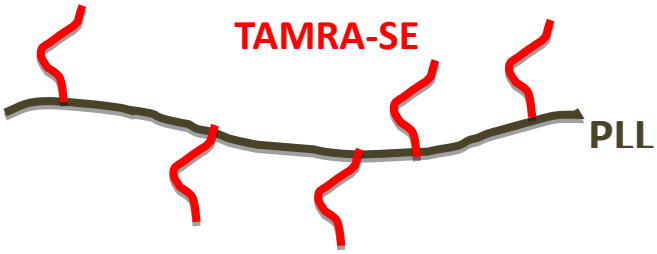

d. schematic diagram of the TAMRA-SE-PLL conjugate.

Figure 15. Conjugation of TAMRA-SE with PLL. a) Molecular structure of TAMRA-SE, b) molecular structure of PLL, c) conjugate of TAMRA-SE-PLL, d) schematic diagram of the TAMRA-SE-PLL conjugate.

The TAMRA-SE-PLL conjugates were then used to form the nanocomposites. The previously obtained core-shell AuNP-silica nanoparticles were placed in the Stöber solution along with the TAMRA-SE-PLL conjugates. When the second layer of silica was formed, the dye conjugates were simultaneously doped into this layer. The nanocomposites were eventually formed. Although the two silica layers were formed sequentially, they appeared homogeneous and the junction of the two layers was difficult to identify (Figure 16).

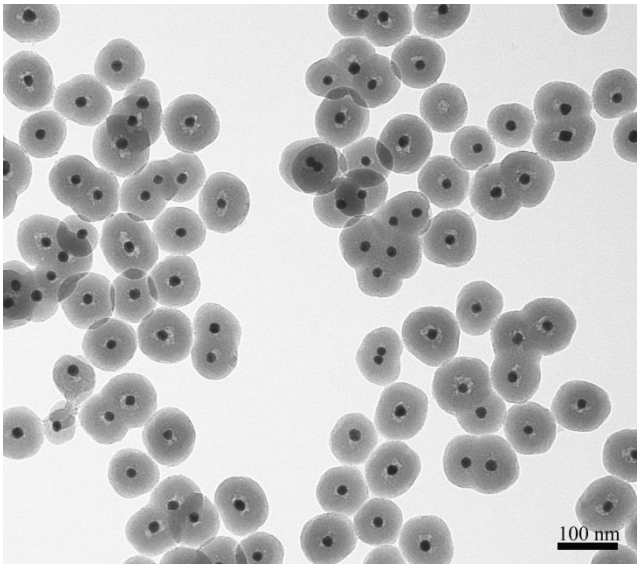

Figure 16. Two sequentially formed silica shells on 13.7 nm-AuNPs.

3.5. pH Effect on the Fluorescence Intensity of TAMRA-SE-PLL Conjugates.

The capability of the fluorescence enhancement of the developed

nanocomposites should be investigated with a number of reasonable control experiments. To accurately measure the amount of dye molecules doped into the nanoparticles, the doped dye-PLL conjugates were released. The removal of AuNPs was accomplished by eroding the silica shell with NaOH and separating the AuNPs by centrifugation. The addition of NaOH affected the solution pH which may affect the fluorescence intensity of TAMRA-SE-PLL as well. Therefore, it was necessary to study the pH effect on TAMRA-SE-PLL.

The measurement of fluorescence intensities of the same amount of TAMRA-SE-PLL in different pH solutions is shown in Figure 17. The pH values ranged from 4 to 11, which covered the whole spectrum pH of our experiments. The results showed that the fluorescence intensity of TAMRA-SE-PLL was constant in the range of pH 4 –11.

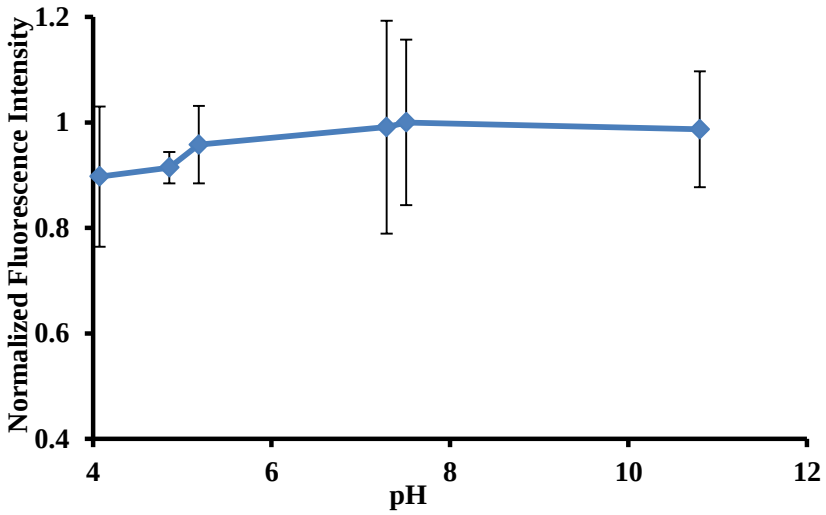

Figure 17. pH effect on the fluorescence intensity of TAMRA-SE-PLL.

3.6. TAMRA-SE-PLL Adsorption Effect.

Pure AuNPs are good quenchers for many dye molecules due to the resonant energy transfer from the dye molecules to the AuNPs. To confirm this phenomenon, the freshly prepared AuNPs were added into the TAMRA-SE-PLL conjugate solution.

Afterwards, the fluorescence intensity of mixture was measured as shown in Figure 18. Without the AuNPs the fluorescence intensity of the TAMRA-SE-PLL was measured and normalized as 1 (Figure 18, curve a). Comparing curve a to curves b, c and d, where different sized AuNPs were used, it is obvious that the fluorescence of TAMRA-SE-PLL was quenched in the presence of AuNPs. We have calculated the percentage of the quenched fluorescence intensity with the different sized gold nanoparticles. The results showed that in the presence of 13 nm, 20 nm, and 34 nm AuNPs, 95.4% ± 1.7%, 98.6% ± 0.2%, and 98.2% ± 0.2% of fluorescence intensities were quenched. The difference between 13 nm and 20 nm is 3.2%, and the difference between the 13 nm and 34 nm is 2.8%. The differences may be due to the differences in their effective surface areas. In our experiments, the TAMRA were not used as free dye molecules but were conjugated to Poly-L-Lysine, resulting in a larger size. Therefore, although the 13 nm AuNPs has a larger surface area than those of 20 nm and 34 nm AuNPs, the effective surface area that can contact with TAMRA-SE-PLL may be that large, leading to a relative low quenching efficiency.

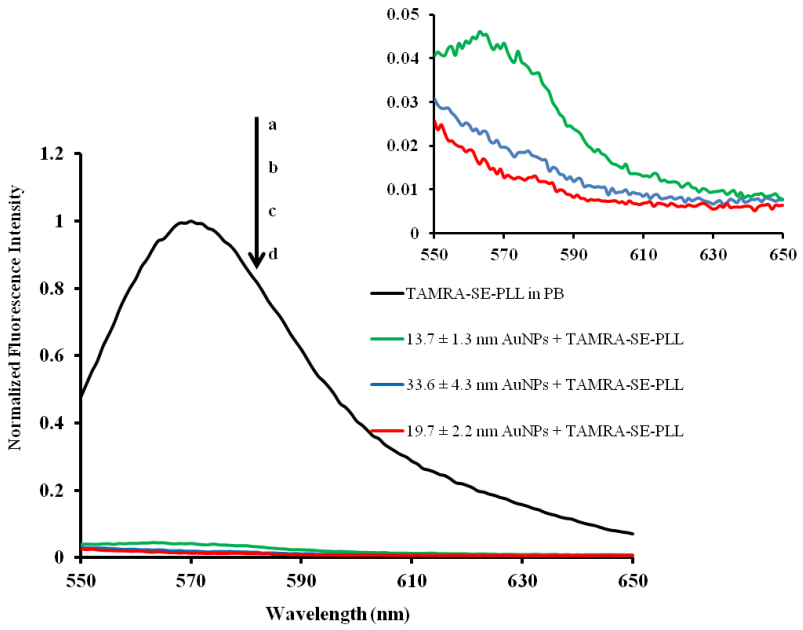

Figure 18. Fluorescence intensity of TAMRA-SE-PLL with and without AuNPs. Curve a). 1 µL of 0.04 mM TAMRA-SE-PLL was added into 3.0 mL PB buffer solution (pH 7.4). Curve b – d). 1 µL of 0.04 mM TAMRA-SE-PLL and 0.3 mL of different sized freshly prepared AuNPs were added into 2.7 mL PB buffer solution. Excitation: 540 nm; Emission range: 550 – 650 nm; slit: 5 nm. Inset: fluorescence spectra of TAMRA-SE-PLL with different sizes of AuNPs.

In the process of silica shell erosion, the dye molecules were dispersed in the solution instead of remaining entrapped in the silica matrix. Although the AuNPs were removed by centrifugation, the released dye molecules might be physically adsorbed on the AuNPs and thus be removed along with the AuNPs. To investigate this adsorption possibility, an aliquot of 0.5 mL of 0.4 M NaOH was added into the silica-coated AuNP solutions with free TAMRA-SE-PLL. After overnight stirring and the centrifugation, the fluorescence intensity of supernatant was detected. For the control experiment, TAMRA-SE-PLL was added into water and the fluorescence intensity was measured. The results are shown in Figure 19.

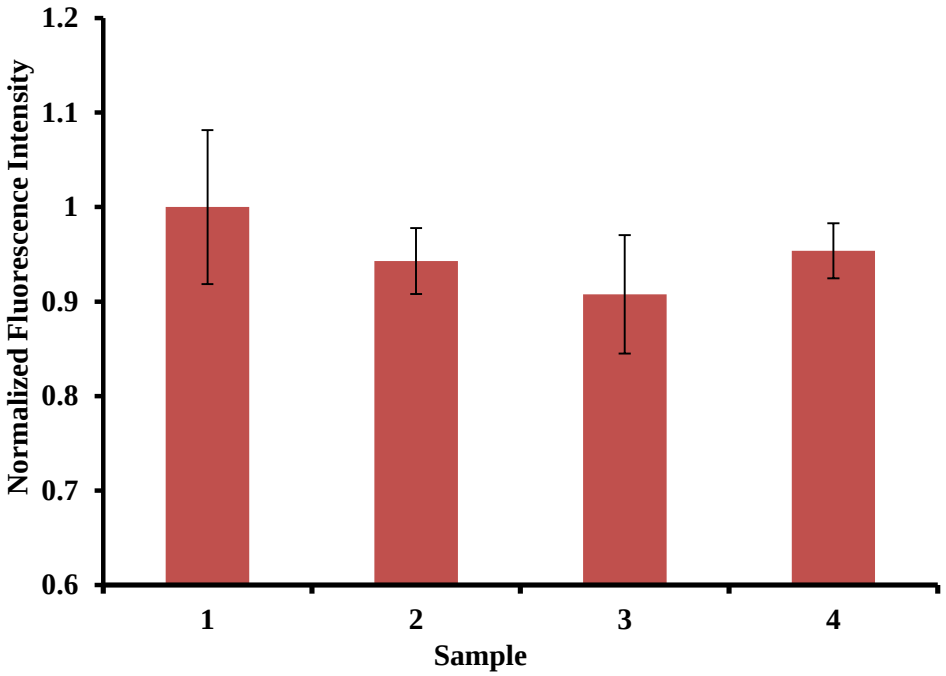

Figure 19. Fluorescence intensity of released TAMRA-SE-PLL from the silica matrix. Sample 1: 1 µL of 0.04 mM TAMRA-SE-PLL was added in 3.0 mL PB buffer; sample 2 – 4 are silica coated on different sized AuNP core cores. The reaction condition: 1 µL of 0.04 mM TAMRA-SE-PLL, 2.5 mL of silica coated AuNPs, and 0.5 mL of 0.4 M NaOH were mixed together and stirred for 24 h in dark. The fluorescence intensity of supernatant was measured after centrifugation to remove the AuNPs. Excitation: 540 nm; Emission range: 550 – 650 nm; slit: 5 nm.

The student *t*-test showed that the fluorescence intensity of four samples in Figure 19 had no significant difference. This is probably due to the removal of negative charges on the surface of AuNPs. AuNPs were monodispersed when they were first synthesized due to the presence of citrate ion. However, if the positively charged TAMRA-SE-PLL is added, it will directly adsorb on the AuNPs. As a result, the fluorescence of TAMRA-SE-PLL is quenched. When the AuNPs went through silica coating, dye doping, and silica erosion, the final AuNPs lost the protection from citrate ions, which made AuNPs aggregate easily and thus became difficult to adsorb dye molecules (Figure 20).

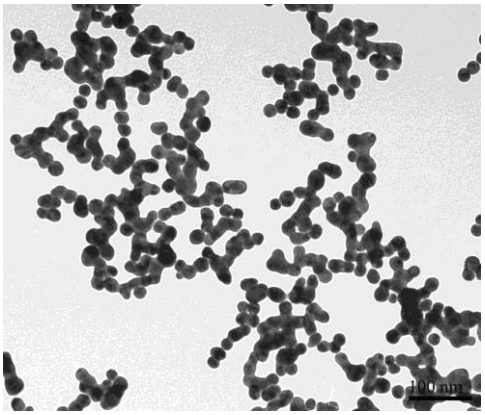

Figure 20. TEM image of the aggregated AuNPs after the silica layer erosion.

3.7. MEF in the Nanocomposite.

The fluorescence enhancement was first investigated using the nanocomposites with a 13.7 ± 1.3 nm AuNP core. The effect of the distance between the dye molecules and the metal cores on the fluorescence enhancement was studied. This distance was defined as the distance from the junction between two silica layers to the edge of AuNPs, that is, the thickness of the spacer.

The enhancement was characterized using fluorescence enhancement factor, F ($F=I_{nanocomposite}/I_{released}$TAMRA, $I_{nanocomposite}$ is the fluorescence intensity of dye-doped nanocomposites; $I_{released}$ TAMRA is the fluorescence intensity of released TAMRA-SE-PLL without the metal core). In our previous study it was observed that the fluorescence quantum yield of the doped dye molecules would be affected by the surroundings. Therefore, to avoid the significant quantum yield changes, in this study the experimental conditions were chosen to minimize the changes of fluorescence quantum yield of dye molecules. Figure 21 shows that when the 17.6 nm spacer was used, the fluorescence was enhanced by 3.2 times. When the size of the spacer increased to 19.2 nm, the fluorescence intensity was increased by 4.8. When the spacer size was further increased to 36.6 nm, the fluorescence intensity was increased by 9.2 times. At this point, it is difficult to continue to increase the spacer size due to

the limitation of the experimental conditions. The above results showed that the designed nanocomposites can obviously enhance the fluorescence intensity of the encapsulated dye molecules.

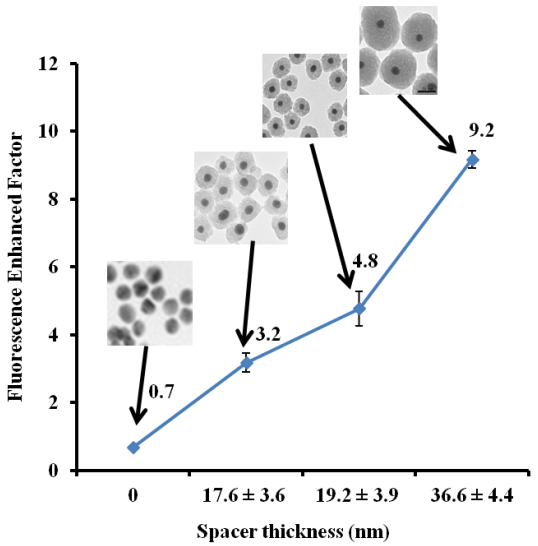

Figure 21. Distance dependent fluorescence enhancement of the TAMRA-SE-PLL using the 13.7 ± 1.3 nm AuNP core.

To further confirm this result, the two nanocomposites containing larger-sized AuNP cores were employed. The first one was the 19.7 nm-AuNP core with three different sized spacers. Compared to the results from the 13.7 ± 1.3 nm AuNP core in Figure 21, when similar spacer sizes were applied, all three enhancement factors were smaller (Table 1). This phenomenon was further confirmed when the largest size of 33.6 nm-AuNP was used as the core. For instance, with a similar spacer thickness of 36 nm, the fluorescence was only enhanced by 3.2 times; this was 3 times less than the enhancement obtained from the smaller sized AuNP of 13.7 nm.

Table 1. Distance dependent fluorescence enhancement

AuNP core size (nm)		13.7 ± 1.3		
Spacer thickness (nm)	0	17.6 ± 3.6	19.2 ± 3.9	36.6 ± 4.4
Fluorescence enhancement factor	0.7	3.2	4.8	9.2
AuNP core size (nm)		19.7 ± 2.2		
Spacer thickness (nm)	0	14.3 ± 3.1	22.4 ± 4.1	28.5 ± 5.0
Fluorescence enhancement factor	0.4	1.5	3.3	6.0
AuNP core size (nm)		33.6 ± 7.6		
Spacer thickness (nm)	0	17.0 ± 1.4	24.1 ± 3.3	35.7 ± 7.6
Fluorescence enhancement factor	0.3	1.9	2.4	3.2

The above results showed that the distance between TAMRA-SE-PLL dye molecules and the AuNP could significantly affect the extent of the fluorescence enhancement at the nanoscale. Within the 36 nm range, the fluorescence enhancement increased as the distance became larger; in contrast to the fluorescence quenching when no silica spacer was employed. The largest enhancement factor was found to be 9.2 at a fluorophore-metal distance of 36.6 nm using the smallest size of AuNP core (13.7 ± 1.3 nm). Therefore, the fluorescence intensity depended not only on the metal core size but also on the distance between the metal core and the dye molecules. The three spacer sizes are all larger than the fluorescence energy transfer effect distance of 10 nm. The detailed mechanism is being studied. It is expected that the designed metal-dye nanocomposites may provide a useful model for better understanding of the geometric and dimensional effects of metallic nanostructures on the fluorescent molecular properties.

4. Conclusions

In conclusion, the dye-doped, metal-silica core-shell fluorescent nanocomposites were synthesized to study the MEF phenomenon. The nanocomposite is a promising model to study the interactions between the metal core and the dye molecules. The formation of the silica shell adjusted the spacer thickness to the

optimal distance where the maximum fluorescence enhancement can occur. A spacer thickness ranging from 14.3 nm to 36.6 nm was applied in this work and the fluorescence enhancement was observed in all developed nanocomposites. The fluorescence quenching effect was obvious when no spacer was used, indicating the importance of the distance between the dye molecules and the metal cores. The largest fluorescence enhancement of ~9-fold was observed by applying 13.7 ± 1.3 nm AuNP as the metal core with a 36.6 ± 4.4 nm silica spacer.

CHAPTER III

HIGHLY SENSITIVE PROTEIN ASSAY USING GOLD NANOPARTICLES-DECORATED SILICA NANORODS

1. Introduction

Sensitive detection of proteins is of tremendous interest for a broad range of applications such as clinical diagnosis, food safety, and environmental analysis.[82-86] A variety strategies and techniques have been developed for the detection of proteins, including enzyme-linked immunosorbent assay (ELISA), western blot, agarose and polyacrylamide gel electrophoresis, and immunosensors in connection with various transducers.[87-95] The sensitivities of the assays were further enhanced by the use of nanomaterials (nanoparticles, nanowires and nanotubes)[96-99] and novel signal amplification approaches.[100-103] However, most of the nanomaterial-based signal amplification methods generally involved in a time-consuming detection process or using advanced laboratory equipment. Lateral flow immunoassay (LFI), also called immunochromatographic assay, have been studied extensively for different applications, such as pregnancy tests, detections of cancer biomarkers, infectious agents, biowarfare agents and toxic compounds.[104-105] In a typical LFI, the antibody-modified marco-/nano- particles move along the strip with the analytes driven by capillary force, and are eventually captured by the pre-immobilized antibodies in the test zone. The captured marco-/nano-particles, which are proportional to the target concentrations, can be determined by observing the color changes of test band or recording the fluorescence, electrical or magnetic signals with appropriate transducers.[106-107] gold nanoparticles (AuNPs),[108-110] carbon nanoparticles,[111] quantum dots[112-114] and Fe_3O_4 nanoparticles,[115] *etc*., have been used as labels for the development of LFIs. Although the fluorescent-, magnetic- and

electrical-LFIs offered high sensitivity, the requirement of the instrumentation and skilled personnel limit its point-of-care or in-field applications.

Among the aforementioned colored particles for visual detection with LFI, AuNPs are the most applicable materials due to its unique optical properties (plasma absorption), remarkable chemical stability, and easy surface modification. The AuNP-based LFI have been applied for the qualitative, semi-quantitative/quantitative detection of proteins,[116] metal ions,[117] and natural toxins.[118] However, the detection of extremely low concentration of proteins is limited by its low sensitivity. Therefore, it is highly desirable to develop highly sensitive LFI for visual detection of proteins.

Recently, great efforts have been made to improve the sensitivity of the AuNP-based LFIs by using dual-labeling method. Choi *et al.* reported a dual AuNP conjugate-based lateral flow assay method for the analysis of troponin I.[119] The first AuNP conjugate was allowed to be immobilized with an antibody against Troponin I for the purpose of the sandwich assay contained in atypical LFI system. The second AuNP conjugate was designed to bind only with the first AuNP conjugate with a higher size. The detection sensitivity increased about a 100-fold compared to the conventional LFI. Chen *et al.* reported a sensitivity enhanced LFI based on the same concept using different-sized AuNPs for the visual detection of bisphenol A.[120] The LOD of the LFI was lowered 10 times compared the traditional AuNP-based assay. He *et al.* reported an ultrasensitive nucleic acid biosensor (NAB) based on horseradish peroxidase (HRP) – gold nanoparticle (AuNP) dual labels and lateral flow strip biosensor (LFSB).[121] Deposition of insoluble enzymatic catalytic product (red colored chromogen) on the captured AuNPs at the test zone of LFSB offered a dramatic visual enhancement. Combining enzyme catalytic amplification with unique optical properties of AuNPs, the NAB was capable of detecting of 0.01 pM target DNA

without instrumentation. Tang *et al.* found that on the use of magnetic AuNP labels lowered the detection limit 3-folds for the detection of aflatoxin B_2 compared to a conventional immunodipstick test using AuNPs as colored reagent.[122]

In this work, we report an ultrasensitive protein assay using a gold nanoparticle-decorated silica nanorod (AuNPs-SiNRs) label and lateral flow strip biosensor. Silica-based nanomaterials (nanoparticles, nanowire and nanorods) have attracted considerable interests in biomedical research owing to their unique properties, such as inertness, high payload capacity, biocompatibility, and great surface-modification.[123] The silica-based nanomaterials have been applied for the development of high sensitive biosensors and bioassays.[124-127] Inspired by the signal amplification methods, silica nanorods were chosen as a matrix to make a AuNPs-SiNRs hybrid. A large number of AuNPs on one single SiNR provided visualized dark purple color that was much darker than the pure AuNPs solution. The nanohybrid was used as a colored reagent instead of AuNP in LFI. Rabbit IgG was used as a model target to demonstrate the proof-of-concept. Under optimal conditions, a detection limit of 0.01 ng mL^{-1} (10 pg mL^{-1}) was obtained, which is almost 50-fold lower than that of AuNPs-based LFI.[128] The promising properties of the AuNPs-SiNRs-based LFI are reported in the following sections.

2. Experimental Section

2.1. Apparatus.

A Hitachi SU8010 field scanning electron microscope (SEM) (Japan) was used to take images of the developed nanocomposites. The elemental analysis was obtained by performing energy-dispersive X-ray spectroscopic (EDS) measurements (Oxford X-Max, MA, USA), which is attached to the Hitachi SU8010 field emission SEM. A Shimadzu UV-vis spectroscopy (MD, USA) was used to obtain the

absorption spectra of the nanomaterials. Airjet AJQ 3000 dispenser, Biojet BJQ 3000 dispenser, Clamshell Laminator and the Guillotine cutting module CM 4000 purchased from Biodot LTD (CA, USA) were used to prepare lateral flow strips. A portable strip reader DT1030 (Shanghai Goldbio Tech. Co., Shanghai, China) was used for signal recording.

2.2. Materials.

Tetraethylorthosilicate (TEOS, 98%) was purchased from Acros Organics (NJ, USA).Sodium citrate (Na_3Ct), gold (III) chloride trihydrate ($HAuCl_4 \cdot 3H_2O$, 99.9+%), hydroxylamine hydrochloride (98%, ACS grade), sodium borohydride ($NaBH_4$, > 98%), $Na_3PO_4 \bullet 12H_2O$, sucrose, Tween 20, Triton X-100, phosphate buffer saline (PBS, pH 7.4, 0.01 M), phosphate buffer saline with 0.05% Tween 20 (PBST), and bovine serum albumin (BSA) were purchased from Sigma Aldrich Inc (St.Louis, MO, USA). Ammonium hydroxide (NH_4OH, 28.0% – 30.0%), potassium carbonate ($K_2CO_3 \cdot 1.5\ H_2O$, ACS grade) and ethanol (95%) were obtained from Fisher Scientific Co (Pittsburgh, PA, USA). Polyvinylpyrrolidone molecule (PVP, average molecular weight M_n = 40,000) and 1-pentanol (99+%, ACS grade) were purchased from Alfa Aesar (Ward Hill, MA, USA). Rabbit IgG, goat anti-rabbit IgG (Ab_1), mouse anti-goat IgG (Ab_2) were obtained from Thermo Scientific (Rockford, IL, USA). Glass fibers (GFCP000800), cellulose fiber sample pads (CFSP001700), laminated cards (HF000MC100) and nitrocellulose membranes (HFB18004) were provided by Millipore (Billerica, MA, USA). All chemicals were analytical reagent grade unless specified. All buffer solutions were prepared using ultrapure water (18 MΩ·cm) from a Millipore Milli-Q water purification system.

2.3. Preparation of Silica Nanorods (SiNRs).

A one-step synthetic method was used to prepare SiNRs. In a typical

synthetic procedure, a total of 3.00 g PVP was added to 30.00 mL of 1-pentanol. The mixture was sonicated for 30 min to obtain a well-mixed PVP/pentanol solution. Then, 3.00 mL of 95% ethanol, 0.84 mL of H_2O, and 0.20 mL of 0.17 M Na_3Ct were added into the PVP/pentanol mixture followed by hand-shaking for a few seconds. Following the addition of 0.30 mL of TEOS and 0.50 mL of NH_4OH the reaction was allowed to proceed overnight at room temperature. The SiNRs were collected by centrifuging at 11,000 rpm for 30 min and removing the supernatant. The collected SiNRs were washed three times with ethanol and dried in the oven at 100 °C.

2.4. Preparation of Gold Seeds.

Typically, 4.00 mL of 1% $HAuCl_4$ solutions was added into 100.00 mL H_2O in an ice bath, followed the addition of 0.50 mL of 0.20 M K_2CO_3 to reduce Au(III) to Au(I). Stir for 10 min until the solution changed its color from yellow to light yellow or colorless. Then, a total amount of 1.00 mL of freshly prepared $NaBH_4$ (0.50 mg/mL) was slowly added. The formation of reddish solution indicated the successful synthesis of gold seeds.

2.5. Preparation of Gold Nanoparticles-Decorated Silica Nanorods (AuNPs-SiNRs).

The AuNPs-SiNRs were prepared according to the reported methods with slight modifications.[44] A aliquot of 1.00 mL of 10.00 mg/mL SiNW solution was added into 40.00 mL gold seeds solution and the mixture was stirred vigorously for 20 min. Surplus gold seeds were removed by centrifugation at a speed of 6,500 rpm for 15 min. The obtained reddish precipitate was gold seed-decorated SiNRs and was re-dispersed in 10.00 mL water. In the gold shell growth process, 4.00 mL of 1% $HAuCl_4$ solution and 0.025 g of K_2CO_3 were added in 90.00 mL water. The mixture was under stirring until it turned to light yellow or colorless. Then, 10.00 mL of gold seeds-decorated SiNWs solution, 1.00 mL of 0.5 M hydroxylamine hydrochloride,

and 1.00 g PVP were sequentially added into the growth solution. After overnight reaction, the solution was centrifuged at a speed of 6,500 rpm for 15 min and washed 3 times by water. The size of AuNPs that decorated on the surface of SiNWs can be adjusted by adding different amounts of 1% $HAuCl_4$ (0, 2, 4, or 6 mL).

2.6. Preparation of AuNP-SiNRs-Ab_1 Conjugates.

Initially, 0.01 mg of Ab_1 was mixed with 1.00 mL of AuNPs-SiNRs (pH 9.0) followed by gentle shaking for 1 h at room temperature. Then 0.10 mL of 10.0 wt% BSA was added with a final concentration of 1.00 wt% and incubated for 30 min. The mixture was further washed with PBS (1% BSA) and centrifuged at 6,000 rpm for 5 min to remove washing liquid. Finally, the as-prepared AuNPs-SiNRs-Ab_1 conjugates were collected and suspended in 1.00 mL of eluent buffer containing 20.00 mM Na_3PO_4•$12H_2O$, 0.25% Tween 20, 10% sucrose and 5% BSA.

2.7. Preparation of AuNPs-Ab_1 Conjugates.

AuNPs with a diameter of 15 ± 3.5 nm were prepared on the basis of a literature procedure.[129] Then, 0.01 mg of Ab_1 was added into 1.0 mL of 5-fold concentrated AuNPs (pH 9.0). The mixture was gently incubated for 1 h, and blocked by 0.1 mL of 10 wt% BSA for 30 min. The obtained solution was centrifuged at 12,000 rpm for 18 min, and the nanoparticles were washed with PBS (1% BSA) three times. The resulting ruby sediments were dispensed in 1.0 mL of buffer containing 20 mM Na_3PO_4•$12H_2O$, 0.25% Tween 20, 10% sucrose and 5% BSA.

2.8. Preparation of the Lateral-Flow Strip Biosensor (LFSB).

The LFSB consisted of the following components: a sample-application pad, a conjugate pad, a nitrocellulose membrane, and an absorption pad. Both the sample-application pad and the absorption pad were made from cellulose fiber. The sample-application pad (17 mm × 30 cm) was soaked in a buffer (pH 8.0) containing

0.25% Triton X-100, 0.05 M Tris-HCl, and 0.15mM NaCl. Then, the sample pad was dried at 37 ^{o}C in the oven and stored in desiccators at room temperature. Ab_1, with a concentration of 1.20 mg mL^{-1}, and Ab_2 (0.85 mg mL^{-1}) were dispensed at different locations of the nitrocellulose membrane (25 mm × 30 mm)to form the test line and the control line by using a Biojet BJQ 3000 dispenser. The nitrocellulose membrane was then dried in the oven at 37 ^{o}C for 1 h. Finally, all the parts were assembled on a plastic, adhesive backing layer (typically an inert plastic, *e.g.*, polyester) using the Clamshell Laminator. Each part overlapped 2 mm to ensure that the solution migrated through the biosensor during the assay. The LFSB with a 3-mm width was cut with the Guillotin cutting-module CM 4000.The AuNPs-SiNR-Ab_1 conjugates were dropped on the conjugate pad using a pipet before each test.

2.9. Detection Procedure.

The assay was performed by dipping the LFSB in a 1.50-mL microcentrifuge tube containing the desired concentration of rabbit IgG in 0.10 mL of running buffer (PBST with 1% BSA). The test and control zones could be evaluated visually within 20 min. The intensities of the test line and the control line were measured using a strip reader, and the results were further analyzed using the Gold Bio strip-reader software.

3. Results and Discussion

3.1.AuNPs-Decorated SiNRs as Colored Reagents in the LFSB.

Various marcro-/nano-particles, including AuNPs, dye-doped polystyrene beads, and carbon nanospheres, have been used as labels for a lateral-flow assay. The analyte concentration is determined by observing the color change (qualitative/semi-quantitative) of the test zone or by recording the intensities (quantitative) of the test band. The sensitivity of the assay is affected by the number

of captured particles per antibody-antigen binding event. Although AuNPs were most commonly used as colored reagents, the sensitivity of AuNP-based LFSBs was not high enough to detect trace amounts of analytes (such as protein biomarkers). The composite nanomaterial, formed by numerous AuNPs evenly coated on a single substrate, would be an ideal colored reagent to enhance the LFSB sensitivity. Several materials, including carbon nanotubes and polymers,[130-133] were used as substrates to prepare the composite nanomaterials. However, most of the composite nanomaterials involved complicated or strict synthetic procedures. Silica-based nanomaterials (nanoparticles, nanorods, and nanowires) have shown great promise in various fields due to the nanomaterials' unique physical and chemical stability as well as their well-established surface modification.[134-135] In the current study, silica nanowires (SiNWs) and nanorods were used as substrates to coat AuNPs due to the larger surface area per rod or wire compared to that per nanoparticle. The synthesized AuNP-SiNWs and AuNP-SiNRs were used as labels for the lateral-flow assays. The mobility of AuNP-SiNWs was much slower than that of AuNP-SiNRs on the nitrocellulose membrane due to the large size of the SiNWs (The length of SiNWs is up to tens of micrometers, results not shown here). Therefore, we chose AuNP-SiNRs, which have a dark purple color and better mobility, as the colored reagents.

3.2. Preparation and Characteristics of AuNP-Decorated SiNRs (AuNP-SiNRs).

A two-step deposition process involving gold-seed deposition and seed growth was used to prepare the AuNP-SiNRs. SiNRs with a length varying from 3.4 – 7.0μm (Figure 22A) were used as the substrate to load numerous AuNPs. Gold seeds were deposited on the SiNR surface by simply mixing AuNP and SiNR solutions for 20 min. Figure 22B presents the typical SEM image of the gold-seed-loaded SiNRs. One can see that the gold seeds with a diameter of 9.7 ± 1.6 nm are monodispersed on

the SiNR surface. The gold-seed-decorated SiNRs were then added to a gold growth solution to form a uniform AuNP layer. Figure 22C shows the SEM image of AuNP-decorated SiNRs after the AuNP growth process. A layer of AuNPs was coated on the SiNR surface, and the density of AuNPs was much higher than the gold-seed-decorated SiNRs. To further identify the formation of the AuNP layer on the SiNR surface, element analysis was performed by the EDS technique. A strong peak for the gold signal was observed in the EDS spectra of AuNP-SiNRs, indicating that AuNPs were successfully loaded on the SiNRs (Figure 22D). Figure 22E presents the UV-vis absorption of the AuNP-SiNR suspension, gold-seed solution, and SiNR suspension. No UV-vis absorption (Figure 22E, a) was observed for the SiNR solution while a typical absorption peak around 514 nm of gold-seed solution was observed (Figure 22E, b). However, AuNP-SiNRs showed an obvious red-shifted, broader peak with a strong absorption in the near-infrared region compared to that of the gold seeds (Figure 22E, c).

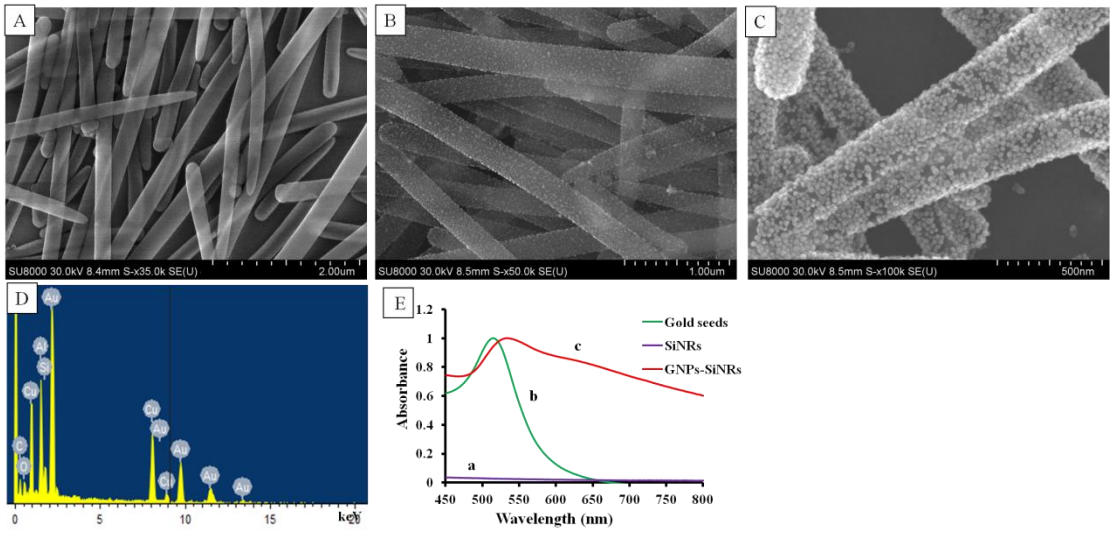

Figure 22. SEM images of (A) SiNRs; (B) gold seed-decorated SiNRs; (C) the formation of GNPs layer on the surface of SiNRs; (D) a representative EDS spectra of AuNPs-SiNRs; (E) UV-vis spectra of SiNRs (a), gold seeds (b), and AuNPs-SiNRs (c).

We studied the effect of the $HAuCl_4$ concentration in the growth solution on

the AuNP size and coverage on the SiNR surface (Figure 23). Without the addition of a gold precursor ($HAuCl_4$) in the growth solution, the AuNP size (9.7 ± 1.6 nm) did not change, and AuNPs were evenly positioned on the SiNR surface (Figure 23A). By adding 2 mL of 1% $HAuCl_4$, gold seeds grew to bigger AuNPs with a size of 16.7 ± 2.4 nm (Figure 23B). In the case of 4 and 6 mL of 1% $HAuCl_4$ addition to the growth solution, SiNR surface was covered by a layer of AuNPs (Figure 23C – D). However, a large number of free AuNPs were synthesized when 6 mL of 1% $HAuCl_4$ solution was added. Therefore, in the following lateral-flow immunoassay application, AuNP-SiNRs synthesized from the addition of 4 mL of 1% $HAuCl_4$ in the growth solution were used as the color reagent.

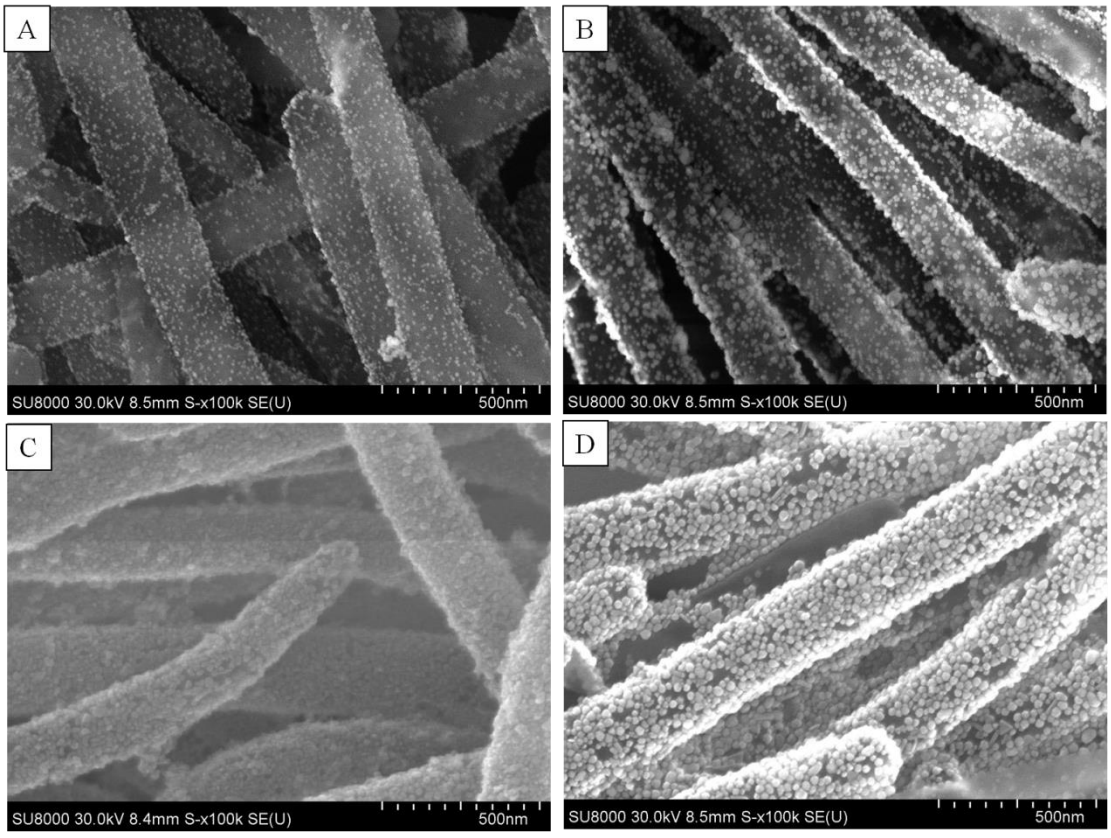

Figure 23. SEM images of AuNPs-SiNRs by adding (A) 0, (B) 2, (C) 4, (D) 6 mL of 1% $HAuCl_4$ in the gold growth solution.

3.3. AuNP-SiNR-Label Based LFSB.

The AuNP-SiNRs were, thus, used as labels to fabricate the LFSB. Rabbit

IgG was used as model target to demonstrate the proof-of-concept. Scheme 3 illustrates the LFSB's configuration and measuring principle. The LFSB consisted of a sample pad, a conjugate pad, an absorption pad, and a nitrocellulose membrane (test line and control line, Scheme 3A). All the components were assembled on a common-adhesive backing layer. Goat anti-rabbit IgG Ab_1 was conjugated with AuNP-SiNRs, and the Ab_1-AuNP-SiNR conjugates were dispensed on the conjugate pad. Goat anti-rabbit IgG Ab_1 was also used as the capture antibody and was dispensed on the test zone of the nitrocellulose membrane. Mouse anti-goat IgG Ab_2 was used as the secondary antibody and was immobilized on the control zone of the nitrocellulose membrane, which was 2 mm behind the test zone (Scheme 3B). During the assay, the LFSB was dipped into a test tube, and the sample solution moved up by capillary force. The Ab_1-AuNP-SiNRs conjugates were rehydrated and released from the conjugate pad. The binding between Ab_1 in Ab_1-AuNP-SiNR conjugates and rabbit IgG (target) occurred, and the formed complexes (IgG-Ab_1-AuNPs-SiNRs) continued to migrate along the membrane. When reaching the test zone, the complexes were captured by the antibody on the test zone *via* the second immunoreaction, resulting in the accumulation of AuNP-SiNRs on the test zone. A dark-purple band was observed, and the color intensity of the test band was directly proportional to the amount of analyte (IgG) in the sample solution. The solution continued to flow until it passed through the control zone where the excess Ab_1-AuNP-SiNRs conjugates were captured by the secondary antibody (anti-goat IgG Ab_2) to produce a second dark-purple band (Scheme 3C, right). In the absence of the target, only the band on the control zone was observed, and no band was observed in the test zone. In this case, the band in the control zone (control line) showed that the LFSB was working properly (Scheme 3C, left). Quantitative analysis was achieved by

reading the test-line intensities with a portable strip reader. The more analytes presented in the sample, the more conjugates would be captured on the test zone, leading to the increased signal.

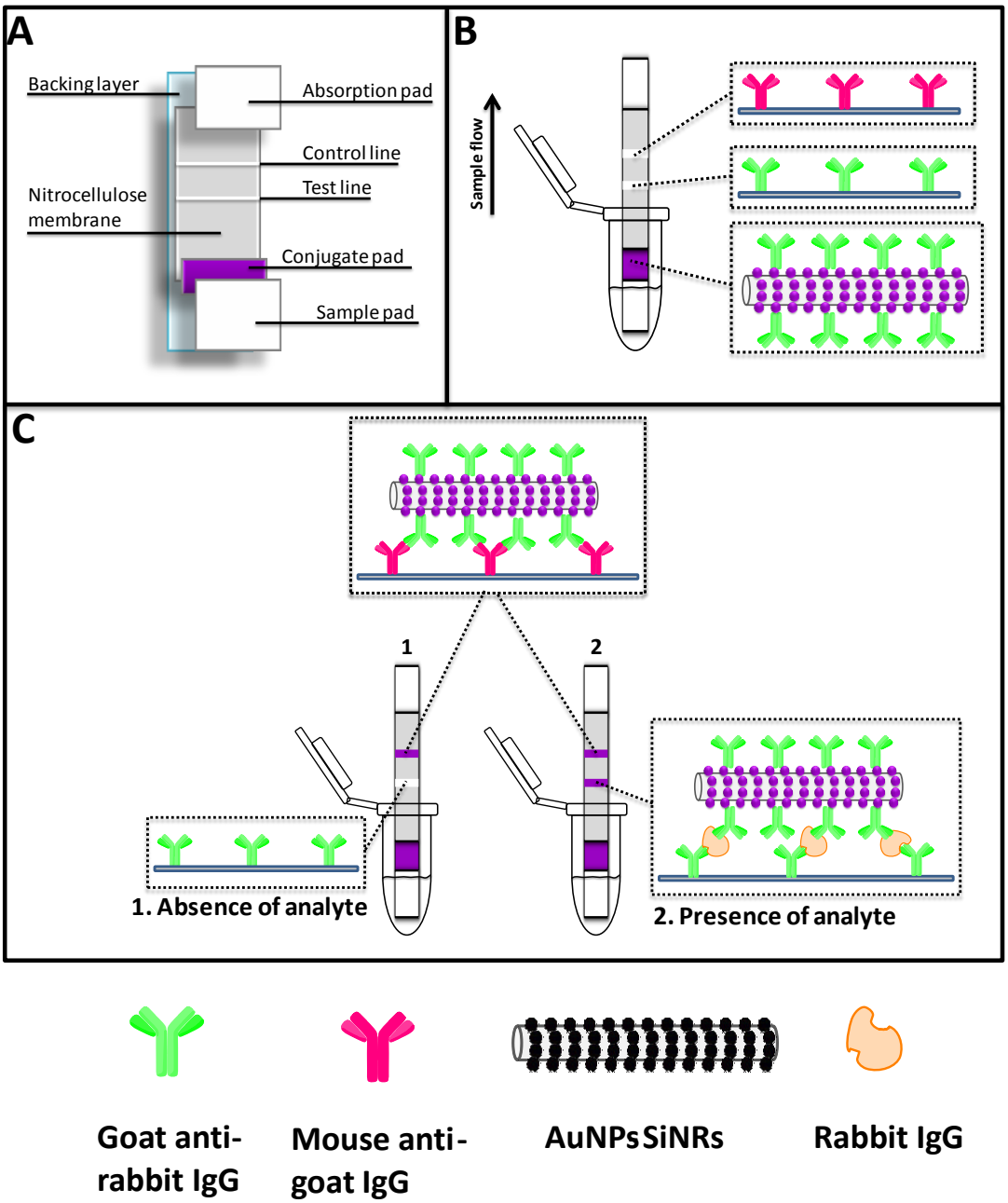

Scheme 3. (A) Schematic representation of the configuration of the lateral flow strip biosensor; (B) Reagents on the lateral flow strip biosensor; (C) Measurement principle of the lateral flow strip biosensor in the absence and presence of analyte (Rabbit IgG).

To confirm the signal amplification of the AuNP-SiNRs, the responses of the

sample solutions at three concentration levels (0, 1.0, and 5.0 ng mL^{-1} IgG) on the AuNP-SiNR-based LFSB were compared with the AuNP-based LFSB. Figure 24 presents the photo images of the LFSBs after the completed assays. When rabbit IgG was absent in the sample solutions, neither of the two LFSBs showed a response on the test zones (Figure 24A). No test line could be observed from the AuNP-based LFSB in the presence of 1.0 ng mL^{-1} of rabbit IgG (Figure 24B, left) while there was a visible test line on the AuNP-SiNR-based LFSB (Figure 24B, right). As shown in Figure 24C, the intensity of the test line on the AuNP-SiNR-based LFSB in the presence of 5.0 ng mL^{-1} rabbit IgG was significantly higher than that of the AuNP-based LFSB which exhibited a very weak response. Such dramatic signal enhancement on the AuNP-SiNR-based LFSB is mostly due to the large surface area of the SiNRs where numerous AuNPs were loaded. The number of the captured AuNPs per antibody-antigen binding on the GNP-SiNR-based LFSB would be much higher than that of the AuNP-based LFSB. In addition, the antibody density on the Ab_1-AuNP-SiNR conjugates would be higher than that of the Ab_1-AuNP conjugates. The immunoreaction efficiency on the AuNP-SiNR-based LFSB was, thus, higher than that for the AuNP-based LFSB with a short assay time.

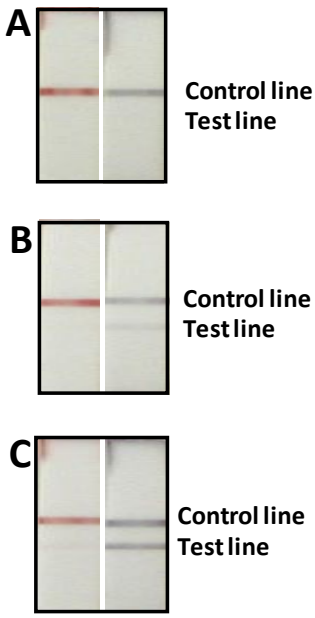

Figure 24. Photo images of the AuNPs-based LFSBs (left) and the AuNPs-SiNRs-based LFSBs (right) in the presence of different concentrations of Rabbit IgG. (A) 0 ng mL^{-1} Rabbit IgG; (B) 1 ng mL^{-1} Rabbit IgG; (C) 5 ng mL^{-1} Rabbit IgG.

3.4. Optimization of Experimental Parameters.

The amount of captured Ab_1 on the LFSB test zone affects the LFSB response. Figure 25A presents the effect for the Ab_1 amount on the signal-to-noise (S/N) ratio of the LFSB. The amount of Ab_1 on the test zone was determined by the dispensing cycles of the Ab_1. The S/N ratio was the highest for one dispensing cycle of Ab_1 on the test zone. The decreased S/N with more dispensing cycles resulted from the higher background signal. Therefore, one dispensing cycle was used as the optimal condition in the following experiments.

The amount of Ab_1 on the AuNP-SiNRs surface affects the LFSB's immunoreaction efficiency and sensitivity. We optimized the Ab_1concentration in the conjugation solution. The LFSB's S/N ratio increased up to 10 μg mL^{-1} Ab_1 in the conjugation solution; a further concentration increase caused a decreased S/N ratio (Figure 25B). As a result, 10 μg mL^{-1} of Ab_1 antibodies were employed to prepare the

Ab_1-AuNP-SiNR conjugates in the following experiments.

The running buffer's composition is one of the main factors in developing a biosensor because it has a significant impact on the efficiency of antibody-antigen binding and the elimination of nonspecific adsorption. Several buffers, including PBS (1% BSA), PBST (1% BSA), and Tris-HCl (1% BSA), were tested, and the results are shown in Figure 25C. The highest S/N ratio was obtained with the PBST (1% BSA) buffer. Therefore, a PBST (1% BSA) buffer was selected for the experiments.

The band intensities depended on the Ab_1-AuNP-SiNR conjugates captured on the test and control zones which, in turn, corresponded to the amount of conjugates on the conjugate pad. To obtain a maximum response using a minimal amount of Ab_1-AuNP-SiNR conjugates, theAb_1-AuNP-SiNRs on the conjugate pad were optimized by increasing the volume of the Ab_1-AuNP-SiNR conjugates loaded on the conjugate pad. Figure 25D displays the histogram for the LFSB's S/N ratio with an increasing volume of conjugate solution (0.8 to 8 μL). It can be seen that the S/N ratio increased up to 4 μL; a further volume increase caused a decreased S/N ratio. The S/N ratio loss at a high volume may be attributed to the saturation of signal intensity and an increased nonspecific adsorption. Therefore, 4 μL of Ab_1-AuNP-SiNR conjugate were employed as the optimal volume for the entire study.

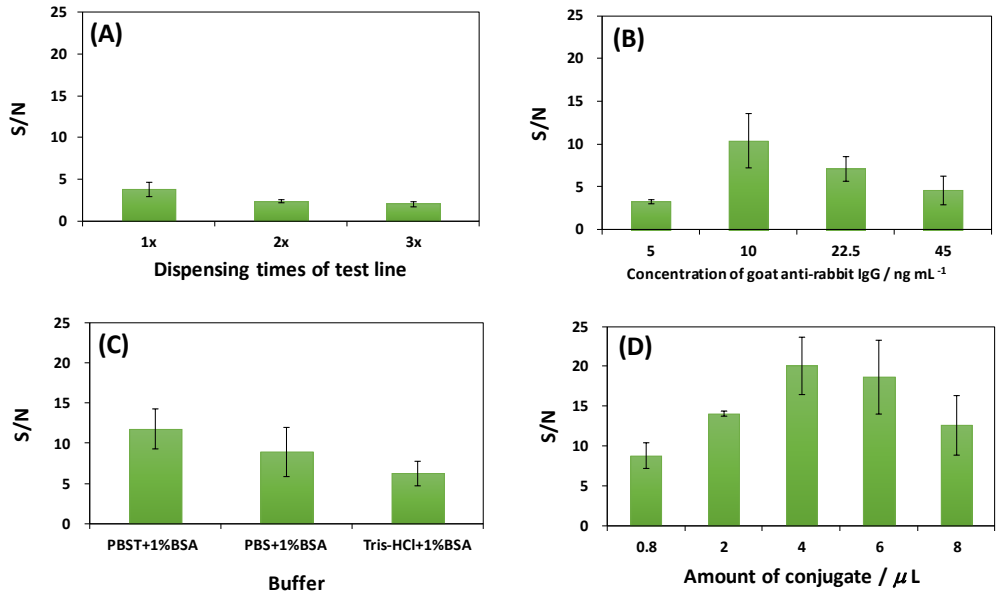

Figure 25. (A) Effect of dispensing cycles of Ab_1 on the S/N ratio of LFSB; (B) Effect of Ab_1 concentration in conjugates solution on the S/N ratio of LFSB; (C) Effect of running buffer components on the S/N ratio of LFSB; (D) Effect of the loading volume of Ab_1-AuNPs-SiNRs conjugates on the S/N ratio of LFSB. Rabbit IgG concentration: 1 ng mL^{-1}.

3.5. Analytical Performance.

Under optimal experimental conditions, we examined the performance of the AuNP-SiNR-based LFSB with different concentrations of rabbit IgG. Figure 26 presents the typical photo images (right) and the corresponding optical response recorded with a portable strip reader in the presence of different concentrations of rabbit IgG (0 to 2.0 ng mL^{-1}). There was no test line observed on the LFSB test zone in the absence of rabbit IgG (control), indicating negligible, nonspecific adsorption under the optimized experimental condition. The test line was quite visible, even at 0.05 ng mL^{-1} rabbit IgG which can be used as the threshold for the visual determination (yes/no) of rabbit IgG without instrumentation.

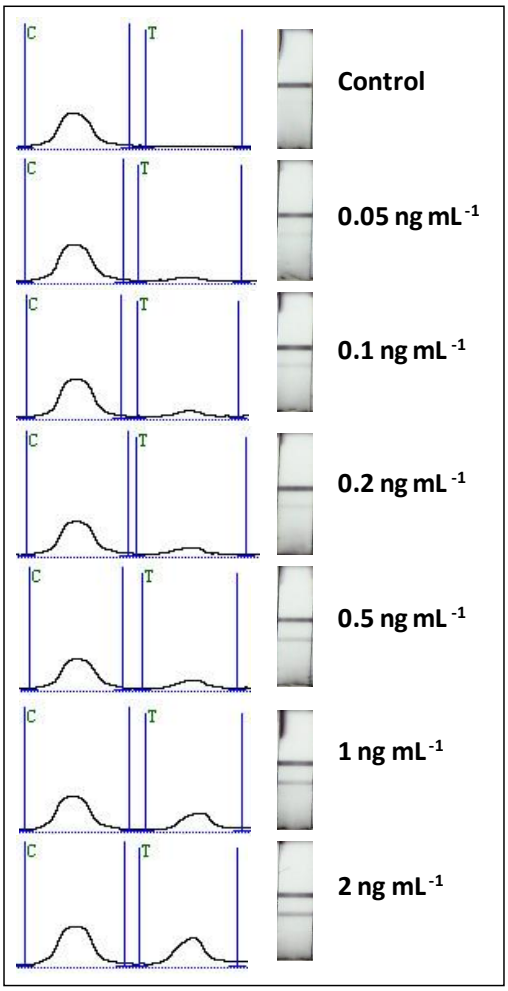

Figure 26. Typical response curves and photo images of the lateral flow biosensor with increasing Rabbit IgG concentration (0.05 – 2 ng mL^{-1}).

In addition, quantitative detection was performed by recording the peak areas of the test bands with the aid of a portable strip reader (Figure 27).The peak area had a linear correlation with the rabbit IgG concentration in the lower concentration range (0.05 – 2 ng mL^{-1}) as shown in the inset of Figure 27. The calibration equation was determined to be peak value A = 188.76C + 61.908 with a correlation coefficient of 0.9941, where A and C represent the peak area and the concentration of rabbit IgG, respectively. The detection limit was estimated to be 0.01 ng mL^{-1} from 3 times the standard deviation corresponding to the blank sample detection (S/N = 3), which was 50 times lower than the traditional AuNP-based LFSB.

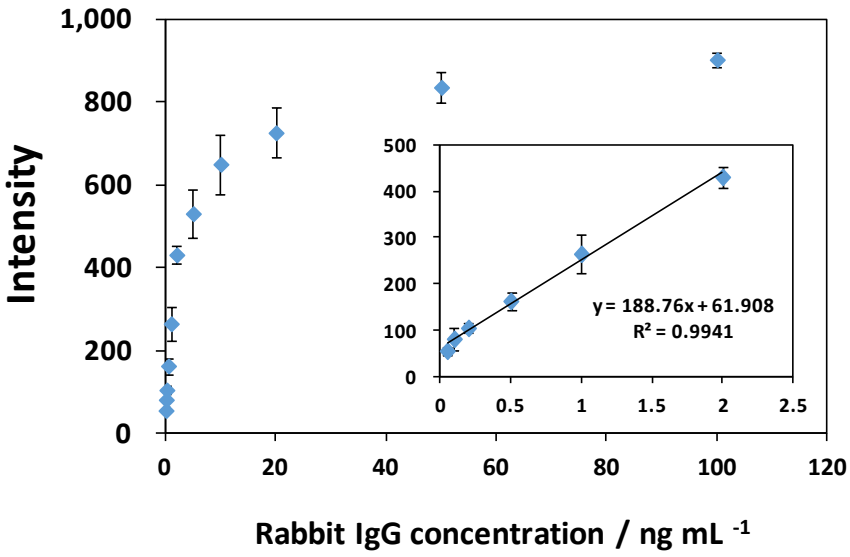

Figure 27. Calibration curve of the biosensor. The inset shows the linear response for Rabbit IgG. Each data point represents the average value obtained from three different measurements.

3.6. Selectivity and Reproducibility.

Selectivity and reproducibility are two important parameters to evaluate a biosensor's performance. The selectivity of the AuNP-SiNR-based LFSB was assessed by testing the responses of other proteins (thrombin, CEA, human IgG, and PDGF-BB) at 100 ng mL^{-1}, as well as the mixtures of rabbit IgG (1 ng mL^{-1}) and the non-target protein (100 ng mL^{-1}). Figure 28 presents the histogram of the responses (A) and the corresponding photo images (B). Excellent selectivity for rabbit IgG, over other proteins, was achieved. The sensitive and specific response was coupled with high reproducibility. The reproducibility of the AuNP-SiNR-based LFSB was studied by testing the sample solutions at different concentration levels (0, 0.5, 5, and 50 ng mL^{-1} of rabbit IgG). Samples from the same batch preparation and at the same concentration level were tested 6 times with 6 different LFSBs. Similar responses were obtained at the same concentration level. The relative standard deviations for the signals were 1.80%, 6.63%, 3.93%, and 5.49% for 50, 5, 0.5, and 0 ng $mL^{-1}$of rabbit IgG, respectively, indicating an excellent reproducibility.

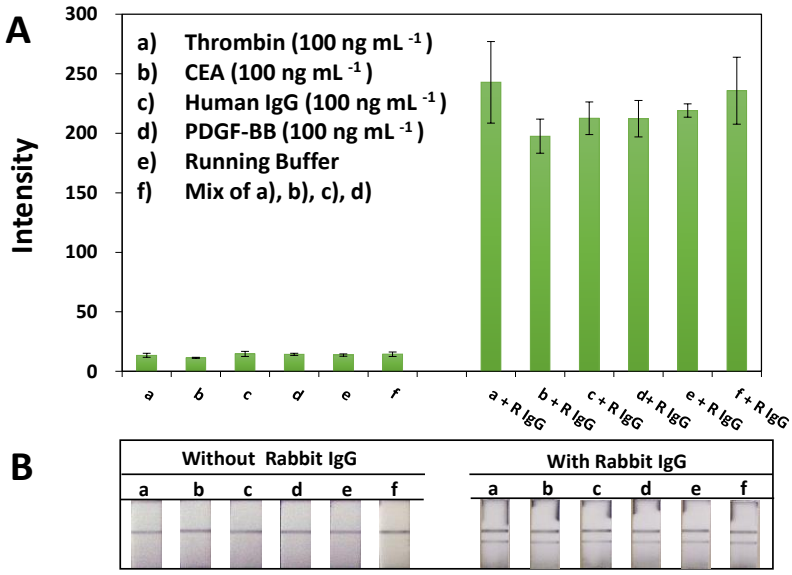

Figure 28. Reproducibility study in the presence of 50, 5, 0.5, and 0 ng mL^{-1} Rabbit IgG. Tests were performed six times for each sample solution.

4. Conclusions

We have developed a highly sensitive lateral-flow strip biosensor (LFSB) using AuNP-SiNRs as labels. The LFSB detection limit was lowered 50 times compared to the traditional AuNP-based lateral-flow assay. As demonstrated here, the significance of this work is to introduce a new type of nanolabel for signal enhancement by coupling with the lateral-flow immunoassay. In addition, the AuNP-SiNRs can be used as nanolabels for nucleic acid and other biological, molecular detection with high sensitivity. Future work will aim to detect cancer biomarkers (proteins and nucleic acids) in human blood or serum.

CHAPTER IV

AU-SILICA NANOWIRE NANOHYBRID AS A HYPERTHERMIA AGENT FOR PHOTOTHERMAL THERAPY IN THE NEAR-INFRARED REGION

1. Introduction

Core-shell nanohybrids made from a metal shell possess tunable optical properties.[73, 136-138] The most notable optical feature of such nanohybrids is the surface plasmon resonance absorption. By changing the core dimensions and the shell thickness, their plasmon resonances can be tuned continuously from ultraviolet to infrared regions of the electromagnetic spectrum, including the near-infrared (NIR) region.[139-140] In the NIR region, light transmission in tissues is much higher than that in the UV-vis region due to low light scattering and absorption from intrinsic chromophores. This results in low-energy absorption of NIR light by normal tissues, and thus limited damage to normal biological tissues while selectively killing cancer cells.[141-143] Among various metal shells, gold nanoshells are of special interest due to their inertness in biological medium, good biocompatibility, and easy bioconjugation.[144-149] Therefore, gold nanoshells have attracted considerate attention in a broad range of applications, including optical communications, biological systems for medical imaging, diagnostic and therapeutic applications, *etc*.[150-153]

A number of materials have been used for making a core of core-shell nanohybrids.[154-157] Recently, gold shells with various shapes of silica cores have been successfully constructed for Raman and fluorescence signal enhancing and drug delivery.[44, 137, 158-161] Silica nanomaterials have shown great promise in various fields due to their unique physical and chemical stability, large surface area, and well-established surface modification.[162-165] Moreover, the gold shell-silica core nanohybrids with a strong NIR absorption could convert photo energy into cytotoxic heat upon NIR laser irradiation. Thus, gold shell-silica core nanohybrids have been

considered as hyperthermia agents for photothermal therapy (PTT).[148] However, most of these photothermolysis studies require high laser power irradiation to destroy cancer cells. A common range of this power, 1.5 – 48.6 W/cm^2,[166-169] is higher than the maximal permissible exposure (MPE) of skin per ANSI (American National Standard for Safe Use of Lasers) regulation (*e.g.*, 0.4 W/cm^2 at 850 nm).[170] Therefore, the design of more efficient and safe photothermal materials is a high need.

Silica nanowires (SiNWs) are relatively new silica nanomaterials and have attracted great attention due to their unique physical and chemical stability and efficient photoluminescence emission.[171-172] Meanwhile, SiNWs have stimulated considerable interests in making biological and environmental sensing devices owing to their large surface area, high loading capacity for large molecules, excellent reservoir characteristics, and the well-established protocols for surface modification with bioselective coatings.[173-174] For example, Ramgir *et al.* applied SiNW as an effective template for the real-time detection of potential lung cancer biomarkers (interleuking-10). Due to the high surface to volume ratio, the SiNWs greatly enhanced the loading of a specific capture antibody toward a particular cancer antigen, resulting in a low detection limit down to 1 fg/mL in ideal pure solution and 1 pg/mL in clinically relevant samples.[175]

In this work, SiNW was used as a core to make the core-shell nanohybrid. With the modification of numerous gold nanoparticles (AuNPs) on the surface of SiNWs, we found that this new type of nanohybrid material had strong absorption in the NIR region and can efficiently generate heat under NIR irradiation. Remarkably, a much lower laser power irradiation, 0.30 W/cm^2, lower than the MPE of skin, was enough for photodestruction of cancer cells *in vitro* by applying the Au-SiNW nanohybrids. The optimal conditions of the Au-SiNW nanohybrids as hyperthermia

agents for photothermal cancer therapy were studied. Our results demonstrated that this new nanohybrid could be a potential candidate for new photothermal materials.

2. Experimental Section

2.1. Materials and Instruments.

Tetraethylorthosilicate (TEOS, 98%) was purchased from Acros Organics. Sodium citrate (Na_3Ct), gold (III) chloride trihydrate ($HAuCl_4 \cdot 3H_2O$, 99.9+%), hydroxylamine hydrochloride (98%, ACS grade), sodium borohydride ($NaBH_4$, > 98%) were purchased from Sigma Aldrich Inc. Ammonium hydroxide (NH_4OH, 28.0% – 30.0%), potassium carbonate ($K_2CO_3 \cdot 1.5\ H_2O$, ACS grade), dimethyl sulfoxide (DMSO), and (4-(2-hydroxyethyl)-1-piperazineethanesulfonic acid (HEPES), and ethanol (95%)were obtained from Fisher Scientific Co. Polyvinylpyrrolidone molecule (PVP, average molecular weight M_n = 40,000)and 1-pentanol (99+%, ACS grade) were purchased from Alfa Aesar. Sodium dodecyl sulface (SDS) was purchased from BioRAD. Dulbecco's modified eagle medium (DMEM) was obtained from Thermo. Human lung epithelial cells (A549 cells), SW620, and KW12C were obtained from American Tissue Culture Collection (ATCC). A 96-nonradioactive-cell proliferation assay (MTT) kit was purchased from Promega. Vybrant apoptosis assay kit was obtained from Molecular Probe. Deionized water with resistivity of 18.2 MΩ·cm was used in all experiments.

A Hitachi SU8010 field emission scanning electron microscope (SEM) was used to take images of the developed nanohybrids. The elemental analysis of the nanohybrids was achieved by performing energy-dispersive X-ray spectroscopy (EDS) measurements using an Oxford X-Max EDS that is attached to the Hitachi SU8010 field emission SEM. A Shimadzu UV-vis spectrophotometer was used to measure sample absorbance. The size of Au seed was measured using a Zeta sizer (Marlwen,

model of Nano-ZS). A BWF1 series fiber-coupled diode laser system (750 mW at 808 nm) from B&W TEK Inc. was used for photothermal effect study. A SK-1250MC electronic thermometer was purchased from Sato Keiryoki MFG. CO., Ltd.

2.2. Synthesis of Silica Nanowires (SiNWs).

An efficient approach to synthesize SiNWs has been developed in our lab. In a typical synthetic process, 3.00 g PVP was completely dissolved in 30.00 mL of 1-pentanol under the sonication of 20 min. After mixing the PVP with 1-pentanol, a 3.00 mL aliquot of 95% ethanol, 0.84 mL of H_2O, 0.20 mL of 0.17 M Na_3Ct, 0.30 mL of NH_4OH, and 0.30 mL of TEOS were added in succession. The mixed solution was well-shaken. The reaction was allowed to proceed overnight at room temperature. The synthesized SiNWs were centrifuged at the speed of 6,500 rpm for 30 min and then washed 3 times by ethanol. Finally the SiNWs were dissolved in water to prepare a 10.00 mg/mL SiNWs stock solution.

2.3. Preparation of Au Seeds.

The gold layer growing method has been well studied in our group.[44] Before growing the gold layer on the surface of SiNWs, Au seeds were synthesized based on a literature method.[176] In a typical Au seed synthesis, 4.00 mL of 1.00% $HAuCl_4$ solution was added into 100.00 mL water in an ice bath, followed the addition of 0.50 mL of 0.20 M K_2CO_3. The solution was stirred for 10 min until the color turned from bright yellow to colorless (or light yellow). A 5.00 mL aliquot of 0.50 mg/mL $NaBH_4$ solution was then slowly added to the above solution. The formation of reddish solution indicated the successful synthesis of Au seeds. The prepared Au seeds were kept in a refrigerator at 4.0 °C for future use.

2.4. Gold Layer Growth.

A 1.00 mL aliquot of 10.00 mg/mL SiNW solution was dropwise added into

40.00 mL of Au seeds and allowed to react for 10 min under vigorous stirring. Surplus Au seeds were removed by centrifugation at a speed of 6,500 rpm for 10 min and then the supernatant was carefully removed. The purplish red precipitate was Au seed-modified SiNWs and was resuspended into 10.00 mL water. The gold growth solution consisted of 2.00 mL (or 0.50, 1.00, 4.00 mL) of 1.00% $HAuCl_4$ and 0.025 g of K_2CO_3 in 90.00 mL of water. The growth solution was vigorously stirred until it turned to light yellow or colorless. A 10.00 mL aliquot of pre-synthesized Au seed-modified SiNWs was added into the growth solution, followed by the addition of 1.00 mL of 0.50 M hydroxylamine hydrochloride. Then, 1.00 g PVP was added into the above solution to stabilize the nanohybrids. After an overnight stirring, the solution was centrifuged at a speed of 6,500 rpm for 15 min and washed 3 times by ethanol.

2.5. Au Seeds Coating on Calcination-treated SiNWs.

The SiNWs synthesized from Section 2.2 were calcinated at 400 °C for 4 h to move the PVP molecules. The calcination-treated SiNWs were then dissolved in water to prepare a concentration of 10 mg/mL solution. A 1.00 mL aliquot of 10.00 mg/mL calcination-treated SiNW solution was dropwise added into 40.00 mL of Au seeds and allowed to react for 10 min under vigorous stirring. The solution was then centrifuged at a speed of 6,500 rpm for 10 min and the supernatant was removed.

2.6. Cell Proliferation Assay for Studying Cytotoxicity of the Au-SiNW Nanohybrids.

The cytotoxicity of the Au-SiNW nanohybrids was investigated using (3-(4,5-dimethylthiazol-2-yl)-2,5-diphenyltetrazolium bromide (MTT, a cell proliferation assay).[177] Three different cancer cells, including human alveolar epithelial A549 cells, SW620, and KW12C were cultured onto a 96-well plate at 37 °C for 24 h. Then, each well was added 10.00 μL of MTT reagent with a final

concentration of 1.00 μg/mL. The cells were further incubated at 37 °C for 4 h until the purple-color developed. Afterwards, 100.00 μL of stop solution (10% DMSO, 10% SDS in 50 mM HEPES buffer) was added into each well and the cells were continuously incubated overnight at 37 °C. The absorbance of each well was recorded at 560 nm to determine the cell proliferation rate.

2.7. Vybrant Apoptosis Assay.

Cell apoptosis and necrosis were detected using the Vybrant apoptosis assay. A549 cells were pre-cultured in a DMEM culture medium overnight and the final cell number was ~ 1 × 10^5/well. Then, a final concentration of Au-SiNW nanohybrids varying from0.100 mg/mL, 0.050 mg/mL, 0.025 mg/mL, to 0.010 mg/mL, was obtained in each well of the plate. The cells were incubated at 4 °C for 30 min and then at 37 °C for 2 h. Next, the cells were treated with an 808 nm laser irradiation for 20 min. The cells were washed 3 times using a fresh cell culture medium and then treated with the fluorescence probe, propidium iodide (PI) and YO-PRO-1 dyes (Vybrant apoptosis assay kit), for 10 min.[178] The cells were observed immediately under a Zeiss confocal fluorescence microscope. The population separated into three groups: live cells with no fluorescence signals, apoptotic cells with high green fluorescence, and necrotic cells with red fluorescence.

3. Results and Discussion

3.1. Synthesis of Au-SiNW Nanohybrids.

3.1.1. Au Seed Modification.

We first developed a relatively simple method to coat a gold layer on a silica matrix to synthesize the Au-SiNW nanohybrids. The gold layer decoration on the surface of SiNWs was accomplished through a two-stage deposition process. The first step was the seed deposition and the second was the seeded growth. The unique

feature of this method was to directly deposit Au seeds onto the surface of SiNWs without any surface modification in the seed deposition step. Surface modification in the process of Au-seed deposition was required in most published methods, which constituted complicated synthetic procedures and low reproducibility.[170-171] This step was completely eliminated in our method. The diameter of synthesized Au seeds was measured to be 9.7 ± 1.6 nm using a particle size analyzer. The seed deposition was obtained by simply mixing the Au seeds and the SiNW solution for 10 min and an evenly-deposited Au seed layer formed on the surface of the SiNWs (Figure 29A).

The mechanism of the Au seed direct deposition on the SiNWs was studied. The presence of PVP on the SiNWs was a key factor. As described in Section 2.2, PVP was added during the synthesis of SiNWs as a surfactant and stabilizer to form the PVP-water droplets in the microemulsion. The hydrolysis and polymerization of TEOS occurred in the interface of PVP-water droplets and oil phase. With continuous reaction, the PVP-water droplet moved to one end and the silica continued to grow along this direction and resulted in an ultra-long SiNW (Figure 29B).Although a few cycles of washing were employed after the synthesis of SiNWs, the PVP was not completely washed away. Previous studies have shown that PVP was adsorbed to a broad range of materials including metals (*e.g.*, gold, silver, and iron), metal oxides, silica, *etc*.[79, 179] Thus, the remaining trace PVP used in the synthesis of SiNWs provided the Au seeds with an easy deposition on the SiNW surface.

Two experiments were conducted to confirm that PVP plays a role in deposition of Au seeds. In the first experiment, we compared our SiNWs with the pure silica nanoparticles that were synthesized with a similar procedure but without the addition of PVP (Figure 29C). When mixing the silica nanoparticles with the Au seeds, few or no Au seeds were decorated on the surface of silica nanoparticles (Figure 29D),

showing the crucial role of PVP. The Au seed-decorated SiNWs were then used to nucleate the growth of a gold layer. With the addition of a reducing reagent, hydroxylamine hydrochloride, the Au seeds grew to form a uniform Au layer in the presence of $HAuCl_4$.

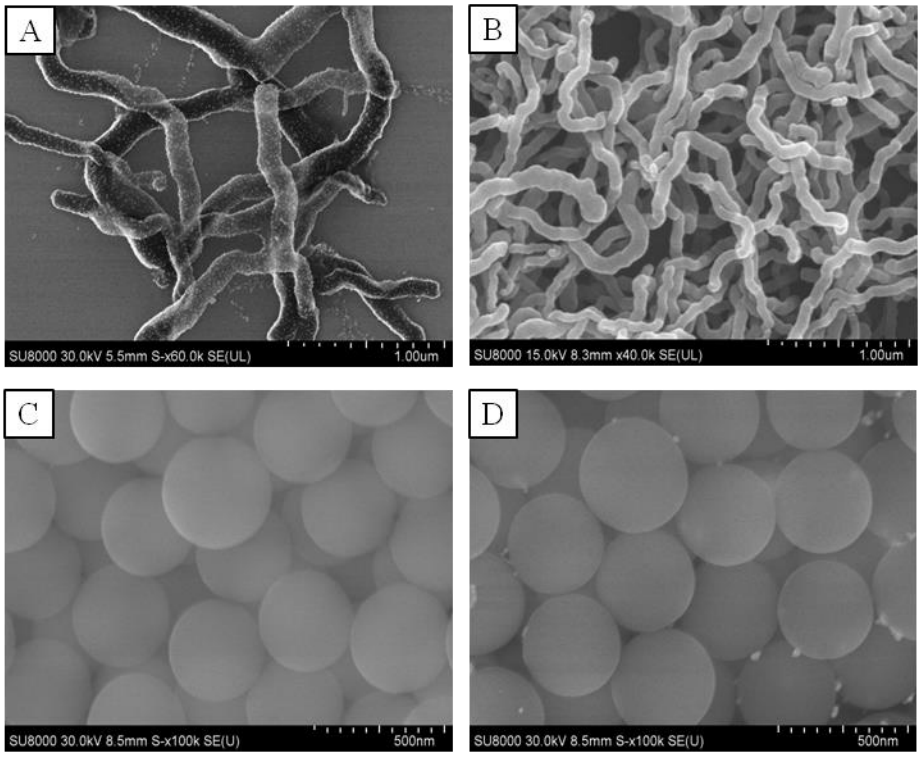

Figure 29. SEM image of (A) SiNWs coated with Au seeds, (B) pure SiNWs, (C) pure silica nanoparticles, and (D) silica nanoparticles coated with few Au seeds due to no PVP used in the synthesis.

In the second experiment, the synthesized SiNWs were treated in a calcination process at 400 °C for 4 h. It has been well-studied that PVP molecules can be removed at high temperature.[180-182] The calcination-treated SiNWs were then stirring with Au seeds (as described in Section 2.5). As shown in Figure 30, no Au seeds were coated on the surface of SiNWs due to the absence of PVP. Both of these two experiments prove the importance of PVP on the deposition of Au seeds on the SiNW surface.

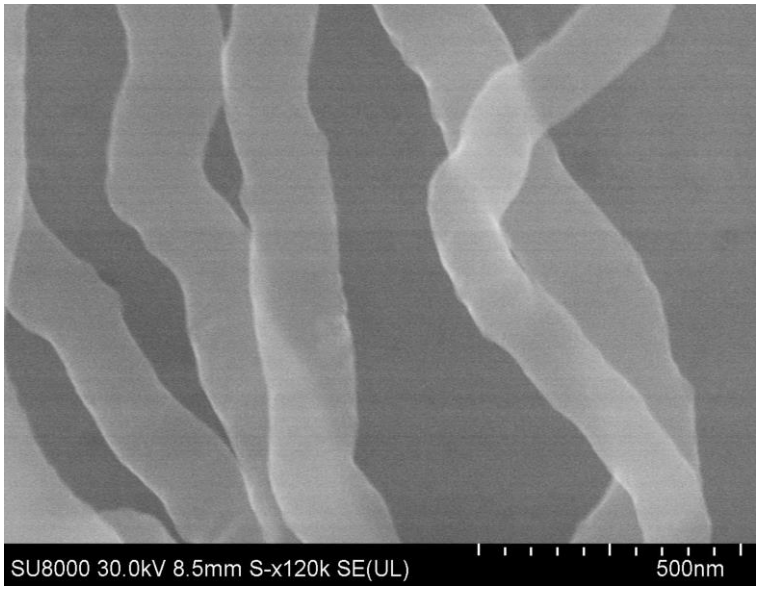

Figure 30. SEM image of calcination-treated SiNWs after stirring with Au seeds.

3.1.2. Tune the Plasmon Resonance Band of the Nanohybrid to the NIR Region.

We were able to tune the plasmon resonance and of the nanohybrid to the NIR region by systematically increasing the thickness of the AuNP layer on the SiNWs. When the amount of $HAuCl_4$ in the Au growth solution increased, the size of AuNPs increased, resulting in different thicknesses of the AuNP layer on the SiNWs. Figure 31A – D showed the SEM images of SiNWs modified with various sized AuNPs. The size of AuNPs on the surface of SiNWs was statistically measured based on over 200 AuNPs. The resulted was shown in Figure 31E. When 4.0 mL of 1% $HAuCl_4$ was used in the Au growth solution, the size of the AuNP increased to 57.3 ± 16.9 nm. The morphology of AuNPs on the surface of SiNWs became more irregular shape rather than a spherical shape with the increasing of $HAuCl_4$ amount. To further identify the formation of AuNP layer, the resultant nanohybrids were analyzed using the SEM-EDS elemental analysis. A representative EDS spectrum was presented in Figure 31F. As expected, Au peaks were observed in the spectrum confirming the existence of gold element. Apart from Au signals, the spectrum also showed Si and O

signals (from SiNWs), and Cu signal (from the copper grid).

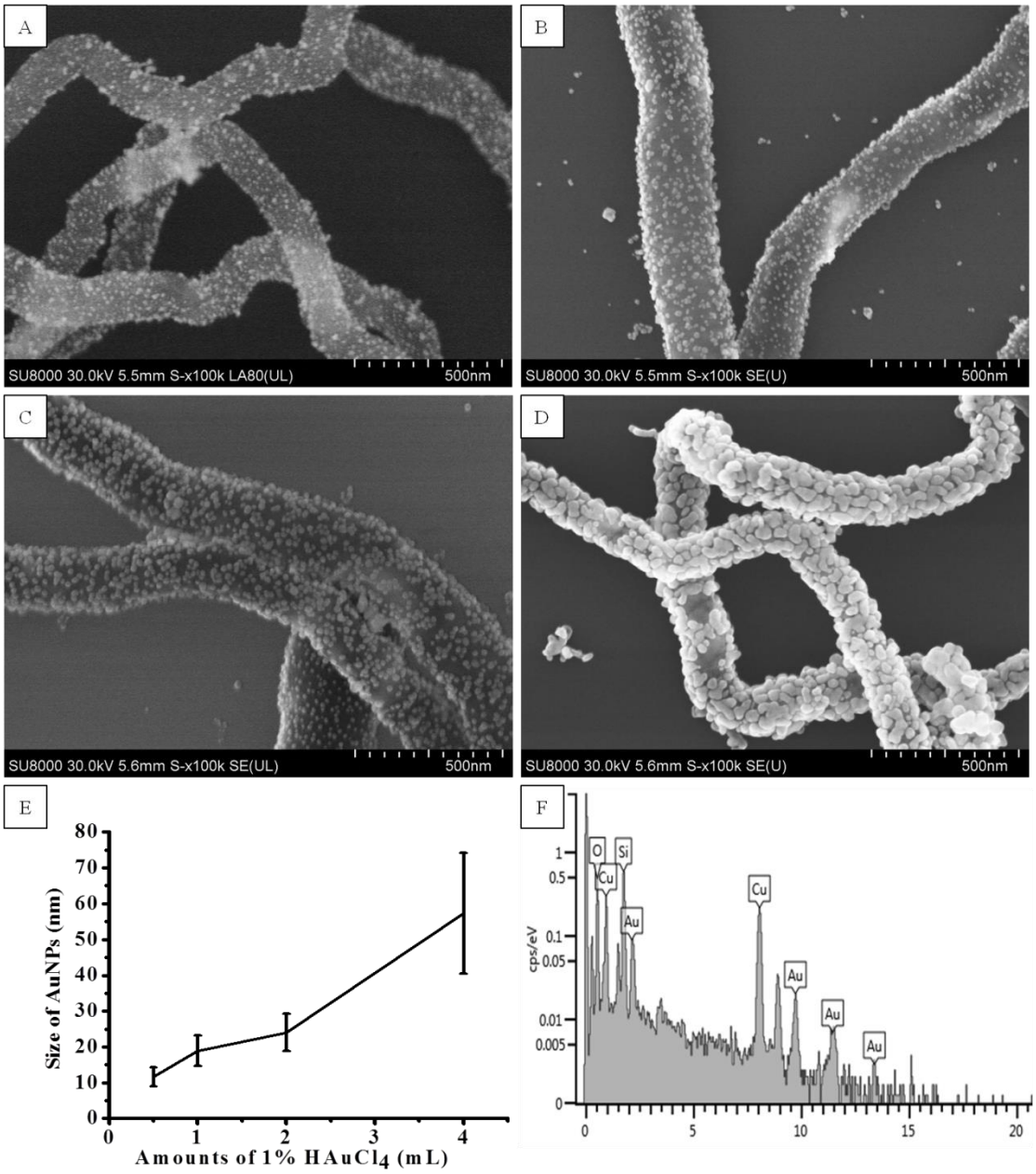

Figure 31. The Au-SiNW nanohybrids. (A) – (D) SEM images of different thicknesses Au layer on SiNW obtained by adding 0.50 mL (A), 1.00 mL (B), 2.00 mL (C), and 4.00 mL (D) of 1.00% $HAuCl_4$ in the gold growth solution; (E) The statistical measurement of the AuNP size; (F) A representative EDS spectrum obtained from the Au-SiNW nanohybrids.

The plasmon resonance and of the nanohybrid was tuned to the NIR region when the AuNP size increased to certain value (Figure 32). The freshly prepared Au seeds showed a peak around 514 nm (Figure 32a) that is consistent with the

literature.[183] Upon the attachment of Au seeds on the surface of SiNWs before the addition of growth solution, the plasmon band appeared at 520 nm (Figure 32b), which was slightly red-shifted compared to that of free Au seeds (514 nm). The absorption peak of Au-SiNW nanohybrids increased with the size changes of AuNPs on the surface of SiNWs (Figure 32c – f). With a thicker gold layer, the absorption peak red shifted toward the NIR region and the peak shape became broader. The broad absorption in the NIR region suggested that the Au-SiNW nanohybrids would be suitable for photothermal therapy. In the NIR region tissues and biological samples have the minimum light absorption, and thus the irradiation has low influence on normal cells. However, pure SiNWs showed little or no NIR absorption (Figure 32g). Although the sample with the thickest gold layer (57.3 ± 16.9 nm) had the highest absorption at 808 nm (Figure 32b), a large number of free AuNPs were obtained besides the Au-SiNW nanohybrids. Therefore, the Au-SiNW nanohybrids used in the following work were synthesized by adding 2.00 mL of 1.00% $HAuCl_4$ to form a gold layer thickness of 24.0 ± 5.2 nm.

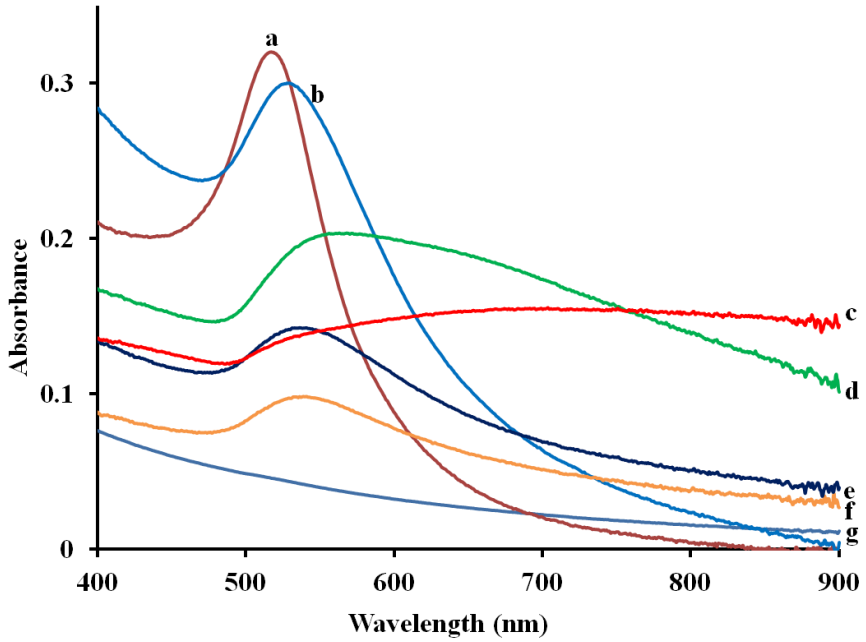

Figure 32. UV-vis spectra of free Au seeds(a), Au-seed coated on SiNWs (b), Au-SiNW nanohybrids by adding 4.00 (c), 2.00 (d), 1.00 (e), and 0.50 mL of 1.00% $HAuCl_4$ (f), and pure SiNWs (g).

3.2. Concentration Effect of Au-SiNW Nanohybrids on Plasmon Resonance.

The concentration of nanomaterials usually affects their plasmon resonance absorption intensity. Thus, we first investigated light absorption capabilities of the nanohybrids under various concentrations. The spectra shown in Figure 33A indicated that the concentration dependent nature of the nanohybrids. As the concentration increased from 0.00625 mg/mL to 0.200 mg/mL, the absorbance at 808 nm raised from 0.0533 to 1.3066. It gave a good linear correlation (R^2 = 0.9983) between the absorbance at 808 nm and the concentration of Au-SiNW nanohybrids (Figure 33B). Overall in the NIR region the nanohybrids exhibited strong optical absorption even at low concentrations. As a comparison, we tested pure absorption ability of SiNWs. Their absorption in the NIR region was much weaker (Figure 33C). For example, the absorbance of Au-SiNW nanohybrids reached 0.67 at a concentration of 0.100 mg/mL while only 0.03 for pure SiNWs at the same concentration.

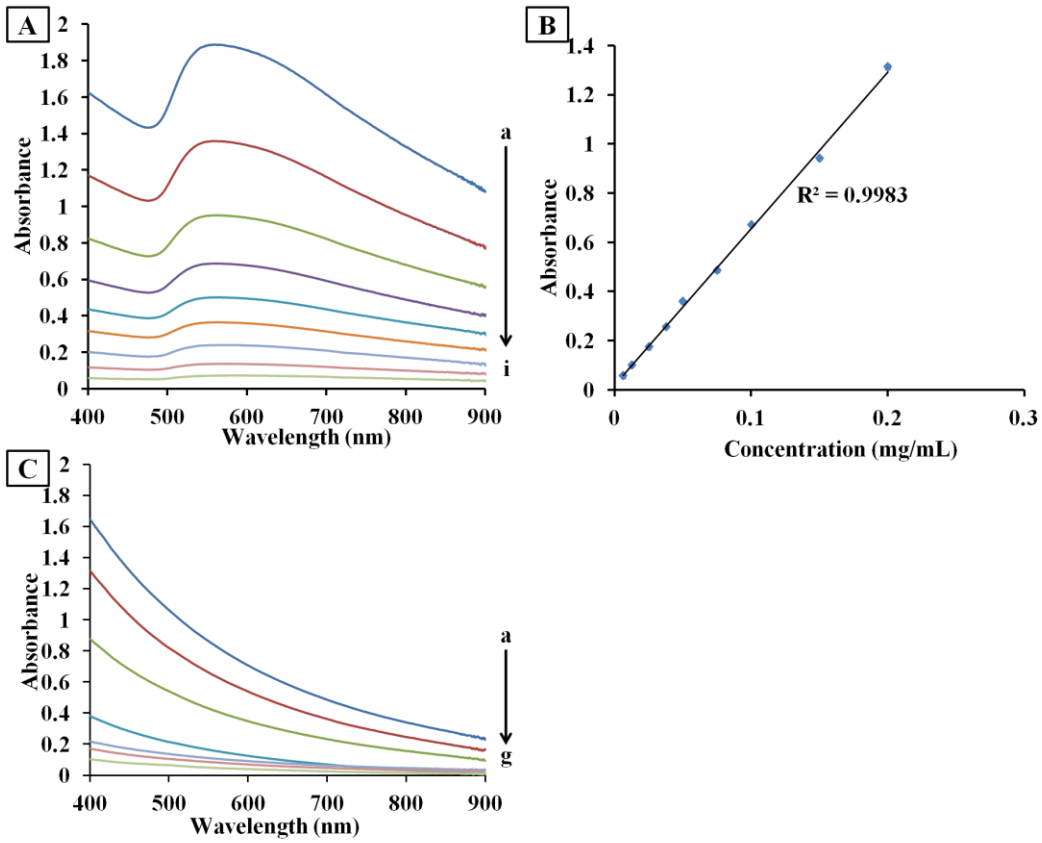

Figure 33. (A) UV-vis spectra of Au-SiNW nanohybrids with different concentrations varying from 0.200, 0.150, 0.100, 0.0750, 0.0500, 0.0375, 0.0250, 0.0125, to 0.00625 mg/mL (a – i); (B) the linear relationship between concentration of Au-SiNW nanohybrids and its absorbance at 808 nm; (C) UV-vis spectra of different concentrations of pure SiNWs changing from 1.00, 0.800, 0.500, 0.250, 0.125, 0.100, to 0.0625 mg/mL (a – g).

3.3. Photothermal Capability of the Nanohybrids.

Due to their high absorption in the NIR region, the Au-SiNW nanohybrid aqueous solution was irradiated with an 808 nm NIR laser to study its heat releasing. Three controls were used including water, pure AuNPs, and pure SiNWs. As shown in Figure 34, no obvious temperature increase was observed for these three controls, indicating a low degree of temperature elevation. In contrast, the Au-SiNW nanohybrids showed a rapid rise in temperature upon exposure to the laser after a short time period of 10 min, and reached a plateau after 20 min of irradiation. In addition, a higher concentration of Au-SiNW nanohybrids displayed a sharper temperature increase. These data indicated that the Au-SiNW nanohybrids can act as

an efficient photothermal mediator.

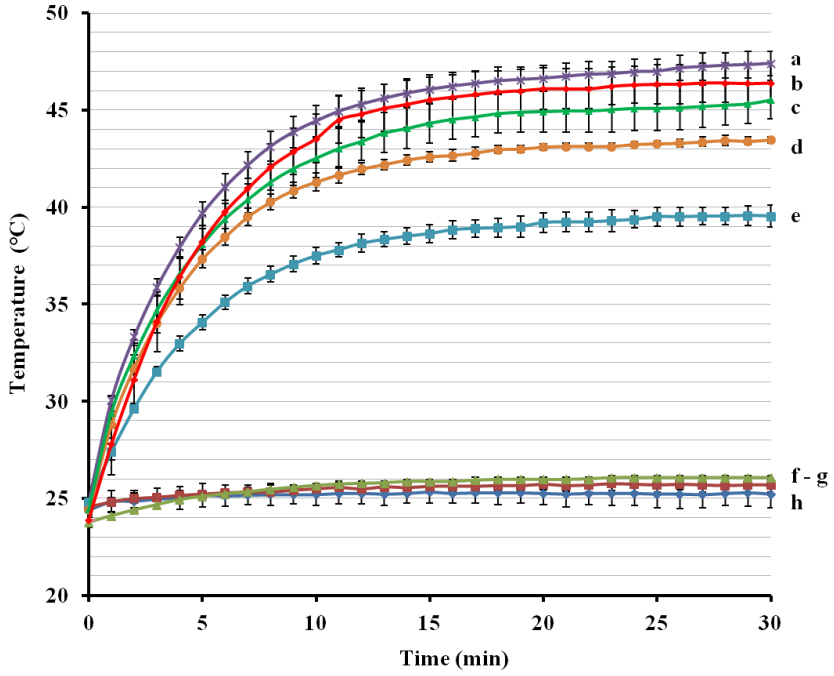

Figure 34. Heat releasing of different concentrations of Au-SiNW nanohybrids varying from 1.000, 0.500, 0.250, 0.100, to 0.050 mg/mL (a – e). Controls:1.000 mg/mL of AuNPs (f), 1.000 mg/mL of pure SiNWs (g), and pure water (h).

3.4. Cytotoxicity Evaluation of Au-SiNW Nanohybrids.

The cytotoxicity of the nanohybrids to living systems was examined prior to applying the nanohybrids to *in vitro* phototheramal therapy. A cell proliferation assay (MTT assay) that can detect cellular toxicity was performed to carry the cytotoxic evaluation. Due to the presence of PVP in the nanohybrids, we first studied the toxicity of PVP to A549 cancer cells. Different concentrations of PVP solution ranging from 0, 0.5, 1.0, 2.0, 5.0, to 10.0% were studied. Even at high concentrations (5.0 and 10.0%), the cell viability were 84% and 77%, respectively, indicating a good biocompatibility of PVP (Figure 35).

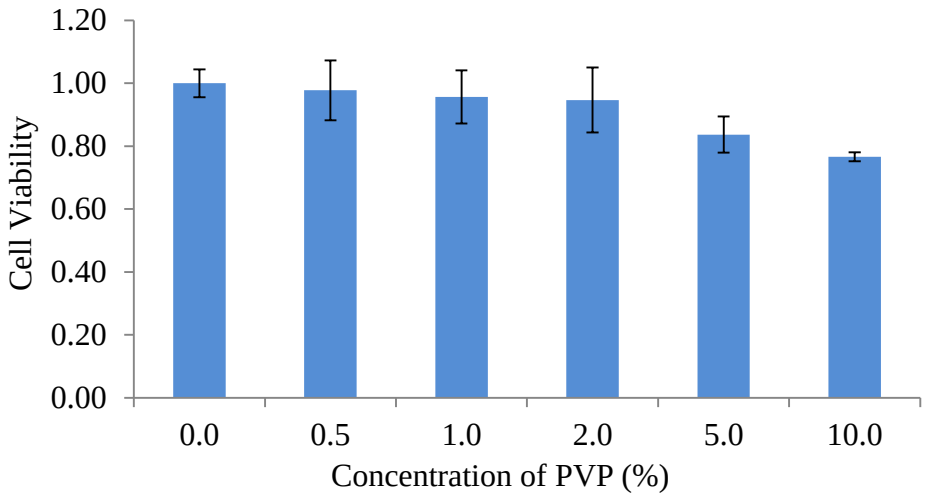

Figure 35. Relative cell viability after culturing with different concentrations of PVP varying from 0, 0.5, 1.0, 2.0, 5.0, to 10.0% for 24 h at 37 °C. After the addition of MTT reagent and 4 h incubation at 37 °C, stop solution was added and followed by overnight incubation. The absorbance of each sample was recorded at 560 nm to determine the cell proliferation rate.

We then studied the biocompatibility of this novel nanohybrid with other three cancer cells, including A549 cells, SW620, and KW12C. Different concentrations of the nanohybrids, from 0, 0.010, 0.025, 0.050, 0.075, 0.100, 0.250 to 0.500 mg/mL, were added to A549 cells in a 96-well plate and incubated for 24 h at 37 °C. After this time period, the effect on cell viability was measured as shown in Figure 36. The cell viability decreased as the concentration of Au-SiNW nanohybrids gradually increased from 0.010 mg/mL to 0.500 mg/mL, showing a concentration-dependent nanotoxicity trend. For example, at a low nanocomposite concentration ($\leq$ 0.100 mg/mL), Au-SiNW nanohybrids had no discernible cell cytotoxicity according to the student t-test ($p > 0.05$). The cell viability was decreased to 80% compared to the untreated control group when high concentrations, 0.250 mg/mL and 0.500 mg/mL, of Au-SiNW nanohybrids were used.

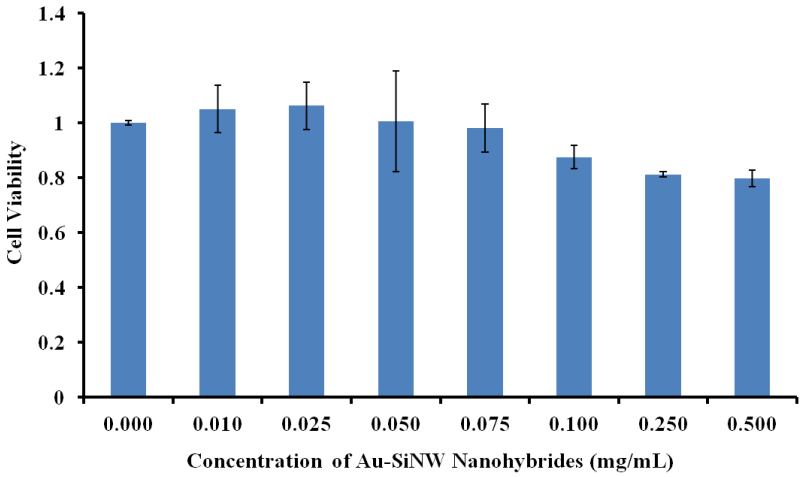

Figure 36. Relative cell viability after culturing with different concentrations of Au-SiNW nanohybrids varying from 0.000, 0.010, 0.025, 0.050, 0.075, 0.100, 0.250, to 0.500 mg/mL for 24 h at 37 °C. After the addition of MTT reagent and 4 h incubation at 37 °C, stop solution was added and followed by overnight incubation. The absorbance of each sample was recorded at 560 nm to determine the cell proliferation rate. The cell used here is A549 cell.

The Au-SiNWs toxicity was also studied in two other colon cancer cells, KW12C and SW620 (Figure 37). As shown in Figure 37, no obvious cell toxicity was observed even at a high concentration of Au-SiNWs in both cases. For example, at a concentration of 0.25 mg/mL Au-SiNWs, the cell viability was 75% and 86% for KW12C and SW620, respectively. As the toxicity observed in this assay was not dramatic, these results demonstrated that the excellent biocompatibility of Au-SiNW nanohybrids would be promising.

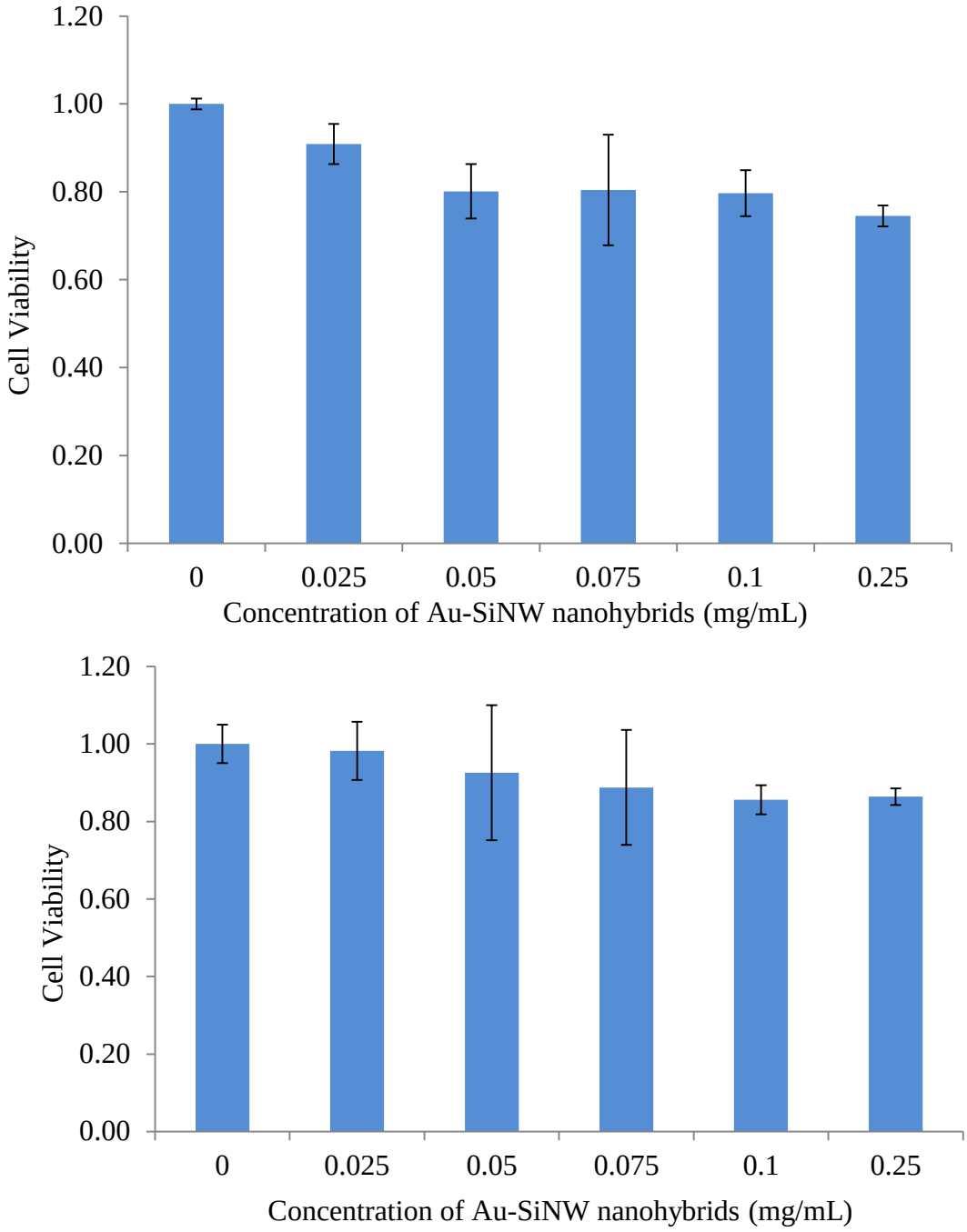

Figure 37. Relative cell viability after culturing with different concentrations of Au-SiNW nanohybrids varying from 0.000, 0.010, 0.025, 0.050, 0.075, 0.100, to0.250 mg/mL for 24 h at 37 °C. After the addition of MTT reagent and 4 h incubation at 37 °C, stop solution was added and followed by overnight incubation. The absorbance of each sample was recorded at 560 nm to determine the cell proliferation rate. The cells used here were KW12C and SW620, respectively.

3.5. *In vitro* Photothermal Therapy Application of the Nanohybrids.

An important feature of the Au-SiNW nanohybrids is the NIR-induced

thermal effect. As demonstrated in section 3.3, the Au-SiNW nanohybrids irradiated by NIR laser clearly elevated the temperature of the solution. This type of nanocomposite could absorb NIR irradiation; then converted the absorbed energy into heat and generate localized hyperthermia. This unique property brought a potential application of the nanohybrids to destroy cancer cells by NIR irradiation on a localized tumor area. To test this potential, we conducted an *in vitro* application of Au-SiNW nanohybrids for photothermal therapy. The Vybrant assay that can distinguish apoptosis and necrosis was used to investigate the PTT effects since apoptosis is considered to be preferred responses among different mechanisms of inducing tumor cell death.[184] Two dyes, the green fluorescent YO-PRO-1 and red fluorescent propidium iodide (PI), were used in the assay. YO-PRO-1dye can stain apoptotic cells by penetrating cytoplasm membrane while PI only penetrates nuclear membrane and thus staining necrotic cells. Therefore, the combination of YO-PRO-1 and PI can provide a sensitive indicator for apoptosis detection.

A549 cells were treated with Au-SiNW nanohybrids with different concentrations varying from 0, 0.010, 0.025, 0.050, to 0.100 mg/mL for 2.5 h, followed by irradiating with an 808 nm laser for 20 min. YO-PRO-1 and PI dyes were then added to stain the cells for 10 min. Apoptotic cells showed green fluorescence, whereas necrotic cells showed red fluorescence. As shown in Figure 38a, A549 cells treated by 0.100 mg/mL of Au-SiNW nanohybrids but without the treatment of NIR light irradiation, resulted in no necrotic or apoptotic cells detected. By treating A549 cells with both 0.100 mg/mL Au-SiNW nanohybrids and NIR light irradiation, significant apoptosis was induced and stained with the green color (Figure 38b). Although the concentration of Au-SiNW nanohybrids decreased to 0.050 mg/mL, most of the cells were dead after NIR irradiation (Figure 38c). Moreover, green

fluorescence was the dominant color (albeit red color staining for necrotic cells were also observed), indicating that apoptosis was the primary mechanism of cell death. Further decreasing the concentration of Au-SiNW nanohybrids resulted in reduced cell death (Figure 38d – e). These results clearly showed a typical concentration-dependent PTT effect (Figure 38b – e). As a control, no apoptosis or necrotic cells were detected when A549 cells were only treated by the NIR light in the absence of Au-SiNW nanohybrids (Figure 38f).

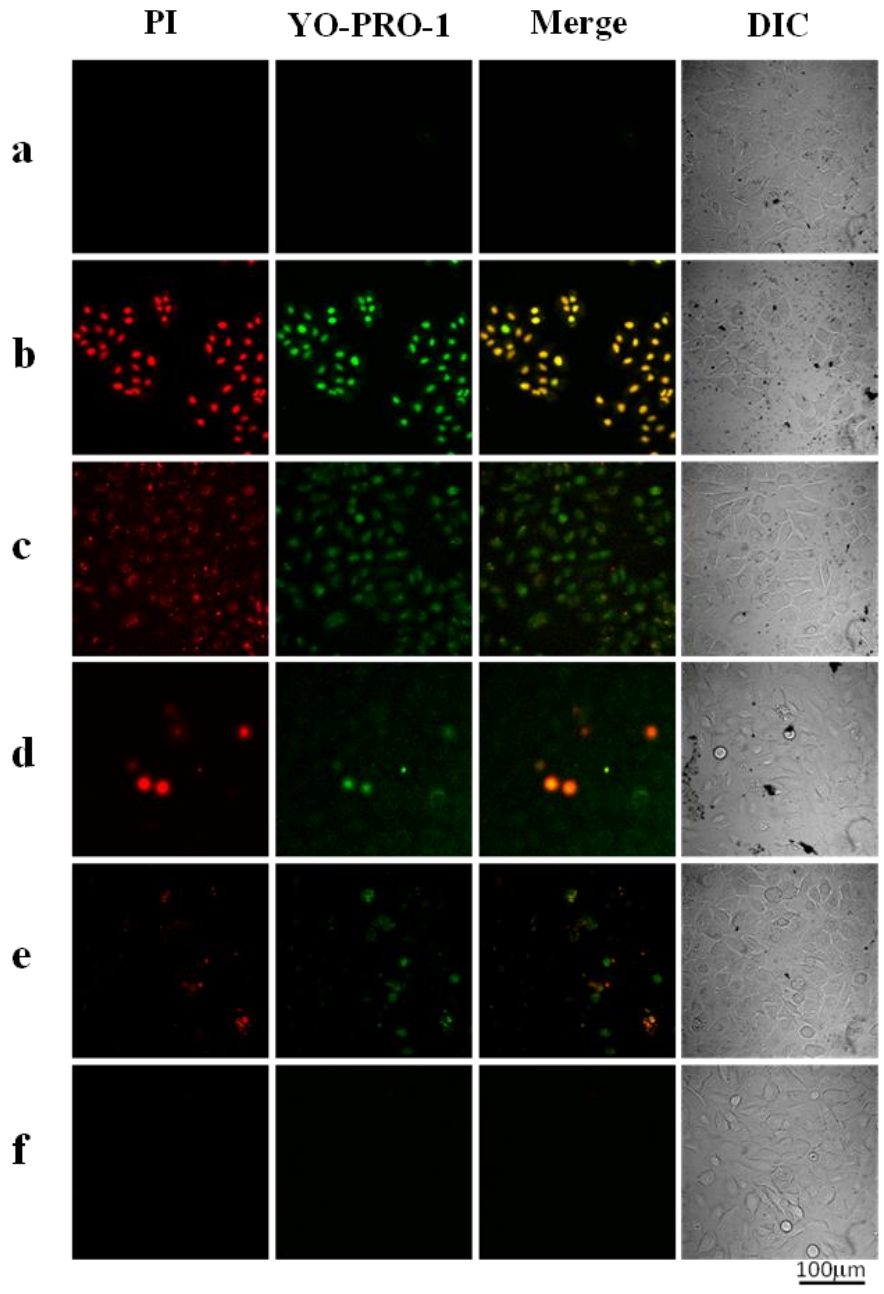

Figure 38. Confocal fluorescence images of A549 cells. A549 cells were treated with different concentrations of Au-SiNW nanohybrids and NIR light centered at 808 nm (0.30 W/cm^2) for 20 min. The concentration of Au-SiNW nanohybrids was 0.100 mg/mL without NIR irradiation (a), 0.100 mg/mL (b), 0.050 mg/mL (c), 0.025 mg/mL (d), 0.010 mg/mL (e), and 0.0 mg/mL (f) with NIR irradiation. After staining a cell population, apoptotic cells showed green fluorescence stained by YO-PRO-1, necrotic cells showed red color by PI, and control cells showed little or no fluorescence. DIC, differential interference contrast.

MTT experiments were also conducted to quantitatively study the effect of the nanohybrids and NIR irradiation. As shown in Figure 39, with the treatment of

NIR irradiation and the increasing concentration from 0.01, 0.025, 0.05, to 0.1 mg/mL, the cell viability decreased to 76.0%, 51.2%, 39.7%, and 27.1%, respectively. However, with the addition of nanohybrids or the treatment of NIR irradiation, no obvious change was observed. These data suggested that only the combination of Au-SiNW nanohybrids and NIR light irradiation can lead to cell death, which was consistence with the results form confocal images.

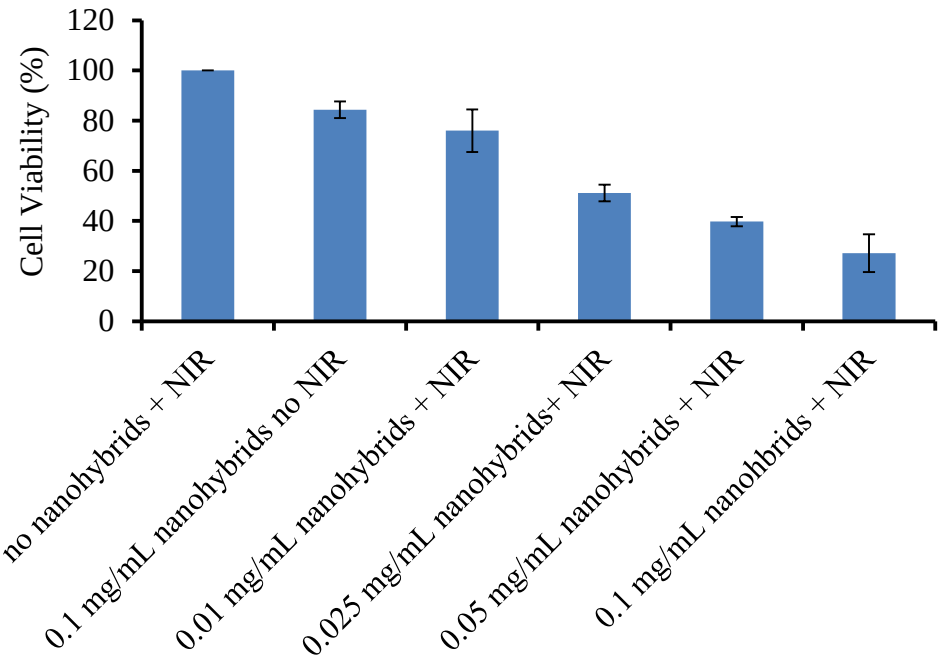

Figure 39. Relative cell viability after incubating with different concentrations of Au-SiNWs nanohybrids in the presence or absence of NIR irradiation.

4. Conclusions

In summary, a novel nanomaterial – Au-SiNW nanohybrid – was synthesized with controllable sizes of AuNPs on the surface. This new nanocomposite exhibited strong surface plasmon resonance absorption due to the growth of a gold layer on the surface of SiNWs. The absorption of Au-SiNW nanohybrids can be tuned from the visible to the NIR region simply by changing the amount of $HAuCl_4$ in the gold growth solution. This nanocomposite was found to have excellent biocompatibility.

Combining the intrinsic properties of both SiNWs and gold layer, the nanocomposites showed significantly improved photothermal cell destroying efficacy even at a low laser power density of 0.3 W/cm^2. These findings indicate that the nanocomposite may be a promising candidate for phototherapeutic cancer therapy.

REFERENCES

1. Jung, C. Y.; Kim, J. S.; Chang, T. S.; Kim, S. T.; Lim, H. J.; Koo, S. M., One-Step Synthesis of Structurally Controlled Silicate Particles from Sodium Silicates Using a Simple Precipitation Process. *Langmuir* **2010,** *26*, 5456-5461.

2. Nandiyanto, A. B. D.; Akane, Y.; Ogi, T.; Okuyama, K., Mesopore-Free Hollow Silica Particles with Controllable Diameter and Shell Thickness *via* Additive-Free Synthesis. *Langmuir* **2012,** *28*, 8616-8624.

3. Wu, H.; Tang, B.; Wu, P., Novel Hollow Mesoporous Silica Spheres/Polymer Hybrid Membrane for Ultrafiltration. *J. Phys. Chem. C* **2011,** *116*, 2246-2252.

4. Deng, T.-S.; Marlow, F., Synthesis of Monodisperse Polystyrene@Vinyl-SiO_2 Core–Shell Particles and Hollow SiO_2 Spheres. *Chem. Mater.* **2011,***24*, 536-542.

5. Jin, D.; Lee, J. H.; Seo, M. L.; Jaworski, J.; Jung, J. H., Controlled Drug Delivery From Mesoporous Silica Using a pH-Response Release System. *New J. Chem* **2012,** *36*, 1616-1620.

6. Young, K. L.; Scott, A. W.; Hao, L.; Mirkin, S. E.; Liu, G.; Mirkin, C. A., Hollow Spherical Nucleic Acids for Intracellular Gene Regulation Based upon Biocompatible Silica Shells. *Nano Lett.* **2012,** *12*, 3867-3871.

7. Liberman, A.; Martinez, H. P.; Ta, C. N.; Barback, C. V.; Mattrey, R. F.; Kono, Y.; Blair, S. L.; Trogler, W. C.; Kummel, A. C.; Wu, Z., Hollow Silica and Silica-Boron Nano/Microparticles for Contrast-Enhanced Ultrasound to Detect Small Tumors. *Biomaterials* **2012,** *33*, 5124-5129.

8. Zhai, X.; Yu, M.; Cheng, Z.; Hou, Z.; Ma, P. a.; Yang, D.; Kang, X.; Dai, Y.; Wang, D.; Lin, J., Rattle-Type Hollow $CaWO_4$: Tb^{3+}@SiO_2Nanocapsules as Carriers for Drug Delivery. *Dalton Trans.* **2011,** *40*, 12818-12825.

9. Chen, J.; Ding, H.; Wang, J.; Shao, L., Preparation and Characterization of Porous Hollow Silica Nanoparticles for Drug Delivery Application.*Biomaterials* **2004,** *25*, 723-727.

10. Li, Z.; Xu, S.; Wen, L.; Liu, F.; Liu, A.; Wang, Q.; Sun, H.; Yu, W.; Chen, J., Controlled Release of Avermectin from Porous Hollow Silica Nanoparticles: Influence of Shell Thickness on Loading Efficiency, UV-Shielding Property and Release. *J. Controlled Release* **2006,** *111*, 81-88.

11. Zhou, J.; Wu, W.; Caruntu, D.; Yu, M. H.; Martin, A.; Chen, J. F.; O'Connor, C. J.; Zhou, W. L., Synthesis of Porous Magnetic Hollow Silica Nanospheres for Nanomedicine Application. *J. Phys. Chem. C* **2007,** *111*, 17473-17477.

12. Chu, N.; Wang, J.; Zhang, Y.; Yang, J.; Lu, J.; Yin, D., Nestlike Hollow Hierarchical MCM-22 Microspheres: Synthesis and Exceptional Catalytic Properties. *Chem. Mater.* **2010,** *22*, 2757-2763.

13. Wang, Y.; Tang, C.; Deng, Q.; Liang, C.; Ng, D. H. L.; Kwong, F.-l.; Wang, H.; Cai, W.; Zhang, L.; Wang, G., A Versatile Method for Controlled Synthesis of Porous Hollow Spheres. *Langmuir* **2010,** *26*, 14830-14834.

14. Qi, G.; Wang, Y.; Estevez, L.; Switzer, A. K.; Duan, X.; Yang, X.; Giannelis, E. P., Facile and Scalable Synthesis of Monodispersed Spherical Capsules with A Mesoporous Shell. *Chem. Mater.* **2010,** *22*, 2693-2695.

15. Kato, N.; Ishii, T.; Koumoto, S., Synthesis of Monodisperse Mesoporous Silica Hollow Microcapsules and Their Release of Loaded Materials. *Langmuir* **2010,** *26*, 14334-14344.

16. Blas, H.; Save, M.; Pasetto, P.; Boissière, C.; Sanchez, C.; Charleux, B., Elaboration of Monodisperse Spherical Hollow Particles with Ordered Mesoporous Silica Shells *via* Dual Latex/Surfactant Templating: Radial Orientation of Mesopore Channels. *Langmuir* **2008,***24*, 13132-13137.

17. Tan, B.; Lehmler, H. J.; Vyas, S. M.; Knutson, B. L.; Rankin, S. E., Fluorinated-Surfactant-Templated Synthesis of Hollow Silica Particles with A Single Layer of Mesopores in Their Shells. *Adv. Mater.* **2005,***17*, 2368-2371.

18. Yuan, J.; Bai, X.; Zhao, M.; Zheng, L., C_{12}mimBr Ionic Liquid/SDS Vesicle Formation and Use as Template for the Synthesis of Hollow Silica Spheres. *Langmuir* **2010,***26*, 11726-11731.

19. Lin, Y.-S.; Wu, S.-H.; Tseng, C.-T.; Hung, Y.; Chang, C.; Mou, C.-Y., Synthesis of Hollow Silica Nanospheres with a Microemulsion as the Template. *Chem. Commun.* **2009**, 3542-3544.

20. Li, J.; Liu, J.; Wang, D.; Guo, R.; Li, X.; Qi, W., Interfacially Controlled Synthesis of Hollow Mesoporous Silica Spheres with Radially Oriented Pore Structures. *Langmuir* **2010,** *26*, 12267-12272.

21. Chen, H.; Hu, T.; Zhang, X.; Huo, K.; Chu, P. K.; He, J., One-Step Synthesis of Monodisperse and Hierarchically Mesostructured Silica Particles with a Thin Shell. *Langmuir* **2010,** *26*, 13556-13563.

22. Yeh, Y.-Q.; Chen, B.-C.; Lin, H.-P.; Tang, C.-Y., Synthesis of Hollow Silica Spheres with Mesostructured Shell Using Cationic−Anionic-Neutral Block Copolymer Ternary Surfactants. *Langmuir* **2005,** *22*, 6-9.

23. Chen, X.; Berger, A.; Ge, M.; Hopfe, S.; Dai, N.; Gösele, U.; Schlecht, S.; Steinhart, M., Silica Nanotubes by Templated Thermolysis of Silicon Tetraacetate. *Chem. Mater.* **2011,** *23*, 3129-3131.

24. Wu, X.-J.; Jiang, Y.; Xu, D., A Unique Transformation Route for Synthesis of Rodlike Hollow Mesoporous Silica Particles. *J. Phys. Chem. C* **2011,** *115*, 11342-11347.

25. Wang, Y. W.; Liang, C. H.; Meng, G. W.; Peng, X. S.; Zhang, L. D., Synthesis and Photoluminescence Properties of Amorphous SiO_x Nanowires. *J. Mater. Chem.* **2002,** *12*, 651-653.

26. Zhu, Y. Q.; Hu, W. B.; Hsu, W. K.; Terrones, M.; Grobert, N.; Karali, T.; Terrones, H.; Hare, J. P.; Townsend, P. D.; Kroto, H. W.; Walton, D. R. M., A Simple Route to Silicon-Based Nanostructures. *Adv. Mater.* **1999,** *11*, 844-847.

27. Jiang, Z.; Xie, T.; Yuan, X. Y.; Geng, B. Y.; Wu, G. S.; Wang, G. Z.; Meng, G. W.; Zhang, L. D., Catalytic Synthesis and Photoluminescence of Silicon Oxide Nanowires and Nanotubes. *Appl. Phys. A* **2005,** *81*, 477-479.

28. Lee, K.-H.; Lofton, C.; Kim, K.; Seo, W.-S.; Lee, Y.; Lee, M.-H.; Sigmund, W., Photoluminescence from Amorphous Silica Nanowires Synthesized Using TiN/Ni/SiO_2/Si and TiN/Ni/Si Substrates. *Solid State Commun.* **2004,** *131*, 687-692.

29. Kim, J. H.; Yoon, C. S., Amorphous Silicon Dioxide Nanowire Array Synthesized *via* Carbonization of Polyimide Thin Film. *J. Phys. Chem. C* **2008,** *112*, 4463-4468.

30. Yu, D. P.; Hang, Q. L.; Ding, Y.; Zhang, H. Z.; Bai, Z. G.; Wang, J. J.; Zou, Y. H.; Qian, W.; Xiong, G. C.; Feng, S. Q., Amorphous Silica Nanowires: Intensive Blue Light Emitters. *Appl. Phys. Lett.* **1998,** *73*, 3076-3079.

31. Nagasawa, K.; Hama, Y., Photoluminescence from Defect Centers in High-Purity Silica Glasses Observed under 7.9-eV Excitation. *Phys. Rev. B* **1992,** *45*, 586-591.

32. Liao, L. S.; Bao, X. M.; Zheng, X. Q.; Li, N. S.; Min, N. B., Blue Luminescence from Si-Implanted SiO_2 Films Thermally Grown on Crystalline Silicon. *Appl. Phys. Lett.* **1996,** *68*, 850-852.

33. Itoh, C.; Suzuki, T.; Itoh, N., Luminescence and Defect Formation in Undensified and Densified Amorphous SiO_2. *Phys. Rev. B* **1990,** *41*, 3794-3799.

34. Byers, C. H.; Harris, M. T.; Williams, D. F., Controlled Microcrystalline Growth Studies by Dynamic Laser-Light-Scattering Methods. *Ind. Eng. Chem. Res.* **1987,** *26*, 1916-1923.

35. Kuijk, A.; van Blaaderen, A.; Imhof, A., Synthesis of Monodisperse, Rodlike Silica Colloids with Tunable Aspect Ratio.*J. Am. Chem. Soc.* **2011,** *133*, 2346-2349.

36. de Dood, M. J. A.; Kalkman, J.; Strohhöfer, C.; Michielsen, J.; van der Elsken, J., Hidden Transition in the "Unfreezable Water" Region of the PVP−Water System. *J. Phys. Chem. B* **2003,** *107*, 5906-5913.

37. Chen, S.-L.; Dong, P.; Yang, G.-H.; Yang, J.-J., Characteristic Aspects of Formation of New Particles during the Growth of Monosize Silica Seeds. *J.Colloid Interface Sci.* **1996,** *180*, 237-241.

38. Yang, H. G.; Zeng, H. C., Creation of Intestine-like Interior Space for Metal-Oxide Nanostructures with a Quasi-Reverse Emulsion. *Angew. Chem. Int. Ed* **2004,** *43*, 5206-5209.

39. Thimons, K. L.; Brazdil, L. C.; Harrison, D.; Fisch, M. R., Effects of Pentanol Isomers on the Growth of SDS Micelles in 0.5 M NaCl. *J. Phys. Chem. B* **1997,** *101*, 11087-11091.

40. Wang, L.; Tan, W., Multicolor FRET Silica Nanoparticles by Single Wavelength Excitation. *Nano Lett.***2006,** *6*, 84-88.

41. Rossi, L. M.; Shi, L.; Quina, F. H.; Rosenzweig, Z., Stöber Synthesis of Monodispersed Luminescent Silica Nanoparticles for Bioanalytical Assays. *Langmuir* **2005,** *21*, 4277-4280.

42. Nakamura, M.; Masayuki, S.; Ishimura, K., Synthesis, Characterization, and Biological Applications of Multifluorescent Silica Nanoparticles. *Anal. Chem* **2007,** *79*, 6507-6514.

43. Jain, P. K.; Huang, X.; El-Sayed, I. H.; El-Sayed, M. A., Review of Some Surface Plasmon Resonance-Enhanced Properties of Noble Metal Nanoparticles and Their Applications to Biosystems. *Plasmonics* **2007,** *2*, 107-118.

44. Xu, S.; Hartvickson, S.; Zhao, J. X., Engineering of SiO_2−Au−SiO_2 Sandwich Nanoaggregates Using a Building Block: Single, Double, and Triple Cores for Enhancement of Near Infrared Fluorescence. *Langmuir* **2008,** *24*, 7492-7499.

45. Warner, J. H.; Hoshino, A.; Yamamoto, K.; Tilley, R. D., Water-Soluble Photoluminescent Silicon Quantum Dots. *Angew. Chem. Int. Ed.* **2005,** *44*, 4550-4554.

46. Lim, S. F.; Riehn, R.; Tung, C.-k.; Ryu, W. S.; Zhuo, R.; Dalland, J.; Austin, R. H., Upconversion Nanophosphors for Bioimaing. *Nanotechnology* **2009,** *20*, 405701-405707.

47. Disney, M. D.; Zheng, J.; M., S. T.; Seeberger, P. H., Detection of Bacteria with Carbohydrate-Functionalized Fluorescent Polymers. *J. Am. Chem. Soc.* **2004,** *126*, 13343-13346.

48. Nagao, D.; Yokoyama, M.; Yamauchi, N.; Matsumoto, H.; Kobayashi, Y.; Konno, M., Synthesis of Highly Monodisperse Particles Composed of a Magnetic Core and Fluorescent Shell. *Langmuir* **2008,** , 9804-9808.

49. Zhang, J.; Lakowicz, J. R., Metal-Enhanced Fluorescence of an Organic Fluorophore Using Gold Particles. *Optics Express* **2007,** *15*, 2589-2606.

50. Aslan, K.; Wu, M.; Lakowicz, J. R.; Geddes, C. D., Fluorescent Core-Shell Ag@SiO_2 Nanocomposites for Metal-Enhanced Fluorescence and Single Nanoparticle Sensing Platforms. *J. Am. Chem. Soc*.**2007,** *129*, 1524-1525.

51. Yang, B.; Lu, N.; Qi, D.; Ma, R.; Wu, Q.; Hao, J.; Liu, X.; Mu, Y.; Reboud, V.; Kehagias, N.; Torres, C. M. S.; Boey, F. Y. C.; Chen, X.; Chi, L., Tuning the Intensity of Metal-Enhanced Fluorescence by Engineering Silver Nanoparticle Arrays. *Small* **2010,** *6*, 1038-1043.

52. Aslan, K.; Malyn, S. N.; Geddes, C. D., Angular-Dependent Metal-Enhanced Fluorescence from Silver Colloid-deposited Films: Opportunity for Angular-Ratiometric Surface Assays. *Analyst* **2007,** *132*, 1112-1121.

53. Aslan, K.; Lakowicz, J. R.; Szmacinski, H.; Geddes, C. D., Metal-Enhanced Fluorescence Solution-Based Sensing Platform. *J. Fluoresc.* **2004,** *14*, 677-679.

54. Yan, J.; Lu, Y.; WAng, P.; Ming, H., Integral Fluorescence Enhancement by Silver Nanoparticles Controlled *via* PMMA Matrix. *Opt. Commun.***2011,** *284*, 494-497.

55. Aslan, K.; Malyn, S. N.; Geddes, C. D., Metal-Enhanced Fluorescence from Gold Surface: Angular Dependent Emission. *J. Fluoresc.* **2007,** *17*, 7-13.

56. Zhang, Y.; Aslan, K.; Previte, M. J. R.; Geddes, C. D., Metal-Enhanced Fluorescence from Copper Substrates. *Appl. Phys. Chem. C* **2007,** *90*, 173116-173119.

57. Aslan, K.; Previte, M. J. R.; Zhang, Y.; Geddes, C. D., Metal-Enhanced Fluorescence from Nanoparticulate Zinc Films. *J. Phys. Chem. C* **2008,** *112*, 18368-18375.

58. Pribik, R.; Aslan, K.; Zhang, Y.; Geddes, C. D., Metal-Enhanced Fluorececne from Chromium Nanodeposits. *J. Phys. Chem. C* **2008,** *112*, 17969-17973.

59. Zhang, Y.; Padhyay, A.; Sevilleja, J. E.; Guerrant, R. L.; Geddes, C. D., Interactions of the Fluorophores with Iron Nanoparticles: Metal-Enhanced Fluorescene. *J. Phys. Chem. C* **2010,** *114*, 7575-7581.

60. Zhang, Y.; Geddes, C. D., Metal-Enhanced Fluorescence from Thermally Stable Rhodium Nanodeposits. *J. Mater. Chem.* **2010,** *20*, 8600-8606.

61. Hong, G.; Tabakman, S. M.; Welsher, K.; Wang, H.; Wang, X.; Dai, H., Metal-Enhanced Fluorescence of Carbon Nanotubes. *J. Am. Chem. Soc* **2010,** *132*, 15920-15923.

62. Zhang, Y.; Mandeng, L. N.; Bondre, N.; Dragan, A.; Geddes, C. D., Metal-Enhanced Fluorescence from Silver-SiO_2-Silver Nanoburger Structures. *Langmuir* **2010,** *26*, 12371-12376.

63. Zhang, Z.; Ni, W.; Kou, X.; Zhang, S.; Sun, Z.; Sun, L.-D.; Wang, J.; Yan, C., Incorporation of Gold Nanorods and Their Enhancement of Fluorescent in Mesostructured Silica Thin Films. *J. Phys. Chem. C* **2008,** *112*, 18895-18903.

64. Bardhan, R.; Grady, N. K.; Cole, J. R.; Joshi, A.; Halas, N. J., Fluorescence Enhancement by Au Nanostructures: Nanoshells and Nanorods. *ACS Nano* **2009,** *3*, 744-752.

65. Ray, K.; Badugu, R.; Lakowicz, J. R., Metal-Enhanced Fluorescence from CdTe Nanocrystals: A Single-Molecule Fluorescence Study. *J. Am. Chem. Soc* **2006,** *128*, 8998-8999.

66. Zhang, J.; Lakowicz, J. R., A Model for DNA Detection by Metal Enhanced Fluorescence from Immobilized Silver Nanoparticles on Solid Substrate. *J. Phys. Chem. B* **2006,** *110*, 2387-2392.

67. Aslan, K.; Wu, M.; Lakowicz, J.; Geddes, C., Metal Enhanced Fluorescence Solution-Based Sensing Platform 2: Fluorescent Core-Shell Ag@SiO_2 Nanoballs. *J. Fluoresc.* **2007,** *17*, 127-131.

68. Cheng, D.; Xu, Q., Separation Distance Dependent Fluorescence Enhancement of Fluorescenin Isothiocyanate by Silver Nanoparticles. *Chem. Commun.* **2007**, 248-250.

69. Jain, P. K.; Lee, K. S.; El-Sayed, I. H.; El-Sayed, M. A., Calculated Absorption and Scattering Properties of Gold Nanoparticles of Different Size, Shape, and Composition: Applications in Biological Imaging and Biomedicine. *J. Phys. Chem. B* **2006,** *110*, 7238-7248.

70. Jain, P. K.; Huang, W.; El-Sayed, M. A., On the Universal Scaling Behavior of the Distance Decay of Plasmon Coupling in Metal Nanoparticle Pairs: APlasmon Ruler Equation. *Nano Lett.* **2007,** *7*, 2080-2088.

71. Jain, P. K.; El-Sayed, M. A., Plasmon Coupling and Its Universal Size Scaling in Nanostrutures of Complex Geometry: Elongated Particle Pairs and Nanosphere Trimers. *J. Phys. Chem. C* **2008,** *112*, 4954-4960.

72. Jain, P. K.; El-Sayed, M. A., Universal Scaling of Plasmon Coupling in Metal Nanostructures: Extension from Particle Pairs to Nanoshells. *Nano Lett.* **2007,** *7*, 2854-2858.

73. Jain, P. K.; El-Sayed, M. A., Surface Plasmon Resonance Sensitivity of Metal Nanostructures: Physcal Basis and Universal Scaling in Metal Nanoshells. *J. Phys. Chem. C* **2007,** *111*, 17451-17454.

74. Huang, W.; Qian, W.; Jain, P. K.; El-Sayed, M. A., The Effect of Plasmon Field on the Coherent Lattice Phonon Oscillation in Electron-Beam Nanofabricated Gold Particle Pairs. *Nano Lett.* **2007,** *7*, 3227-3234.

75. Mahmoud, M. A.; El-Sayed, M. A., Reaction of Platinum Nanocatalyst with the Ferricyanide Reactant to Produce Prussian Blue Analogue Complexes. *J. Phys. Chem. C* **2007,** *111*, 17180-17183.

76. Leevy, W. M.; Gammon, S. T.; Jiang, H.; Johnson, J. R.; Maxwell, D. J.; Jackson, E. N.; marquez, M.; Piwnica-Worms, D.; Smith, B. D., Optical Imaging of Bacterial Infection in Living Mice Using A Fluorescent Near-Infrared Molecule Prone. *J. Am. Chem. Soc.* **2006,** *128*, 16476-16477.

77. Aslan, K.; Lakowicz, J. R.; Geddes, C. D., Rapid Deposition of Triangular Silver Nanoplates on Planar Surfaces: Application to Metal-Enhanced Fluorescence. *J. Phys. Chem. B* **2005,** *109*, 6247-6251.

78. Aslan, K.; Leonenko, Z.; Lakowicz, J. R.; Geddes, C. D., Fast and Slow Deposition of Silver Nanorods on Planar Surfaces: Application to Metal-Enhanced Fluorescence. *J. Phys. Chem. B* **2005,** *109*, 3157-3162.

79. Graf, C.; Vossen, D. L. J.; Imhof, A.; van Blaaderen, A., A General Method To Coat Colloidal Particles with Silica. *Langmuir* **2003,** *19*, 6693-6700.

80. Zhang, J.; Thurber, A.; Tenne, D. A.; Rasmussen, J. W.; Wingett, D.; Hanna, C.; Punnoose, A., Enhanced Dye Fluorescence in Novel Dye-ZnO Nanocomposites. *Adv.Funct.Mater.* **2010,** *20*, 4358-4363.

81. Malicka, J.; Gryczynski, I.; Kusba, J.; Lakowicz, J. R., Effects of Metallic Silver Island Films on Resonacne Energy Transfer Between N,N' -(dipropyl)-Tetramethyl-indocarbocyanine (Cy3)- and N,N'-(dipropyl)-Tetramethyl-indodicarbocyanine (Cy5)-Labeled DNA. *Biopolymers* **2003,** *70*, 595-603.

82. Torres-Chavolla, E.; Alocilja, E. C., Aptasensors for Detection of Microbial and Viral Pathogens. *Biosens. Bioelectron.* **2009,** *24*, 3175-3182.

83. Nam, J.-M.; Thaxton, C. S.; Mirkin, C. A., Nanoparticle-Based Bio-Bar Codes for the Ultrasensitive Detection of Proteins. *Science* **2003,** *301*, 1884-1886.

84. Wang, J.; Cao, Y.; Xu, Y.; Li, G., Colorimetric Multiplexed Immunoassay for Sequential Detection of Tumor Markers. *Biosens. Bioelectron.* **2009,** *25*, 532-536.

85. Zhou, W.-H.; Zhu, C.-L.; Lu, C.-H.; Guo, X.; Chen, F.; Yang, H.-H.; Wang, X., Amplified Detection of Protein Cancer Biomarkers Using DNAzyme Functionalized Nanoprobes. *Chem. Commun.* **2009,** *0*, 6845-6847.

86. Wang, H.; Wu, Z.; Tang, L.; Yu, R.; Jiang, J., Fluorescence Protection Assay: A Novel Homogeneous Assay Platform toward Development of Aptamer Sensors for Protein Detection. *Nucleic Acids Res.* **2011,** *39*, e122.

87. Akter, R.; Kyun Rhee, C.; Aminur Rahman, M., Sensitivity Enhancement of an Electrochemical Immunosensor through the Electrocatalysis of Magnetic Bead-Supported Non-Enzymatic Labels. *Biosens. Bioelectron.* **2014,** *54*, 351-357.

88. Du, S.; Guo, Z.; Chen, B.; Sha, Y.; Jiang, X.; Li, X.; Gan, N.; Wang, S., Electrochemiluminescence Immunosensor for Tumor Markers based on Biological Barcode Mode with Conductive Nanospheres. *Biosens. Bioelectron.* **2014,** *53*, 135-141.

89. Yu, Q.; Zhan, X.; Liu, K.; Lv, H.; Duan, Y., Plasma-Enhanced Antibody Immobilization for the Development of a Capillary-Based Carcinoembryonic Antigen Immunosensor Using Laser-Induced Fluorescence Spectroscopy. *Anal. Chem.* **2013,** *85*, 4578-4585.

90. Xia, H.; Mathew, B.; John, T.; Hegab, H.; Feng, J., Microfluidic Based Immunosensor for Detection and Purification of Carbonylated Proteins. *Biomed. Microdevices* **2013,** *15*, 519-530.

91. Armani, A. M.; Kulkarni, R. P.; Fraser, S. E.; Flagan, R. C.; Vahala, K. J., Label-Free Single-Molecule Detection with Optical Microcavities. *Science* **2007,** *317*, 783-787.

92. Nie, S.; Emory, S. R., Probing Single Molecules and Single Nanoparticles by Surface-Enhanced Raman Scattering. *Science* **1997,** *275*, 1102-1106.

93. Pang, Y.; Gordon, R., Optical Trapping of a Single Protein. *Nano Lett.* **2011,** *12*, 402-406.

94. Sorgenfrei, S.; Chiu, C.-y.; Gonzalez, R. L.; Yu, Y.-J.; Kim, P.; Nuckolls, C.; Shepard, K. L., Label-Free Single-Molecule Detection of DNA-Hybridization Kinetics with a Carbon Nanotube Field-Effect Transistor. *Nature Nanotechnol.* **2011,** *6*, 126-132.

95. Srinivas, R. L.; Chapin, S. C.; Doyle, P. S., Aptamer-Functionalized Microgel Particles for Protein Detection. *Anal. Chem.* **2011,** *83*, 9138-9145.

96. Akter, R.; Rahman, M. A.; Rhee, C. K., Amplified Electrochemical Detection of a Cancer Biomarker by Enhanced Precipitation Using Horseradish Peroxidase Attached on Carbon Nanotubes. *Anal. Chem.* **2012,** *84*, 6407-6415.

97. Lin, D.; Wu, J.; Ju, H.; Yan, F., Signal Amplification for Electrochemical Immunosensing by in situ Assembly of Host–Guest Linked Gold Nanorod Superstructure on Immunocomplex. *Biosens. Bioelectron.* **2013,** *45*, 195-200.

98. Shiddiky, M. J. A.; Kithva, P. H.; Rauf, S.; Trau, M., Femtomolar Detection of a Cancer Biomarker Protein in Serum with Ultralow Background Current by Anodic Stripping Voltammetry. *Chem. Commun.* **2012,** *48*, 6411-6413.

99. Wang, J.; Han, H.; Jiang, X.; Huang, L.; Chen, L.; Li, N., Quantum Dot-Based Near-Infrared Electrochemiluminescent Immunosensor with Gold Nanoparticle-Graphene Nanosheet Hybrids and Silica Nanospheres Double-Assisted Signal Amplification.*Anal. Chem.* **2012,** *84*, 4893-4899.

100.Zhang, J.; Yuan, Z.-F.; Wang, Y.; Chen, W.-H.; Luo, G.-F.; Cheng, S.-X.; Zhuo, R.-X.; Zhang, X.-Z., Multifunctional Envelope-Type Mesoporous Silica Nanoparticles for Tumor-Triggered Targeting Drug Delivery. *J. Am. Chem. Soc.* **2013,** *135*, 5068-5073.

101.Qiu, L.-P.; Wu, Z.-S.; Shen, G.-L.; Yu, R.-Q., Highly Sensitive and Selective Bifunctional Oligonucleotide Probe for Homogeneous Parallel Fluorescence Detection of Protein and Nucleotide Sequence. *Anal. Chem.* **2011,** *83*, 3050-3057.

102.Lu, L.; Liu, B.; Zhao, Z.; Ma, C.; Luo, P.; Liu, C.; Xie, G., Ultrasensitive Electrochemical Immunosensor for HE4 Based on Rolling Circle Amplification. *Biosens. Bioelectron.* **2012,** *33*, 216-221.

103.Zhang, Z.-z.; Zhang, C.-y., Highly Sensitive Detection of Protein with Aptamer-Based Target-Triggering Two-Stage Amplification. *Anal. Chem.* **2012,** *84*, 1623-1629.

104.Posthuma-Trumpie, G.; Korf, J.; Amerongen, A., Lateral Flow (Immuno)Assay: Its Strengths, Weaknesses, Opportunities and Threats. A Literature Survey. *Anal. Bioanal. Chem.***2009,** *393*, 569-582.

105.Wang, Y.-K.; Yan, Y.-X.; Ji, W.-H.; Wang, H.-a.; Li, S.-Q.; Zou, Q.; Sun, J.-H., Rapid Simultaneous Quantification of Zearalenone and Fumonisin B1 in Corn and Wheat by Lateral Flow Dual Immunoassay. *J. Agric. Food Chem.* **2013,** *61*, 5031-5036.

106.Parolo, C.; Medina-Sanchez, M.; de la Escosura-Muniz, A.; Merkoci, A., Simple Paper Architecture Modifications Lead to Enhanced Sensitivity in Nanoparticle based Lateral Flow Immunoassays. *Lab on a Chip* **2013,** *13*, 386-390.

107.Hou, S.-Y.; Hsiao, Y.-L.; Lin, M.-S.; Yen, C.-C.; Chang, C.-S., MicroRNA Detection using Lateral Flow Nucleic Acid Strips with Gold Nanoparticles. *Talanta* **2012,** *99*, 375-379.

108.Mao, X.; Ma, Y.; Zhang, A.; Zhang, L.; Zeng, L.; Liu, G., Disposable Nucleic Acid Biosensors Based on Gold Nanoparticle Probes and Lateral Flow Strip. *Anal. Chem.* **2009,** *81*, 1660-1668.

109.Shyu, R.-H.; Shyu, H.-F.; Liu, H.-W.; Tang, S.-S., Colloidal Gold-Based Immunochromatographic Assay for Detection of Ricin. *Toxicon* **2002,** *40*, 255-258.

110.López_Marzo, A. M.; Pons, J.; Blake, D. A.; Merkoçi, A., High Sensitive Gold-Nanoparticle based Lateral Flow Immunodevice for Cd^{2+}Detection in Drinking Waters. *Biosens. Bioelectron.* **2013,** *47*, 190-198.

111.Suárez-Pantaleón, C.; Wichers, J.; Abad-Somovilla, A.; van Amerongen, A.; Abad-Fuentes, A., Development of an Immunochromatographic Assay Based on Carbon Nanoparticles for the Determination of the Phytoregulator Forchlorfenuron. *Biosens. Bioelectron.* **2013,** *42*, 170-176.

112.Li, Z.; Wang, Y.; Wang, J.; Tang, Z.; Pounds, J. G.; Lin, Y., Rapid and Sensitive Detection of Protein Biomarker Using a Portable Fluorescence Biosensor Based on Quantum Dots and a Lateral Flow Test Strip. *Anal. Chem.* **2010,** *82*, 7008-7014.

113.Zou, Z.; Du, D.; Wang, J.; Smith, J. N.; Timchalk, C.; Li, Y.; Lin, Y., Quantum Dot-Based Immunochromatographic Fluorescent Biosensor for Biomonitoring Trichloropyridinol, a Biomarker of Exposure to Chlorpyrifos. *Anal. Chem.* **2010,** *82*, 5125-5133.

114.Li, X.; Lu, D.; Sheng, Z.; Chen, K.; Guo, X.; Jin, M.; Han, H., A Fast and Sensitive Immunoassay of Avian Influenza virus Based on Label-free Quantum Dot Probe and Lateral Flow Test Strip. *Talanta* **2012**, *100*, 1-6.

115.Liu, C.; Jia, Q.; Yang, C.; Qiao, R.; Jing, L.; Wang, L.; Xu, C.; Gao, M., Lateral Flow Immunochromatographic Assay for Sensitive Pesticide Detection by Using Fe_3O_4 Nanoparticle Aggregates as Color Reagents. *Anal. Chem.* **2011**, *83*, 6778-6784.

116.Fang, Z.; Ge, C.; Zhang, W.; Lie, P.; Zeng, L., A Lateral Flow Biosensor for Rapid Detection of DNA-Binding Protein c-jun. *Biosens. Bioelectron.* **2011**, *27*, 192-196.

117.Chao, C.-H.; Wu, C.-S.; Huang, C.-C.; Liang, J.-C.; Wang, H.-T.; Tang, P.-T.; Lin, L.-Y.; Ko, F.-H., A Rapid and Portable Sensor Based on Protein-Modified Gold Nanoparticle Probes and Lateral Flow Assay for Naked Eye Detection of Mercury Ion. *Microelectron. Eng.* **2012**, *97*, 294-296.

118. Anfossi, L.; Baggiani, C.; Giovannoli, C.; D'Arco, G.; Giraudi, G., Lateral-Flow Immunoassays for Mycotoxins and Phycotoxins: a Review. *Anal. Bioanal. Chem.***2013**, *405*, 467-480.

119. Choi, D. H.; Lee, S. K.; Oh, Y. K.; Bae, B. W.; Lee, S. D.; Kim, S.; Shin, Y.-B.; Kim, M.-G., A Dual Gold Nanoparticle Conjugate-based Lateral Flow Assay (LFA) Method for the Analysis of Troponin I. *Biosens. Bioelectron.* **2010**, *25*, 1999-2002.

120. Mei, Z.; Qu, W.; Deng, Y.; Chu, H.; Cao, J.; Xue, F.; Zheng, L.; El-Nezamic, H. S.; Wu, Y.; Chen, W., One-Step Signal Amplified Lateral Flow Strip Biosensor for Ultrasensitive and on-site Detection of Bisphenol A (BPA) in Aqueous Samples. *Biosens. Bioelectron.* **2013**, *49*, 457-461.

121. He, Y.; Zhang, S.; Zhang, X.; Baloda, M.; Gurung, A. S.; Xu, H.; Zhang, X.; Liu, G., Ultrasensitive Nucleic Acid Biosensor based on Enzyme–Gold Nanoparticle Dual Label and Lateral Flow Strip Biosensor. *Biosens. Bioelectron.* **2011**, *26*, 2018-2024.

122. Tang, D.; Sauceda, J. C.; Lin, Z.; Ott, S.; Basova, E.; Goryacheva, I.; Biselli, S.; Lin, J.; Niessner, R.; Knopp, D., Magnetic Nanogold Microspheres-Based Lateral-Flow Immunodipstick for Rapid Detection of Aflatoxin B2 in Food. *Biosens. Bioelectron.* **2009**, *25*, 514-518.

123. Vallet-Regi, M.; Balas, F.; Arcos, D., Mesoporous Materials for Drug Delivery. *Angew. Chem. Int. Ed.* **2007**, *46*, 7548-7558.

124. Bae, S. W.; Tan, W.; Hong, J.-I., Fluorescent Dye-Doped Silica Nanoparticles: New Tools for Bioapplications. *Chem. Commun.* **2012**, *48*, 2270-2282.

125. Fan, H.; Jiao, F.; Chen, H.; Zhang, F.; Wang, Q.; He, P.; Fang, Y., Qualitative and Quantitative Detection of DNA Amplified with HRP-Modified SiO_2Nanoparticles using Scanning Electrochemical Microscopy. *Biosens. Bioelectron.* **2013**, *47*, 373-378.

126. Qi, W.; Wu, D.; Zhao, J.; Liu, Z.; Zhang, W.; Zhang, L.; Xu, G., Electrochemiluminescence Resonance Energy Transfer Based on $Ru(phen)_3^{2+}$-Doped Silica Nanoparticles and Its Application in "Turn-on" Detection of Ozone. *Anal. Chem.* **2013**, *85*, 3207-3212.

127. Zhang, Y.; Yuan, Q.; Chen, T.; Zhang, X.; Chen, Y.; Tan, W., DNA-Capped Mesoporous Silica Nanoparticles as an Ion-Responsive Release System to Determine the Presence of Mercury in Aqueous Solutions. *Anal. Chem.* **2012**, *84*, 1956-1962.

128.Kawde, A.; Mao, X.; Xu, H.; Zeng, Q.; He, Y.; Liu, G., Moving Enzyme-Linked Immunosorbent Assay to the Point-of-Care Dry-Reagent Strip Biosensor. *Am. J. Biomed. Sci.* **2010**, *2*, 23-32.

129.Xu, H.; Mao, X.; Zeng, Q.; Wang, S.; Kawde, A.-N.; Liu, G., Aptamer-Functionalized Gold Nanoparticles as Probes in a Dry-Reagent Strip Biosensor for Protein Analysis. *Anal. Chem.* **2008**, *81*, 669-675.

130.Tanaka, H.; Mitsuishi, M.; Miyashita, T., Tailored-Control of Gold Nanoparticle Adsorption onto Polymer Nanosheets. *Langmuir* **2003**, *19*, 3103-3105.

131.Tseng, R. J.; Huang, J.; Ouyang, J.; Kaner, R. B.; Yang, Polyaniline Nanofiber/Gold Nanoparticle Nonvolatile Memory. *Nano Lett.* **2005**, *5*, 1077-1080.

132.Chu, H.; Wang, J.; Ding, L.; Yuan, D.; Zhang, Y.; Liu, J.; Li, Y., Decoration of Gold Nanoparticles on Surface-Grown Single-Walled Carbon Nanotubes for Detection of Every Nanotube by Surface-Enhanced Raman Spectroscopy. *J. Am. Chem. Soc.* **2009**, *131*, 14310-14316.

133.Minati, L.; Antonini, V.; Dalla Serra, M.; Speranza, G., Multifunctional Branched Gold–Carbon Nanotube Hybrid for Cell Imaging and Drug Delivery. *Langmuir* **2012**, *28*, 15900-15906.

134.Lin, W.; Huang, Y.-w.; Zhou, X.-D.; Ma, Y., *In vitro*Toxicity of Silica Nanoparticles in Human Lung Cancer Cells. *Toxicol. Appl. Pharmacol.* **2006**, *217*, 252-259.

135.Jin, Y.; Kannan, S.; Wu, M.; Zhao, J. X., Toxicity of Luminescent Silica Nanoparticles to Living Cells. *Chem. Res. Toxicol.* **2007**, *20*, 1126-1133.

136.Kim, J.-H.; Bryan, W. W.; Randall Lee, T., Preparation, Characterization, and Optical Properties of Gold, Silver, and Gold−Silver Alloy Nanoshells Having Silica Cores. *Langmuir* **2008**, *24*, 11147-11152.

137.Graf, C.; van Blaaderen, A., Metallodielectric Colloidal Core−Shell Particles for Photonic Applications. *Langmuir* **2002**, *18*, 524-534.

138.Wang, H.; Tam, F.; Grady, N. K.; Halas, N. J., Cu Nanoshells: Effects of Interband Transitions on the Nanoparticle Plasmon Resonance. *J. Phys. Chem. B* **2005**, *109*, 18218-18222.

139.Loo, C.; Lowery, A.; Halas, N.; West, J.; Drezek, R., Immunotargeted Nanoshells for Integrated Cancer Imaging and Therapy. *Nano Lett.* **2005**, *5*, 709-711.

140.Oldenburg, S. J.; Jackson, J. B.; Westcott, S. L.; Halas, N. J., Infrared Extinction Properties of Gold Nanoshells. *Appl.Phys. Lett.***1999**, *75*, 2897-2899.

141.Chen, W. R.; Adams, R. L.; Carubelli, R.; Nordquist, R. E., Laser-Photosensitizer Assisted Immunotherapy: a Novel Modality for Cancer Treatment. *Cancer Lett.* **1997**, *115*, 25-30.

142.Kam, N. W. S.; O'Connell, M.; Wisdom, J. A.; Dai, H., Carbon Nanotubes as Multifunctional Biological Transporters and Near-Infrared Agents for Selective Cancer Cell Destruction. *Proc. Natl. Acad. Sci. U.S.A.* **2005**, *102*, 11600-11605.

143.Huang, X.; El-Sayed, I. H.; Qian, W.; El-Sayed, M. A., Cancer Cell Imaging and Photothermal Therapy in the Near-Infrared Region by Using Gold Nanorods. *J. Am. Chem. Soc.* **2006**, *128*, 2115-2120.

144.Tang, L.; Liu, L. J.; Elwing, H., Complement Activation and Inflammation Triggered by Model Biomaterial Surfaces. *J. Colloid Interface Sci.* **1998**, *41*, 333-340.

145.Hu, M.; Chen, J.; Li, Z.-Y.; Au, L.; Hartland, G. V.; Li, X.; Marquez, M.; Xia, Y., Gold Nanostructures: Engineering Their Plasmonic Properties for Biomedical Applications. *Chem. Soc. Rev.* **2006**, *35*, 1084-1094.

146.Shukla, R.; Bansal, V.; Chaudhary, M.; Basu, A.; Bhonde, R. R.; Sastry, M., Biocompatibility of Gold Nanoparticles and Their Endocytotic Fate Inside the Cellular Compartment: A Microscopic Overview. *Langmuir* **2005**, *21*, 10644-10654.

147.Skrabalak, S. E.; Chen, J.; Au, L.; Lu, X.; Li, X.; Xia, Y., Gold Nanocages for Biomedical Applications. *Adv. Mater.* **2007**, *19*, 3177-3184.

148.Kim, J.; Park, S.; Lee, J. E.; Jin, S. M.; Lee, J. H.; Lee, I. S.; Yang, I.; Kim, J.-S.; Kim, S. K.; Cho, M.-H.; Hyeon, T., Designed Fabrication of Multifunctional Magnetic Gold Nanoshells and Their Application to Magnetic Resonance Imaging and Photothermal Therapy. *Angew. Chem. Int. Ed.* **2006**, *45*, 7754-7758.

149.Bartczak, D.; Muskens, O. L.; Nitti, S.; Sanchez-Elsner, T.; Millar, T. M.; Kanaras, A. G., Interactions of Human Endothelial Cells with Gold Nanoparticles of Different Morphologies. *Small* **2012**, *8*, 122-130.

150.Wang, S. M.; Xiao, J. J.; Yu, K. W., Tunable Coupled Plasmon Modes *via*Nanoshell Particle Chains. *Opt. Commun.* **2007**, *279*, 384-389.

151.Gobin, A. M.; O'Neal, D. P.; Watkins, D. M.; Halas, N. J.; Drezek, R. A.; West, J. L., Near Infrared Laser-Tissue Welding Using Nanoshells as an Exogenous Absorber. *Las. Surg. Med.* **2005**, *37*, 123-129.

152.Gobin, A. M.; Lee, M. H.; Halas, N. J.; James, W. D.; Drezek, R. A.; West, J. L.,Near-Infrared Resonant Nanoshells for Combined Optical Imaging and Photothermal Cancer Therapy. *Nano Lett.* **2007**, *7*, 1929-1934.

153.Wu, C.; Liang, X.; Jiang, H., Metal Nanoshells as a Contrast Agent in Near-Infrared Diffuse Optical Tomography. *Opt. Commun.* **2005**, *253*, 214-221.

154.Gelbrich, T.; Feyen, M.; Schmidt, A. M., Magnetic Thermoresponsive Core−Shell Nanoparticles. *Macromolecules* **2006**, *39*, 3469-3472.

155.Levin, C. S.; Hofmann, C.; Ali, T. A.; Kelly, A. T.; Morosan, E.; Nordlander, P.; Whitmire, K. H.; Halas, N. J., Magnetic−Plasmonic Core−Shell Nanoparticles. *ACS Nano* **2009**, *3*, 1379-1388.

156.Yang, Y.; Liu, J.; Li, X.; Liu, X.; Yang, Q., Organosilane-Assisted Transformation from Core–Shell to Yolk–Shell Nanocomposites. *Chem.Mater.* **2011**, *23*, 3676-3684.

157.Zeng, H.; Li, J.; Wang, Z. L.; Liu, J. P.; Sun, S., Bimagnetic Core/Shell FePt/Fe_3O_4 Nanoparticles. *Nano Lett.* **2003**, *4*, 187-190.

158.Schmit, V. L.; Martoglio, R.; Scott, B.; Strickland, A. D.; Carron, K. T., Lab-on-a-Bubble: Synthesis, Characterization, and Evaluation of Buoyant Gold Nanoparticle-Coated Silica Spheres. *J. Am. Chem. Soc.* **2011**, *134*, 59-62.

159.Jackson, J. B.; Halas, N. J., Silver Nanoshells: Variations in Morphologies and Optical Properties. *J. Phys. Chem. B* **2001**, *105*, 2743-2746.

160.Goude, Z. E.; Leung, P. T., Surface Enhanced Raman Scattering from Metallic Nanoshells with Nonlocal Dielectric Response. *Solid State Commun.* **2007**, *143*, 416-420.

161.Hale, G. D.; Jackson, J. B.; Shmakova, O. E.; Lee, T. R.; Halas, N. J., Enhancing the Active Lifetime of Luminescent Semiconducting Polymers *via* Doping with Metal Nanoshells. *Appl.Phys. Lett* **2001**, *78*, 1502-1504.

162.Peters, R.; Kramer, E.; Oomen, A. G.; Herrera Rivera, Z. E.; Oegema, G.; Tromp, P. C.; Fokkink, R.; Rietveld, A.; Marvin, H. J. P.; Weigel, S.; Peijnenburg, A. A. C. M.; Bouwmeester, H., Presence of Nano-Sized Silica during i*n vitro* Digestion of Foods Containing Silica as a Food Additive. *ACS Nano* **2012**, *6*, 2441-2451.

163.Farre, C.; Lansalot, M.; Bazzi, R.; Roux, S.; Marquette, C. A.; Catanante, G.; Blum, L.J.; Charvet, N.; Louis, C.; Chaix, C., Automated Oligonucleotide Solid-Phase Synthesis on Nanosized Silica Particles Using Nano-on-Micro Assembled Particle Supports. *Langmuir* **2009**, *26*, 4941-4950.

164.Fujiwara, M.; Shiokawa, K.; Sakakura, I.; Nakahara, Y., Silica Hollow Spheres with Nano-Macroholes Like Diatomaceous Earth. *Nano Lett.* **2006**, *6*, 2925-2928.

165.Zhang, Y.; Li, G.; Wu, Y.; Luo, Y.; Zhang, L., The Formation of Mesoporous TiO_2 Spheres *via* a Facile Chemical Process. *J. Phys. Chem. B***2005**, *109*, 5478-5481.

166.Hahn, M.; Singh, A.; Sharma, P.; Brown, S.; Moudgil, B., Nanoparticles as Contrast Agents for *invivo*Bioimaging: Current Status and Future Perspectives. *Anal. Bioanal. Chem.* **2011**, *399*, 3-27.

167.Kennedy, L. C.; Bickford, L. R.; Lewinski, N. A.; Coughlin, A. J.; Hu, Y.; Day, E. S.; West, J. L.; Drezek, R. A., A New Era for Cancer Treatment: Gold-Nanoparticle-Mediated Thermal Therapies. *Small* **2011**, *7*, 169-183.

168.Tong, L.; Wei, Q.; Wei, A.; Cheng, J.-X., Gold Nanorods as Contrast Agents for Biological Imaging: Optical Properties, Surface Conjugation and Photothermal Effects. *Photochem. Photobiol.* **2009**, *85*, 21-32.

169.Au, L.; Zheng, D.; Zhou, F.; Li, Z.-Y.; Li, X.; Xia, Y., A Quantitative Study on the Photothermal Effect of Immuno Gold Nanocages Targeted to Breast Cancer Cells. *ACS Nano* **2008**, *2*, 1645-1652.

170.ANSI, American National Standard for Safe Use of Lasers. *Laser Institute of America: Orlando, FL* **2000**.

171.Park, S.; Heo, J.; Kim, H. J., A Novel Route to the Synthesis of Silica Nanowires without a Metal Catalyst at Room Temperature by Chemical Vapor Deposition. *Nano Lett.* **2011**, *11*, 740-745.

172.Yang, Z.; Zhang, Y.; Liu, D.; Nie, E.; Jiao, Z.; Jin, Y.; He, Y.; Gong, M.; Sun, X., Selective Synthesis of SiO_2 NWs on Si Substrate and Their Adjustable Photoluminescence. *J. Non-Cryst. Solids* **2010**, *356*, 2207-2210.

173.Ramgir, N. S.; Sekhar, P. K.; Zajac, A.; Lee, L.; Zhukov, T.; Bhansali, S., Ultrasensitive Voltammetric Detection of IL-10, a Lung Cancer Biomarker, in Serum Using SiO_2 Nanowires Template. *Sens. Lett.* **2007**, *5*, 608-611.

174.Elliman, R. G.; Wilkinson, A. R.; Kim, T. H.; Sekhar, P. K.; Bhansali, S., Optical Emission from Erbium-Doped Silica Nanowires. *J. Appl. Phys.* **2008**, *103*, 104304-104304-5.

175.Ramgir, N. S.; Zajac, A.; Sekhar, P. K.; Lee, L.; Zhukov, T. A.; Bhansali, S., Voltammetric Detection of Cancer Biomarkers Exemplified by Interleukin-10 and Osteopontin with Silica Nanowires. *J. Phys. Chem. C* **2007**, *111*, 13981-13987.

176.Hermanson, G. T.; Ed., *In Bioconjugate Techniques; Academic Press: San Diego* **1996**, 597.

177.Wu, M.; Pasula, R.; Smith, P. A.; Martin II, W. J., Mapping Alveolar Epithelial Binding Sites in vivo Using Phase Peptide Libraries. *Gene Ther.* **2003**, *10*, 1429-1436.

178.Kannan, S.; Pang, H.; Foster, D.; Rao, Z.; Wu, M., Human 8-oxoguanine DNA Glycosylase Links MAPK Activation to Resistance to Hyperoxia in Lung Epithelial Cells. *Cell Death Differ.* **2006**, *13*, 311-323.

179.Pattanaik, M.; Bhaumik, S. K., Adsorption Behaviour of Polyvinyl Pyrrolidone on Oxide Surfaces. *Mater. Lett.* **2000**, *44*, 352-360.

180.Zhang, M.; Fang, K.; Lin, M.; Hou, B.; Zhong, L.; Zhu, Y.; Wei, W.; Sun, Y., Controlled Fabrication of Iron Oxide/Mesoporous Silica Core–Shell Nanostructures. *J. Phys. Chem. C* **2013**, *117*, 21529-21538.

181.Ab Kadir, R.; Li, Z.; Sadek, A. Z.; Abdul Rani, R.; Zoolfakar, A. S.; Field, M. R.; Ou, J. Z.; Chrimes, A. F.; Kalantar-zadeh, K., Electrospun Granular Hollow SnO_2 Nanofibers Hydrogen Gas Sensors Operating at Low Temperatures. *J. Phys. Chem. C* **2014**, *118*, 3129-3139.

182.Li, J.; Wang, J.; Liang, X.; Zhang, Z.; Liu, H.; Qian, Y.; Xiong, S., Hollow $MnCo_2O_4$ Submicrospheres with Multilevel Interiors: From Mesoporous Spheres to Yolk-in-Double-Shell Structures. *ACS Appl. Mater. Interfaces* **2013**, *6*, 24-30.

183.Duff, D. G.; Baiker, A.; Edwards, P. P., A New Hydrosol of Gold Clusters. 1. Formation and Particle Size Variation. *Langmuir* **1993**, *9*, 2301-2309.

184.Oh, W.-K.; Kim, S.; Choi, M.; Kim, C.; Jeong, Y. S.; Cho, B.-R.; Hahn, J.-S.; Jang, J., Cellular Uptake, Cytotoxicity, and Innate Immune Response of Silica−Titania Hollow Nanoparticles Based on Size and Surface Functionality. *ACS Nano* **2010**,*4*, 5301-5313.